Reduction of the Onset of Nucleate Boiling Superheat of Electrical Insulating Fluid by the Honeycomb Porous Plate and Heated Film

呉, 菲菲

九州大学
KYUSHU UNIVERSITY

Reduction of the Onset of Nucleate Boiling Superheat of Electrical Insulating Fluid by the Honeycomb Porous Plate and Heated Film

By

Feifei, Wu

Thesis submitted to Kyushu University for the degree of Doctor of Philosophy

Examiner: Prof. Shoji Mori

Co-examiner: Prof. Yasuyuki Takata

Prof. Wei Liu

Graduate School of Engineering

Kyushu University

Fukuoka, JAPAN

August 2023

Abstract

The explosive growth and miniaturization of electronic devices demands advanced cooling techniques, such as immersion cooling via boiling of dielectric liquids. Due to the high wettability, dielectric liquids tend to fill surface cavities, which trap gas and act as nucleation sites for boiling. As a result, excessive superheat exhibited at the onset of nucleate boiling (ONB) of dielectric liquids and temperature overshoots occurred. In this study, a honeycomb porous plate (HPP) was utilized to improve the performance of saturated pool boiling of dielectric liquids. As the working fluid, a fluorinated dielectric of AE-3000 has been selected. Three kinds of HPPs were manufactured with different cavity ranges. The cavities are designed in a pore size distribution (PSD) with peak pore diameters of 0.2 μm (0.004~0.9 μm), 0.9 μm (0.004~4.8 μm) and 0.6 μm (0.004~20.8 μm), respectively. Particularly, re-entrant cavities were observed in the HPP with the peak pore diameter 0.6 μm. HPPs were attached to an indium–tin oxide (ITO) heater and then tested in a boiling experiment immediately after the degassing procedure. Infrared cameras and high-speed videos were simultaneously measured the top surface temperature and bubble generation. As a result, reducing ΔT_{ONB} was found with the increasing range of cavities.

After immersing the HPPs into AE-3000 for 48 hours, boiling experiments were restarted to examine the stability of the ΔT_{ONB}. Increasing ΔT_{ONB} was observed on the HPP with peak pore diameters of 0.2 μm (0.004~0.9 μm) and reliable ΔT_{ONB} was still achieved on the other HPPs. This finding indicated that large amounts of cavities on the HPP (peak pore diameters of 0.2 μm) were flooded by the highly wetting liquid during the immersion period. Therefore, a coupled section combining the HPP and a metal fine heated film with a continuous small input power was developed to reactivate nucleate cavities. Bubbles generating from the heated film was considered to displace the liquid trapped within the flooded cavities and be trapped into the cavities for the nucleation promotion. Finally, this section successfully maintained the ΔT_{ONB} at a desirable value after immersion. Later, exploration about how to minimize energy consumption of the heated film while still ensuring low ΔT_{ONB} was conducted. HPP couple with an intermittent heated film was tested in boiling experiments. Suggestions for balancing performance (low ΔT_{ONB}) with energy efficiency was provided for the coupled section use in thermal management of high-power density electronics.

Contents

List of figures

List of tables

Nomenclature

A	Area of the heating surface (m^2)
$d_{avg.}$	Average pore diameter (μm)
d_c	Cavity diameter in Hsu's model (μm)
d_{max}	Maximum pore diameter (μm)
d_{min}	Minimum pore diameter (μm)
D_{HPP}	Diameter of the honeycomb porous plate (mm)
h	Cavity depth (μm)
h_{fg}	Latent heat of vaporization (J/kg)
h_{nc}	Natural convection heat transfer coefficient (W/(m^2 K))
i	Uncertainty parameters index
I	Current (A)
ΔI	Current uncertainty (A)
k_l	Liquid thermal conductivity (W/[m K])
k_s	Sapphire thermal conductivity (W/[m K])
m_i	Uncertainty parameters [-]
Δm_i	Individual standard uncertainty [-]
p_l	Liquid pressure (Pa)
p_v	Vapor pressure (Pa)
q	Heat flux (W/m^2)
q_w	Heat flux for boiling (W/m^2)
Δq	Heat flux uncertainty (W/m^2)
V	Voltage (V)
V_{pore}	Volume of pore (percentage of total or volume per unit mass) (m^3/kg)
ΔV	Voltage uncertainty (V)
v_{fg}	Liquid to vapour specific volume change (m^3/kg)
R_a	Arithmetic mean roughness height of the sapphire substrate (nm)
R_q	Root mean square roughness height of the sapphire substrate (nm)
r_b	Bubble radius (m)
t	Time (s)
T	Temperature (K)
T_l	Liquid temperature (K)
$T_{ITO\text{-}cal}$	Calibrated temperature (K)
T_{sat}	Saturation temperature (K)
T_w	Wall temperature (K)
ΔT_{ONB}	Surface superheat at bubble inception (K)
ΔT_w	Wall superheat (K)
Δu	Overall uncertainty
z	Spatial z coordinate (m)
z_c	Mesh size in z-direction (μm)
z_{bottom}	Bottom surface position (m)
z_{top}	Top surface position (m)

Greek

β	Cavity cone half-angle (°)
δ_T	Thermal boundary layer thickness (m)
θ	Contact angle (°)
μ_l	Liquid dynamic viscosity (Pa s)
ρ_v	Vapor density (kg/m^3)
σ	Surface tension (N/m)

Abbreviations

CHF	Critical heat flux
HF	Heated film
HPP	Honeycomb porous plate
HSV	High-speed video
HTC	Heat transfer coefficient
IR	Infrared
ITO	Indium–tin oxide
ONB	Onset of the nucleate boiling
PS	Plain surface
PSD	Pore size distribution
SEM	Scanning electron microscopy
TTL	Transistor–transistor logic

Subscripts

l	Liquid
v	Vapor
w	Heat transfer surface

CHAPTER 1

Introduction

1.1 Motivation

With the exponential growth in digital infrastructure driven by artificial intelligence, quantum computing, and high-performance computing advancements, data centers are experiencing unprecedented heat generation [1,2]. Electricity consumption by data centers in Japan is expected to rise as high as 105 terawatt-hours by 2040, up roughly fivefold from 20 terawatt-hours in 2021, and to 211 terawatt-hours in 2050, according to the Central Research Institute of Electric Power Industry. Therefore, adjustments to the cooling system are needed to improve the efficiency of electrical energy consumed, this will also reduce maintenance costs and electricity usage [3]. Immersion cooling, as shown in Fig 1.1, where electronic components are submerged directly in dielectric fluids, emerges as a promising technique to mitigate these thermal issues [4-10]. This technique is capable of dissipating high heat fluxes while maintaining relatively small temperature differences between the heated surface and the coolant liquid [11-15].

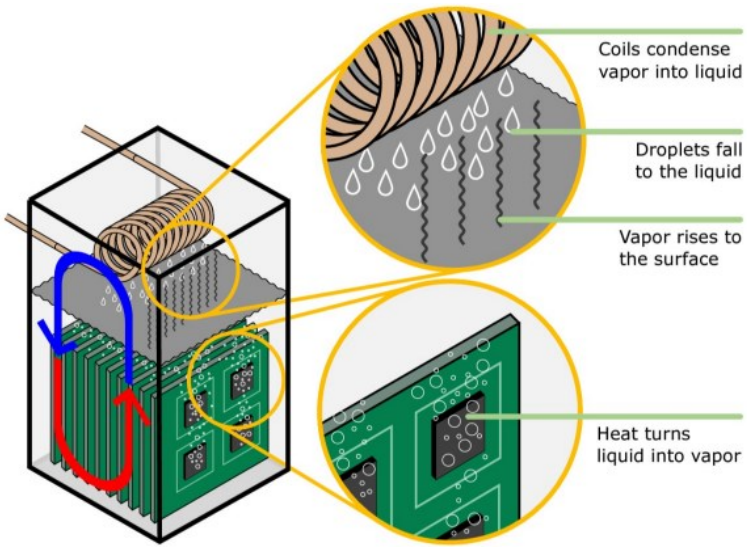

Fig. 1.1 Two-phase immersion cooling [10].

Essential criteria for the boiling liquid include dielectric properties, environmental friendliness, and a proper boiling temperature within the desired temperature range of these components [16]. These criteria are reasonably met by Fluorinert™ electronic liquids and Novec engineered fluids [17].

According to the previous research about the wettability influence on the onset of nucleate boiling (ONB), nucleation cavity immersed in highly wetting liquid could be easily flooded then prevent vapor entrapment for the generation of bubble nuclei [18-20]. As a result, higher excessive superheats are required for boiling incipience. The superheat for boiling incipience is defined as the ΔT_{ONB}. Boiling occurs if surface superheat exceeds a threshold value, called the *Onset of Nucleate Boiling* (ONB).

In this thesis, we investigate the superheat reduction of the surface superheat for the ONB (ΔT_{ONB}) in the immersion boiling of dielectric liquid. One major challenge of the immersion cooling in electronic devices is the difficulty in initiating boiling due to the high wettability of dielectric liquid coolants. As shown in Fig. 1.2, when the heat load on electronic devices increases over time, cooling system tend to experience a delay in initiating boiling. Research [20] on dielectric liquid boiling have confirmed that the temperature at which boiling occurs (ΔT_{ONB}) usually exceeds safe operating range for devices. Before entering the efficient heat transfer regime of boiling, the device surfaces may have already suffered damage due to the overshoot. Additionally, this high ΔT_{ONB} causes an abrupt surface temperature to decrease later due to the sudden release of stored sensible heat through boiling, leading to thermal shock in electronic components and impairing cooling process effectiveness.

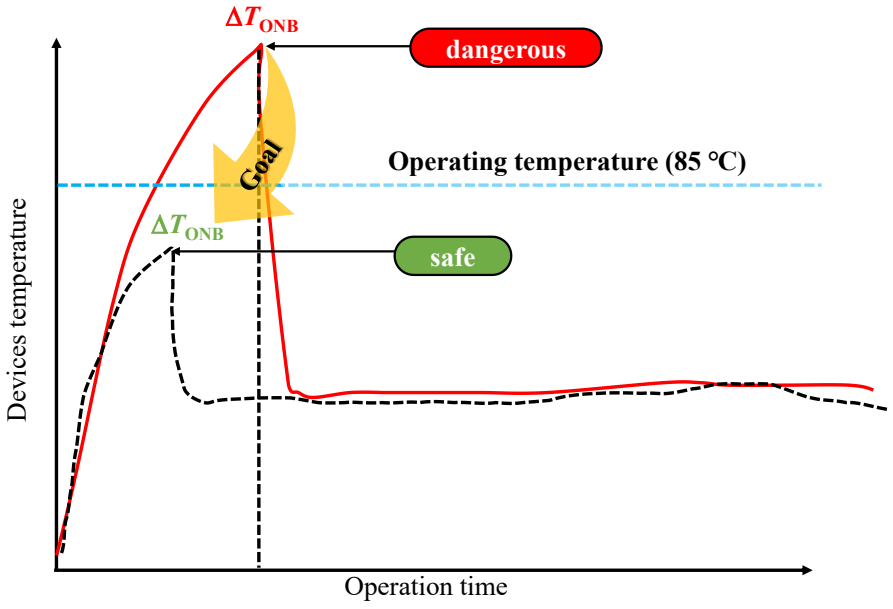

Fig. 1.2 Devices temperature for immersion cooling with dielectric liquid.

Thus, a honeycomb porous plate (HPP) was utilized to promote the ΔT_{ONB} of saturated pool boiling of dielectric liquids. Detailed investigation was performed, i.e., temperature distribution of

the heated surface, bubble formation pattern and durability of the HPP. Furthermore, a hybrid enhancement technique is proposed, combining the HPP with a fine heated film, aiming to sustain a stable reduction in the superheat for the ONB while considering durability aspects. Motivation for this research stems from an urgent need to overcome limitations presented by high ΔT_{ONB} in immersion boiling cooling techniques and ensure efficient heat transfer while keeping device temperatures within safe operating ranges and minimizing thermal shock risk to reduce mechanical failure and ensure reliable cooling of electronic components.

1.2 Background and Previous Research

1.2.1 Description of boiling phenomenon

Generally, boiling curves were used as a practical way to investigate the overall boiling performance, i.e., superheat for the onset of nucleate boiling (ΔT_{ONB}), heat transfer coefficient and the critical heat flux (CHF). A brief introduction was made about boiling curves. A boiling curve shows the relationship between heat flux (q) and wall superheat (ΔT_w) during boiling, which was first experimentally identified by Nukiyama [21]. Nukiyama's studies were validated by Drew and Mueller (1937) with experiments performed on an organic liquid [22]. Wall superheat is the temperature difference between the heated surface and liquid saturation temperature. Figure 1.3 (a) schematically depicts the boiling curve of water, where Fujii and Imura's correlation was used to predict the natural convection regime, as marked with blue line. Besides, the Rohsenow's correlation (red curve) was used for nucleate boiling regime. And the CHF value was predicted by the Zuber's correlation [22]. It can be seen the boiling curve typically include:

Natural convection regime. Natural convection is the low heat flux region of the boiling curve, where fluid flow is driven by buoyancy caused by temperature differences within the fluid. This regime lacks bubble formation as the surface temperature does not go beyond the nucleation temperature. Heat transfer mainly occurs through conduction and convection, without substantial boiling activity.

Nucleate boiling regime. As wall superheat increases, bubbles begin to form on the heater surface, known as the onset of nucleate boiling (ONB). These bubbles rise to the liquid's free surface due to buoyancy forces. The steep slope between the ONB and the CHF point on the boiling curve reflects a high heat transfer coefficient, which increases with surface temperature. This increase in heat transfer coefficient is primarily attributed to the activation of more nucleation sites as heat flux rises

[23]. Besides, CHF represents a maximum heat flux in boiling regime, where a boiling crisis occurs when the heat flux surpasses this limit and cannot be sustained [24-27].

Transition boiling regime. The transition boiling regime is an unstable and relatively short-lived regime that occurs between the nucleate boiling regime and the film boiling regime during the boiling process. It is characterized by the intermittent formation and collapse of the vapor film on the heated surface [28-31].

Film boiling regime. The film boiling regime occurs at heat fluxes higher than the CHF, which is the maximum heat flux that can be sustained during the nucleate boiling regime. A continuous vapor film or layer forms on the heated surface, which acts as an insulating barrier and significantly reduces the heat transfer rate [32-35].

Compared with boiling curves of water, a higher superheat at the ONB in boiling curves of dielectric liquid is observed [36-38], as shown in Fig. 1.3 (b). Corty and Foust observed the higher excessive surface temperature on initial boiling nucleation of dielectric liquids (ether, pentane and Freon-113) [39]. For the dielectric liquids with highly wetting ability, even the microcavities on a surface could be easily flooded then prevent vapor entrapment for the generation of bubble nuclei. As a result, higher excessive superheats of boiling incipience are required for dielectric liquid than for partially wetting liquids (water). This higher excessive ΔT_{ONB} occurs during the transition from natural convection heat transfer to nucleate boiling heat transfer. During the nucleate boiling regime, dielectric liquids can achieve high dissipated heat fluxes at small temperature differences, similar to water.

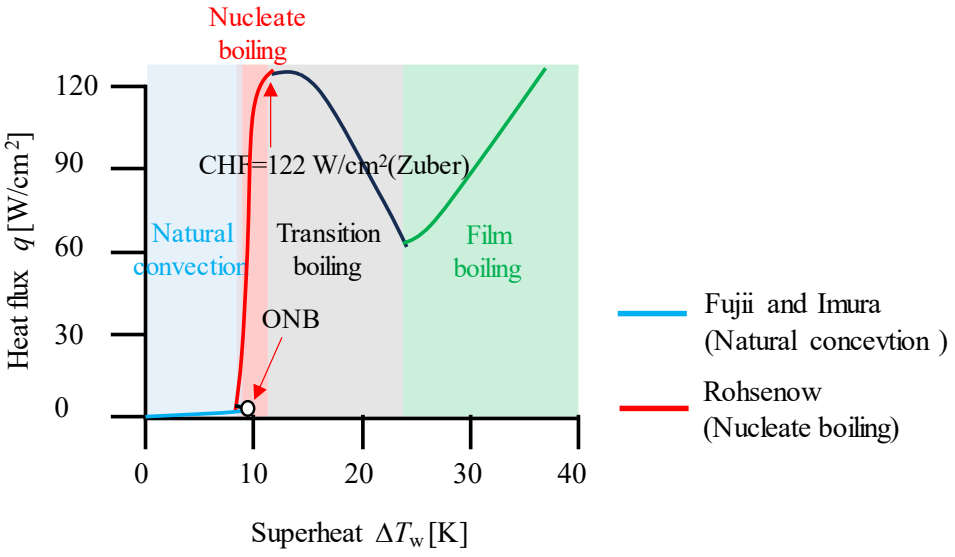

(a)

Fig. 1.3 Boiling curves of (a) water (b) dielectric liquids.

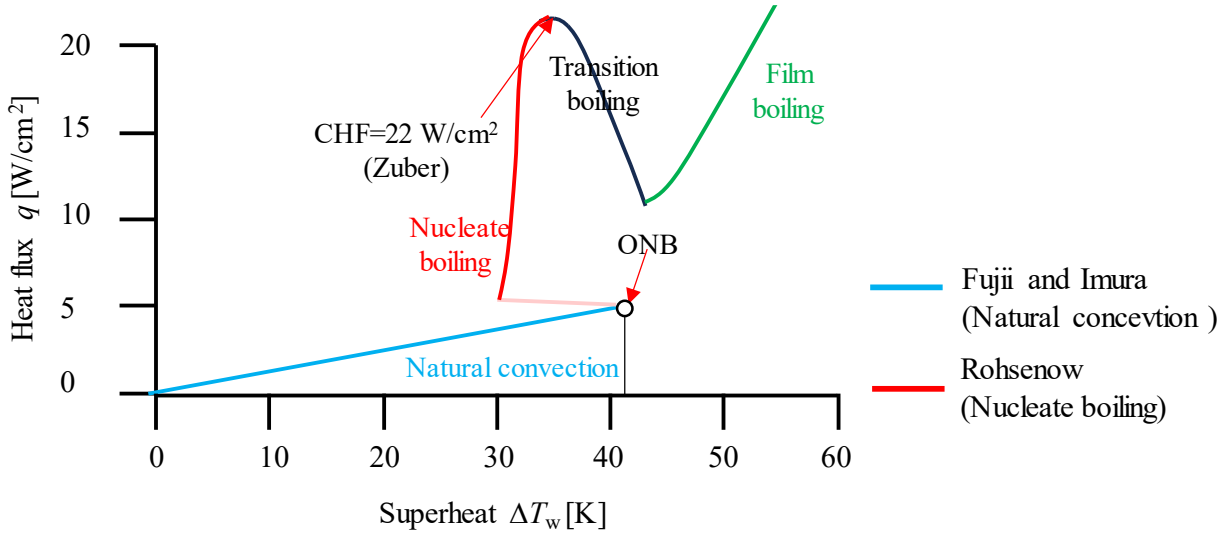

(b)

Fig. 1.3 (Continued).

The significant excess ΔT_{ONB} required to trigger nucleate boiling presents a major challenge for using this method in electronic cooling applications. Focus on reducing the superheat required for the ONB in immersion boiling cooling systems using dielectric liquid coolants, relevant research papers on dielectric liquid boiling and efforts to mitigate the high ΔT_{ONB} issue will be introduced in the next section.

1.2.2 Boiling Incipience and Stability

Studies of boiling incipience have shed light on the superheat required for nucleate boiling (ΔT_{ONB}), using high-speed photography of single nucleation sites and theoretical models. Especially, Fluorocarbon and Novec fluids are highly wetting fluids which result in an obvious higher ΔT_{ONB} and a high tendency for leakage [41-43]. Researchers have extensively investigated the aging effect on heat transfer surfaces, which is closely linked to the stability of nucleation sites during repeated boiling cycles. Zhou et al. [43] studied the effect of surface aging in submerged jet impingement boiling of PF 5020. They compared the results at two immersion times, 1 hour and 10 hours, and observed that the boiling curves shifted towards the left as the immersion time increased from 1 to 10 hours, indicating an improvement in the heat transfer coefficient with surface aging. This observation was supported by Ma and Bergles [44], who conducted submerged jet impingement experiments using R113. Based on these findings, it is highly recommended to consider the effect of surface aging when studying heat transfer phenomena involving boiling surfaces. In this study, the focus is on the

boiling incipience of dielectric liquids, and a review of boiling incipience is emphasized next.

The earlier study by Corty and Foust [39] conducted nucleate boiling experiments on a horizontal copper surface using three different liquids: refrigerant R-113, diethyl ether, and n-pentane. They prepared copper surfaces with varying degrees of roughness, ranging from 0.150 μm to 0.575 μm. They observed that rougher copper surfaces were more prone to earlier nucleation and boiling initiation, suggesting that the nucleation sites might originate from pits and scratches on the rougher surfaces. Later, employing techniques like scanning electron microscopy (SEM) and optical microscopy, researchers verified that the nucleation sites for boiling bubbles are indeed cavities or imperfections present on the surfaces. Clark et al. [45] examined a boiling surface under a microscope and observed that the bubbles do originate from cavities on the surface. Cornwell et al. [46-48] verified with a Scanning Electron Microscope that nucleate sites are typically cavities. Lorenz [49] provided electron micrographs (at 3000x magnification) showing the active cavity geometry on the surface, as depicted in Fig. 1.4. Based on these observations, a geometrical model was developed to relate the effective cavity size to the nucleation process, considering idealized conical cavities [49].

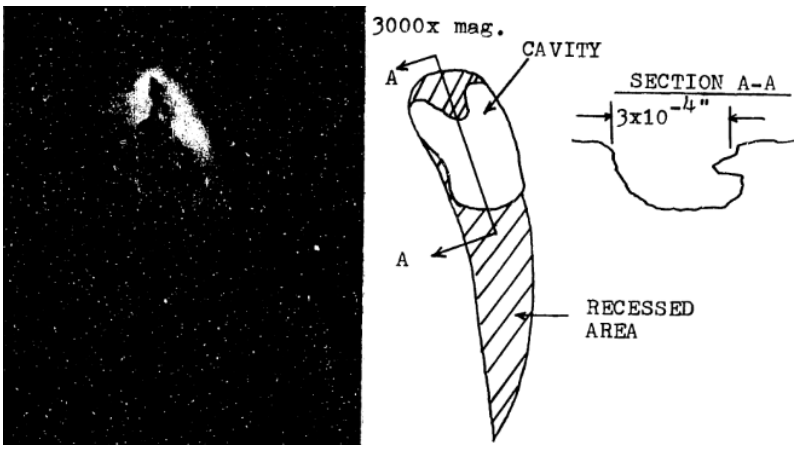

Fig. 1.4 Electron micrographs of nucleation cavities at 3000x magnification [49].

On the other hand, large superheat for triggering the ONB was found during the boiling process of the dielectric liquid. For instance, the experimental verification of the high superheat during the saturation of nucleate pool boiling on a copper surface in HFE-7100 showed that the surface temperature for the ΔT_{ONB} is approximately 75℃ [50, 51], which means the devices could be overshoot before the nucleate boiling region.

Many efforts have been made on enhancing nucleate pool boiling to reduce temperature excursion at incipient boiling and reduce the ΔT_{ONB} during nucleate dielectric boiling. Laser texturing [52-54] and chemical coating [55], have been widely used to promote boiling nucleation by providing large

amounts of activated nucleation cavities. Boiling of FC-72 was conducted on a surface texturing by a nanosecond fiber laser and the surface can provide multi-scale microcavities [52]. Enhanced and controlled boiling heat transfer was achieved on the laser textured surface [52]. Ho et al. [53] also conducted pool boiling experiments of FC-72 liquid on a selective laser melting to investigate the structure impact on the HTC. Su et al. [56] conducted pool boiling tests on graphene and fluorinated-graphene-coated surfaces, using R-141b as a working fluid. By providing a greater number of nucleation sites, superior heat transfer performance of the F-graphene-coated surface was attained.

Specifically, porous surfaces have been extensively tested for pool boiling of dielectric liquids [57-61]. For instance, microporous copper surfaces with cavity sizes ranging from 0.5 to 5 μm exhibited lower boiling incipience temperatures (ΔT_{ONB} = 3~11 K) during the nucleate pool boiling of HFE-7100 [60]. Similarly, an extremely lower superheat (ΔT_{ONB} = 0.5~0.8 K) for boiling incipience of HFE-7100 was found on a porous copper graphite with randomly sized cavities ranging from a few to hundreds of microns [61].

Significant reduce of the ΔT_{ONB} was achieved on various surfaces, another parrel investigation-aging effect of the ΔT_{ONB} was also draw our attention. Based on the gas entrapment criterion, a conical cavity was simply proposed by Bankoff [62], as shown in Fig 1.5. To trap gas, the contact angle should be greater than the cavity cone angle, i.e. $\theta > 2\beta$. As for the dielectric liquid, the contact angle was smaller than the water, the deeper cavity depth was required for trapping gas. However, in some cases, the cavity made by a deeper depth becomes inactive when restarting the boiling experiments for a while. For example, the pool boiling experiment of dielectric liquids (FC-72) demonstrated deactivated nucleation in cylindrical cavities, accompanied with an increasing ΔT_{ONB} of 30 K for restarting the boiling process [63]. The cylindrical cavities were assumed to be flooded by FC-72 and not enough to be more resistant against flooding [63]. For maintained the stable nucleation of dielectric liquid, reentrant microstructure was found to be able to provide a gas entrapment against immersion [64, 65].

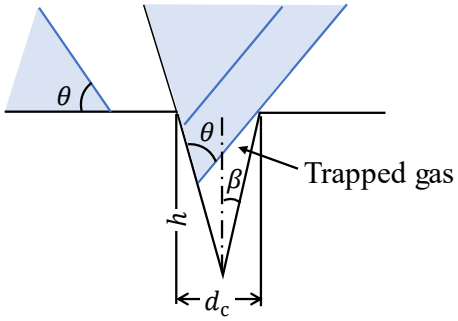

Fig. 1.5 Schematic drawing for entrapment of gas across a cavity.

A doubly reentrant cavity, as shown in Fig 1.6, was found to provide a stronger resistance against wetting and retain suspension, even if for the liquid with contact angle close to 0° [66].

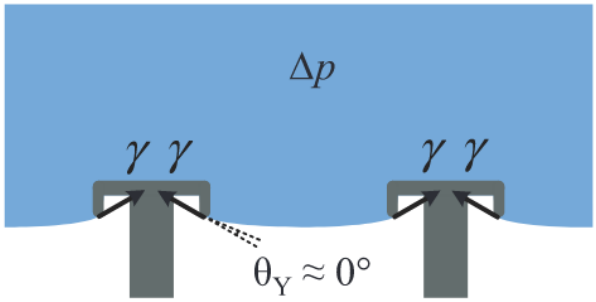

Fig. 1.6 Liquid suspension on doubly reentrant cavities [66].

In the investigation of nucleate boiling of FC-72 on re-entrant and doubly re-entrant cavities [63]. Nucleation on re-entrant cavities ceased early at a larger superheat, suggesting that FC-72 invaded the cavities during a bubble departure [63]. When heated after leaving the chips for ~5 minutes without nucleation, the doubly re-entrant cavities resumed nucleation at the temperature they ceased to nucleate during cooling. In stark comparison, the re-entrant cavities could not reactivate nucleation during the cooling process with a much larger superheat (~7 K). For the dielectrics with highly wetting ability, complicated cavities appear to be effective in maintain stable nucleation.

1.2.3 Hsu's model for prediction active cavity range

In this study, Hsu's model [67] was considered to confirm the active cavities range based on the superheat for incipience boiling. On real engineering surfaces, there exists a range of cavity sizes that can be activated at a fixed wall superheat value, rather than just a single size. To provide a practically feasible prediction from a surface engineering perspective. Hsu [67] proposed a nucleation criterion that depends on the thermal boundary layer characteristics at the heated wall. As seen in Fig. 1.6, the embryo bubble starts from an existing cavity (truncated sphere) on the heated surface when the liquid temperature T_l in the region close to the heated surface (thermal boundary layer) is equal to the bubble temperature T_b. The liquid temperature T_l was a linear temperature gradient within the liquid thermal boundary layer, as shown in the following equation:

$$T_l - T_{\text{sat}} = (T_{\text{w}} - T_{\text{sat}})(1 - \frac{z}{\delta_{\text{T}}}) \tag{1.1}$$

And the bubble temperature was calculated based on the Young-Laplace equation for a spherical bubble. The corresponding saturation temperature inside the bubble can be approximately found from the Clausius-Clapeyron equation as:

$$T_b - T_{\text{sat}} = \frac{2\sigma T_{\text{sat}}}{r_b \rho_v h_{fg}} \tag{1.2}$$

Hsu et.al assumed that the temperature T_{b} at which the height of the embryo bubble h_{b} is sufficiently large to maintain the growth of the bubble. Then, he obtained the following relation:

$$d_{\text{c}} = \delta_{\text{T}} \cdot \frac{\sin\theta \cdot (T_{\text{w}} - T_{\text{sat}})}{(1 + \cos\theta) \cdot (T_{\text{w}} - T_{\text{sat}})} \cdot \left[1 \pm \sqrt{1 - \left(\frac{8 \cdot (1 + \cos\theta) \cdot \sigma \cdot T_{\text{sat}}}{h_{\text{fg}} \cdot \rho_{\text{v}} \cdot \delta_{\text{T}} \cdot (T_{\text{w}} - T_{\text{sat}})}\right)}\right] \tag{1.3}$$

This correlation provides a range of nucleation cavity radii for which the cavity may be considered activated or inactive. In a verification experiment, Hsu found that the calculated δ_{T} (ΔT_{ONB} = 5 K) is 0.608 mm for water, and he suggested that δ_{T} may not be always the same for all cases.

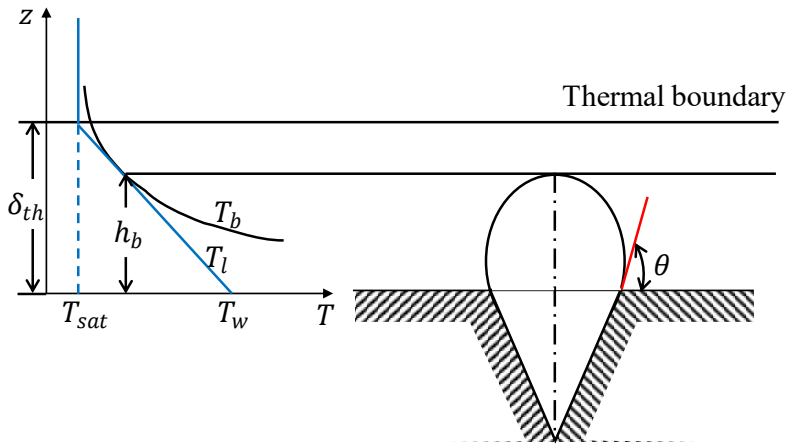

Fig. 1.7 Simplified schematic of Hsu's nucleation model.

1.3 Scientific Significance

According to the research motivation and background, in this work, we

1. Develop a pool boiling experiments apparatus capable of simultaneously capturing top surface temperature distribution and boiling behavior through the integration of an infrared camera and high-speed video technology.

2. Achieve a significant decrease in the surface superheat of the ONB during the initial test of saturated pool boiling of AE-3000 liquid through three types of the HPPs, comparing with the plain surface - indium-tin oxide (ITO) heater surface.

3. Evaluate the effectiveness of the pore size distribution (PSD) of the three types of the HPPs in reducing the surface superheat of the ONB and enhancing the heat transfer coefficient (HTC).

4. Develop a coupled section combining the HPP and a metal fine film with a small input power to effectively resolve the deteriorated surface superheat of the ONB issues encountered during the restarting boiling experiment following prolonged immersion periods.

1.4 Outline of the thesis

To comprehensively understand the current and historical interest in this work, Chapter 1 provides the research background that guides the future direction of this work. With the aim of maintaining surface temperatures for boiling incipience within safe operational limits (85 ºC) for electronic devices, experiments were designed and conducted as follows. In Chapter 2 boiling performance on various HPPs was investigated. Three kinds of HPPs were manufactured with different cavity ranges. The cavities are designed in a pore size distribution (PSD) with peak pore diameters of 0.2 μm (0.004~0.9 μm), 0.9 μm (0.004~4.8 μm) and 0.6 μm (0.004~20.8 μm), respectively. The surface superheat for the ONB (ΔT_{ONB}), and detailed surface superheat distribution under the ΔT_{ONB} condition, HTC performance and cavity geometry effect on the ΔT_{ONB} was studied. Models for the ΔT_{ONB} prediction previous published, introduced earlier in Chapter 2 was compared with our experimental results. In a restarting experiment after immersing the HPP samples into the liquid for a long period, the deteriorated ΔT_{ONB} was found on certain HPP sample (0.004~0.9 μm). In Chapter 3, a hybrid section combined the HPP (0.004~0.9 μm) and a metal fine film was introduced. Stability of the bubble nucleation was studied. Continuous and discontinuous voltage was applied to the heated film. Besides, a comparative study was also conducted by applying different patterns of the discontinuous heated film voltage. Final conclusions and a short outlook on future work are given in Chapter 4.

CHAPTER 2

Effects of Pore size distribution of a Honeycomb Porous Plate on the Onset of Nucleate Boiling of AE-3000

In this chapter, a honeycomb porous plate (HPP) was utilized to improve the performance of saturated pool boiling of dielectric liquids. As the working fluid, a fluorinated dielectric of AE-3000 has been selected. Three kinds of HPPs were manufactured with different cavity ranges. The cavities are designed in a pore size distribution (PSD) with peak pore diameters of 0.2 μm (0.004~0.9 μm), 0.9 μm (0.004~4.8 μm) and 0.6 μm (0.004~20.8 μm), respectively. The relationship between the superheat required for the onset of nucleate boiling (ΔT_{ONB}) and the PSD of the HPPs was investigated experimentally. The HPP was attached on an indium-tin oxide (ITO) heating surface to meaure the boiling curves. In boiling curves, the averaged ΔT_{ONB} and local ΔT_{ONB} was measured using a 2D IR thermography. The results indicated that not only the peak diameter of the cavities but also the overall cavity size distribution, especially the presence of larger-sized cavities, influenced the superheat required for the ΔT_{ONB}. What's more, stability of the ΔT_{ONB} on these HPPs were also considered by performing restarting boiling experiments after immersing the HPPs into AE-3000 for 48 hours. After 48-hour immersion, the HPP with the smallest pores (Peak diameter: 0.2 μm) showed increased average averaged ΔT_{ONB} by 6.7 K and the local ΔT_{ONB} ranging from 18.0 K to 33.0 K due to cavity deactivation. In contrast, other HPPs with larger pores maintained stable performance. Later, comparing the surface superheat for the boiling incipience and Hsu's model, active cavities range for boiling nucleation was confirmed. Results indicate that HPPs with larger cavities, particularly those with re-entrant structure, provide more stable and reduced ΔT_{ONB}, enhancing immersion cooling efficiency for electronic devices.

2.1 Experimental apparatus and procedures

2.1.1 Working fluid

The working liquid, AE-3000 (AGC Co. Ltd), had similar thermophysical characteristics with Fluorinert™ electronic liquids and Novec engineered fluids [68-71], as illustrated in Table 2.1, which also includes the molecular structures.

Table 2.1 Thermophysical properties of AE-3000, FC-72 and HFE-7100 [68-71]

	AE-3000	FC-72	HFE-7100
Molecular structure	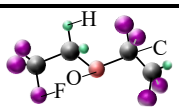	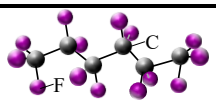	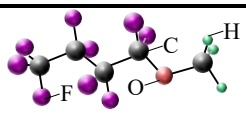
Molecular Formula	$CF_3CH_2OCF_2CF_2H$	C_6F_{14}	$C_4F_9OCH_3$
Electric Conductivity (S/m)	7.7×10^{-4}	1.0×10^{-15}	7.0×10^{-10}
Boiling point (℃)	55.0	56.0	59.8
Latent heat (kJ/kg)	147.2	88.0	112.0
Specific heat (J/kg·K)	1336	1100	1253
Liquid density (kg/m^3)	1395.1	1680	1405
Liquid viscosity (mPas)	0.43	0.38	0.38
Vapor density (kg/m^3)	7.7	11.7	9.7
Surface tension (mN/m)	12.2	10.0	11.1

2.1.2 Experimental apparatus

A schematic of the pool boiling test facility used for the present work is shown in Fig. 2.1. The facility consisted of a boiling chamber (internal diameter of 82 mmΦ and height of 150 mm) made of borosilicate glass, heating system, condenser, voltage supply, and measurement facility. An auxiliary sheathed heater was immersed in the bulk liquid to maintain the desired saturation of the working fluid. The condenser was cooled by circulating water chilled by a refrigeration system to reduce the evaporation loss of AE-3000 and maintain the liquid level at approximately 60 mm above the boiling surface during the experiments. A calibrated K-type thermocouple (1 mm in diameter and with a measurement error of ±0.1 K) was placed just next to the heating surface to measure the liquid temperature. For each experiment, saturated temperature of the working liquid was confirmed.

In the experiments, a thin film made of indium–tin oxide (ITO) was used as the heater and boiling occurred on the upward-facing side of this film. As shown in Fig. 2.2 (a)-(c), the ITO heater was constructed with three layers, namely, a sapphire substrate (40 mm × 40 mm), the ITO film (active area: 10 mm × 10 mm), and a TiO_2 layer, with the respective thicknesses of 1 mm, 250 nm, and 100 nm. ITO film was deposited by ion-plasma sputtering onto the sapphire substrate. The gold pads made by Cr (30 nm thick) and Au (200 nm thick) electrodes were deposited sequentially onto the ITO film and were connected to a DC power supply with a maximum output power of 1.2 kW. The gold pads are used to define the active heating area (~10 × 10 mm, red trait in the Fig. 2.2 (b)). The accuracy of the DC power supply at maximum output value was ±10 mV. Current of the heater was measured through a shunt resistance (2.5 mΩ) with a manufacturer-specified accuracy of 0.2% and voltage was directly measured through electrodes (gold electrodes) of the ITO layer. Thus, Joule heating per unit

area of the ITO heater can be calculated as:

$$q = \frac{V(t) \cdot I(t)}{A} \tag{2.1}$$

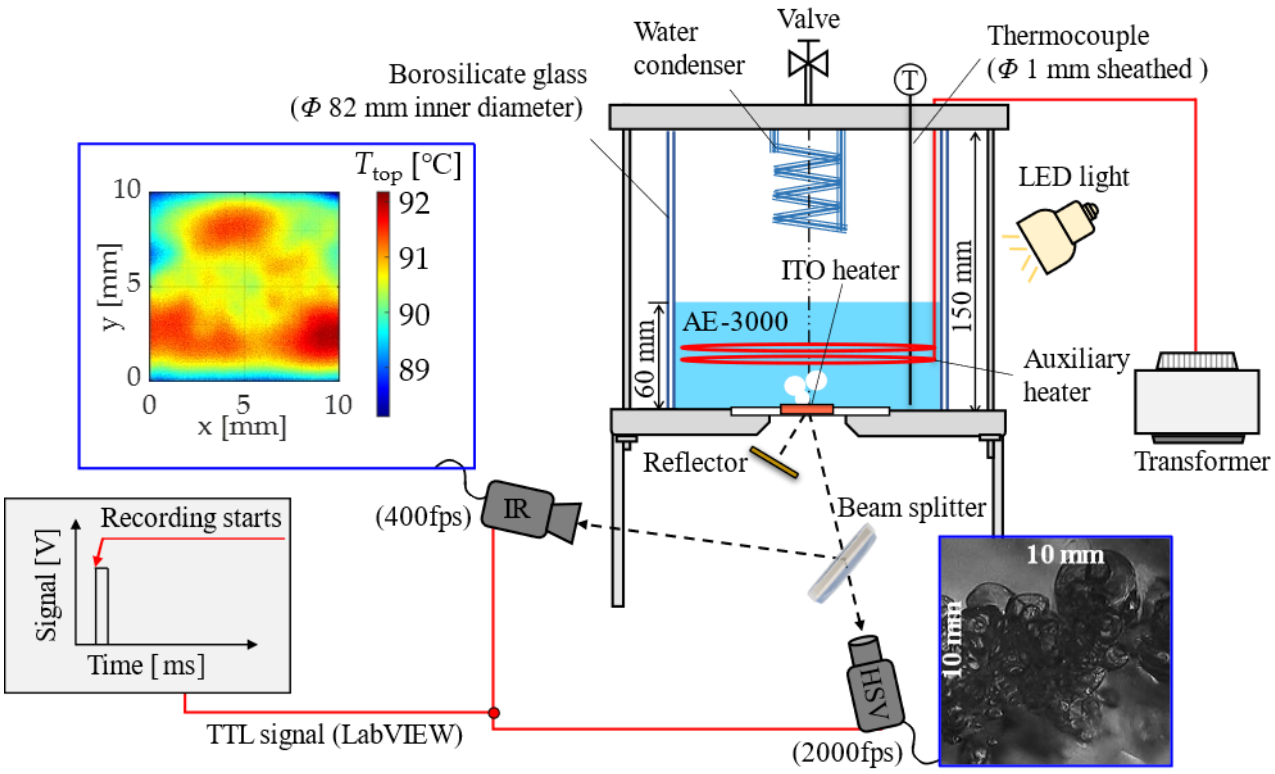

Fig. 2.1 Schematic illustration of the experimental facility.

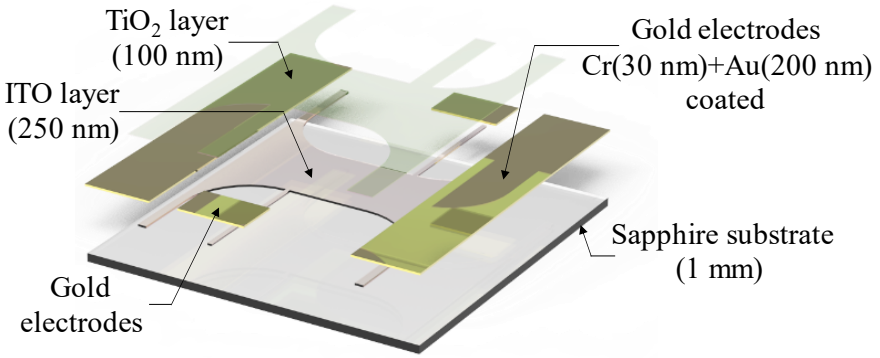

(a)

Fig. 2.2 (a) ITO heater sections, (b) relevant dimensions of the ITO heater, (c) circuit description of the ITO heater.

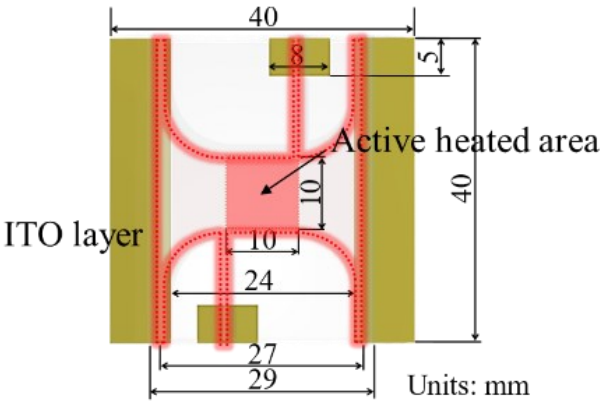

(b)

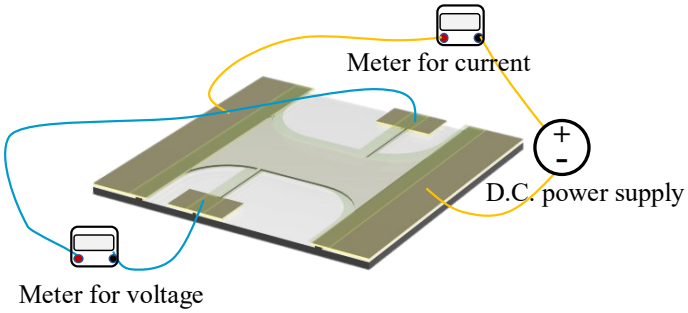

(c)

Fig. 2.2 (Continued).

Besides, a layer of TiO_2 with a thickness of 100 nm was applied above the top surface of the ITO heater on which boiling occurred to increase wettability. AE-3000 liquid contact angle on the TiO_2 layer and ITO layer was measured, the results showed that contact angle was almost same on these two layers (variation was about 1º). Finally, our measurements showed that the contact angle of the AE-3000 liquid drop on the TiO_2 layer was approximately 10.7º. Measured contact angle on the TiO_2 layer and ITO layer was shown in Fig. 2.3.

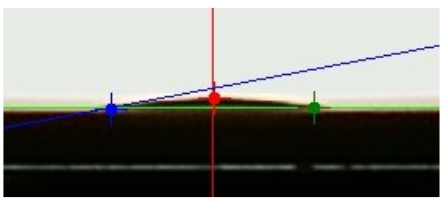

TiO_2 layer
10.71º

(a)

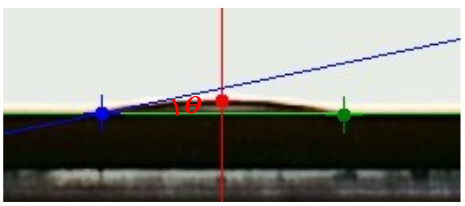

Sapphire layer
11.75º

(b)

Fig. 2.3 Measurement of the contact angle (a) contact angle on the TiO_2 layer of the ITO heater and (b) contact angle on the ITO heating surface without TiO_2 layer.

Then, roughness of the ITO layer was measured by stylus profilometer (Dektak XT). The measured arithmetic average of the surface height deviation R_a and root mean square roughness R_q were 9.4 and 12.1 nm, respectively. Thus, the bare ITO layer was classified as a nano-smooth surface with no microcavities that could act as nucleation sites. Roughness data of the ITO layer was shown in Fig. 2.4.

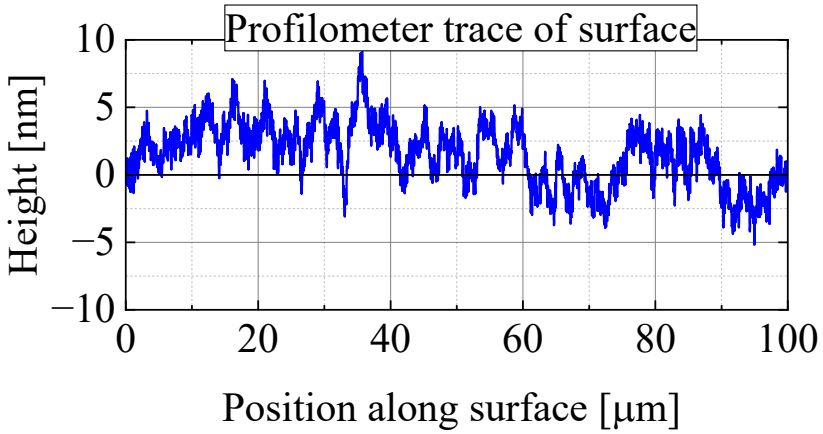

Fig. 2.4 Cross-sectional roughness of the ITO heater surface.

2.2.3 Honeycomb Porous Plate (HPP)

Boiling experiments were performed on two different surface sections: a plain surface, the honeycomb porous plate. The assembly configuration of the HPP attached to the ITO layer (plain surface) is illustrated in Fig. 2.5. The HPP was fixed to the top of the ITO layer by nylon wires with an outer diameter of 0.8 mm, actual section for the HPP fixed on the ITO heater was shown in the right side of the Fig. 2.5.

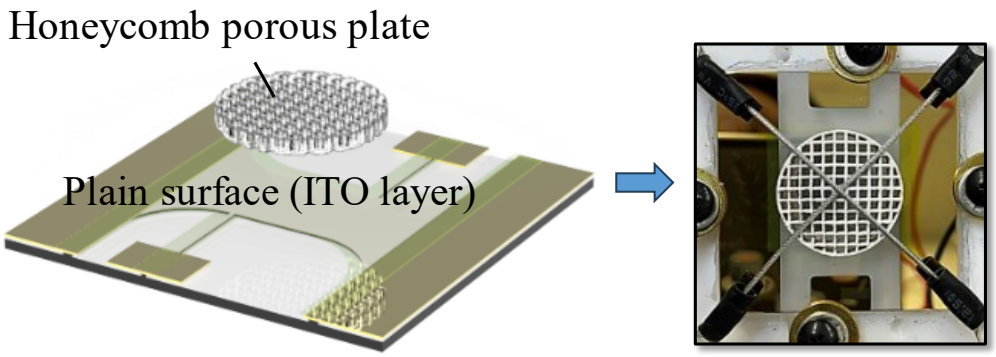

Fig. 2.5 Installation of the HPP on the ITO layer.

Despite efforts to achieve a tight fixing, the presence of a gap between the HPP and the ITO film was unavoidable. Laser microscopy measurements of the HPP surface revealed a roughness profile ranging from -15 to 27 μm. Consequently, the maximum potential gap between the HPP and the ITO heating surface is estimated to be 42 μm. It is hypothesized that this narrow gap formed between the HPP and the ITO film exhibits lower thermal resistance compared to the bulk liquid. As a result, the liquid within this confined region is expected to heat more rapidly, potentially leading to earlier nucleation with a reduced ΔT_{ONB}.

The structural details of the HPPs are depicted in Fig. 2.6 (a), (b) and (c). Circular HPPs with same thickness of 5 mm and different outer diameters of 15 mm (HPP2 and HPP3) and 20 mm (HPP1) were employed in this study. The HPP with a diameter of 20 mm featured vapor escape channel width (equivalent to the cell width) of 1.4 mm and grid wall of 0.5 mm. Similarly, the 15 mm diameter HPP consisted of 1.0 mm width vapor escape channels and 0.35 mm width grid walls. The aperture ratio (the ratio of the open area to total area) for each HPP was 0.72 (diameter: 20 mm) and 0.36 (diameter: 15 mm), respectively.

Scanning electron microscopy (SEM) was used to examine the top surface. For example, large amounts of cavities could be observed on the top surface of these HPPs, as shown in Fig 2.6 (a), (b) and (c). However, the shape of cavities inside the HPP1 and HPP2 were unable to be measured due to the limit of resolution of optical microscopes. In the HPP3, re-entrant cavities were able to be found by microcomputer tomography. 3D description of the cavities inside the HPP3 was illustrated in Fig. 2.6 (c). Re-constructed 3D models of the scanning images have confirmed that re-entrant cavities were formed in the HPP3. More 3D models of the HPP3 from the scanning images were supplied in Appendix A.

Due to the limited accuracy of the microscopy for observing the pore size of HPP1 and HPP2, the PSD of all the HPPs was measured by mercury penetration porosimetry (mercury contact angle: 140°). During the process of mercury penetration porosimetry, mercury is incrementally forced into the pores of a sample under increasing pressure. The pressure applied to force mercury into the pores is inversely related to the pore diameter according to the Washburn equation. The initial data collected is usually in the form of intruded volume. To get detailed insights into the distribution of pore sizes, the first derivative of the intruded volume with respect to the logarithm of the pore diameter is calculated $dV_{pore}/d(\log d)$. Finally, the data was normalized per unit mass. The weight of the testing sample was 2.5 g in my study. PSD were represented in Fig. 2.6 (d). Porosity for the three HPPs was nearly same, from 19% to 20%. The primary difference among the HPPs was the pore size, with peak pore diameters of 0.2 μm, 0.9 μm and 0.6 μm for HPP1, HPP2 and HPP3, respectively. Additionally,

the average pore diameters $d_{avg.}$ for each HPP were 0.03 µm, 0.5 µm and 0.2 µm, respectively. Median pore diameter at which half of the total pore volume is filled with mercury for the three HPPs are 0.1 µm, 0.8 µm and 0.6 µm. Size parameter and PSD of the HPPs were summarized in Table 2.2.

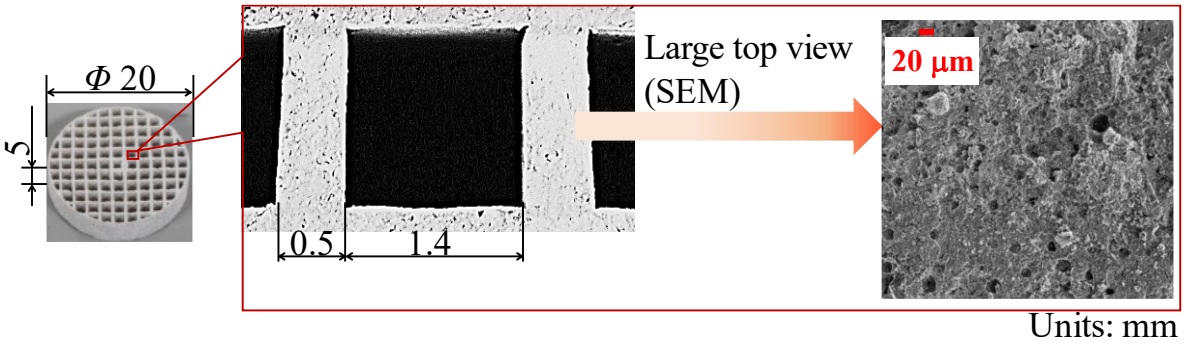

(a)

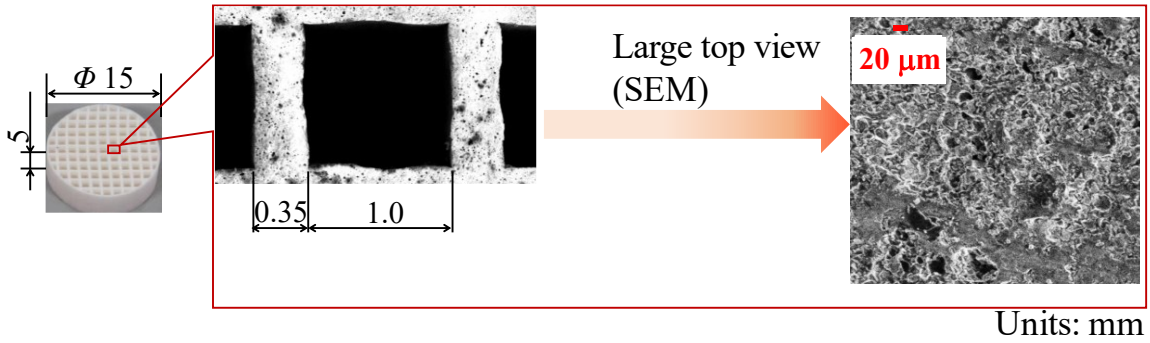

(b)

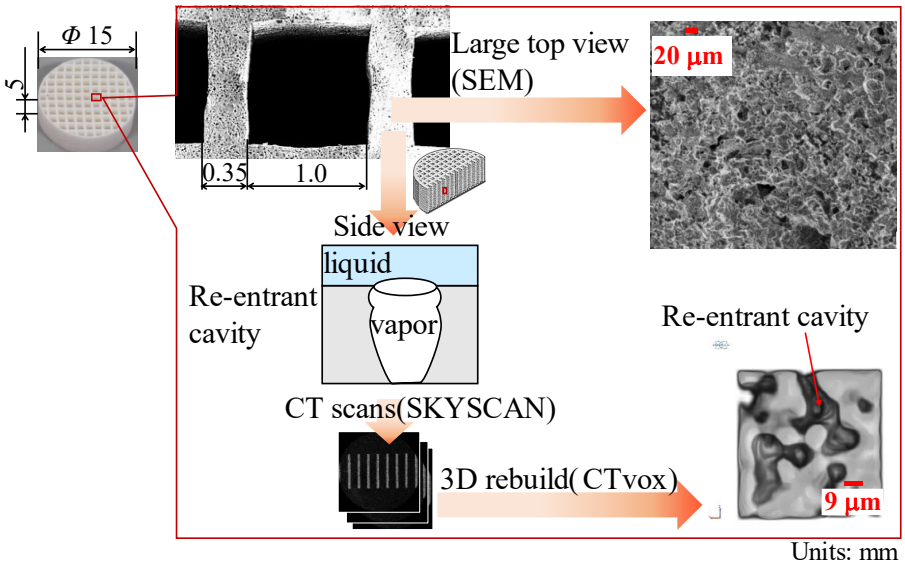

(c)

Fig. 2.6 (a) description of the HPP1 with conical cavities (diameter: 20 mm), (b) description of the HPP2 (diameter: 15 mm) and (c) description of the HPP3 with re-entrant cavities (diameter: 15 mm) (d) pore size distributions determined by mercury porosimetry.

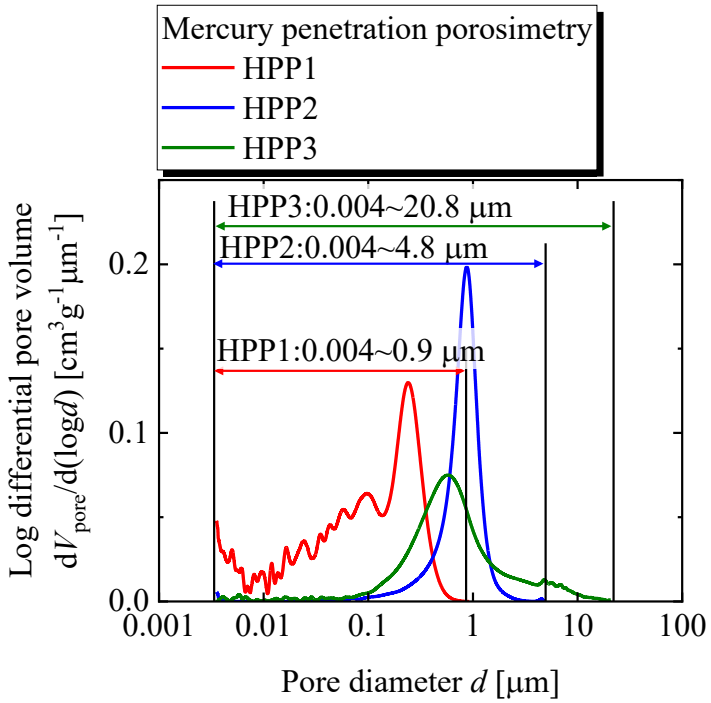

(d)

Fig. 2.6 (Continued).

Table 2.2 Pore information of the HPPs

HPP	D_{HPP} (mm)	PSD (μm)					Porosity
		d_{max}	d_{min}	$d_{avg.}$	Median	Peak	
HPP1	20	0.9	0.004	0.03	0.1	0.2	19%
HPP2	15	4.8	0.004	0.5	0.8	0.9	19%
HPP3	15	20.8	0.004	0.2	0.6	0.6	20%

2.2.4 Experimental procedure

AE-3000 (AGC Co. Ltd) was poured into the boiling chamber through the top valve until the interface was 60 mm above the boiling surface. The working fluid AE-3000 was boiled at a moderate heat flux (2.3 W/cm^2) by a 200 W preheater for 2 h under saturated conditions to remove any leftover trapped gas because the presence of dissolved gas lowers ΔT_{ONB} [72-75]. Then, heat flux was provided by an ITO heater with a current interval of 0.5 A until 12 W/cm^2 (typically ~60% of the estimated CHF value). Waiting period for each current was set as 60s to reach the quasi-steady state. The two-dimensional temperature of the backside of the boiling surface was captured by the IR camera. During experiments, the liquid temperature was maintained at the saturation temperature under atmospheric pressure by opening the top valve above the condenser.

Heat loss through the ITO heater was estimated by three-dimensional steady heat conduction

equation. Given the z-axis (thickness direction) temperature profile, the heat flux from the ITO heater to AE-3000 liquid can be calculated by Fourier conduction law as given:

$$q_{\mathrm{w}} = q - k_{\mathrm{s}}(T_{Top})\frac{T_{Top} - T(z_{\mathrm{top}} - z_{\mathrm{c}})}{z_{\mathrm{c}}} \tag{2.2}$$

where z_{top} is the z-coordinate of the top surface, the z_{c} is the distance between the top surface and the center of the adjacent cell in the z-direction, the mesh size of z_{c} is 50 μm. k_{s} is temperature-dependent thermal conductivity related to the top surface temperature [76-79].

Based on the calculated results, deviation of the backside and topside surface was smaller than 1.0 K. Top surface superheat ($\Delta T_{\mathrm{w}} = T_{\mathrm{top}}$-$T_{\mathrm{sat}}$) and heat flux from the ITO heater to the AE-3000 liquid (q_{w}) were used in boiling curves. Calculation of the ITO heater including calculation domain setting, boundary condition and deviation of the backside and topside surface under different heat flux condition were shown in Appendix B.

2.2.5 Uncertainty analysis

The overall uncertainty was calculated by combining the individual standard uncertainty using the following equation [80]:

$$\Delta u = \sqrt{\sum_{i=1}^{M}(\frac{\partial u}{\partial m_i}\Delta m_i)^2} \tag{2.3}$$

where Δu is the overall uncertainty, m_i is the individual standard uncertainty parameter considered, M is the total number of uncertainty parameters considered, and Δm_i is the individual standard uncertainty for m_i, respectively. Heat flux uncertainty Δq is evaluated by taking account of voltage and current of the ITO heater. The maximum output accuracy of the DC power supply was ±10 mV. The uncertainty of the current was 0.2%. Based on these uncertainties, the maximum uncertainty of heat flux measurement was estimated as 0.02 W/cm^2 using the following equation:

$$\frac{\Delta q}{q} = \sqrt{(\frac{\Delta V}{V})^2 + (\frac{\Delta I}{I})^2} \tag{2.4}$$

Uncertainty analysis of heat flux was summarized in Table 2.3.

Table 2.3 Uncertainty analysis of heat flux.

V [V]	I [A]	q [W/cm^2]	Δq / q [%]	Δq [W/cm^2]
2.030	0.344	0.698	0.532	0.004
5.810	0.981	5.684	0.264	0.015
8.298	1.404	11.6	0.234	0.003

2.2 Results and discussion

2.3.1 Boiling Curves on the plain surface

Boiling curves obtained with the plain surface are presented in Fig. 2.7 (a). The boiling curves demonstrated the excellent reproducibility of the experimental data over three runs under the same operating conditions. The horizontal arrows labeled "NC" represent the extent of the natural convection regime before the nucleate boiling regime. The natural convection regime was single-phase convection; thus, the heat transfer coefficient was low. As the heat flux increases, the heat transfer regime transits from natural convection regime to the nucleate boiling regime. The transition point is called the ONB point (ΔT_{ONB}) which is defined the reduction of the average wall temperature sharply.

Beyond the ΔT_{ONB}, the curve enters the nucleate boiling regime, where the heat flux continues to increase with a relatively smaller increase in surface superheat, reflecting the enhanced heat transfer performance of the nucleate boiling process. As described in the Chapter 1, AE-3000 has high wetting ability (Contact angle between the AE-3000 liquid drop and the TiO_2 layer was approximately 10º in our measurements). This liquid trend to flood surface cavities for nucleation and consequently high surface superheat was required for nucleation. Figure 2.7 (b) illustrates the bottom HSV of a plain surface prior to boiling occurring. Synchronized surface superheat distribution was shown in Fig 2.7 (c) and uniform high surface superheat distribution was found within the averaged ΔT_{ONB} was 49.8 K. When heat flux was increased further, large bubbles began forming, as evidenced by bottom HSV of Fig 2.7 (d). Meanwhile, a sharp surface superheat drop occurred, the surface superheat ΔT_w reduced from 49.8 K to 31.7 K.

Hsu's correlation [67] was considered to confirm the relationship between the active cavity range and ΔT_{ONB} on the plain surface. The correlation was given as:

$$d_c = \delta_T \cdot \frac{\sin\theta \cdot (T_w - T_{sat})}{(1+\cos\theta)\cdot(T_w - T_{sat})} \cdot \left[1 \pm \sqrt{1 - \left(\frac{8\cdot(1+\cos\theta)\cdot\sigma\cdot T_{sat}}{h_{fg}\cdot\rho_v\cdot\delta_T\cdot(T_w - T_{sat})}\right)}\right] \tag{2.5}$$

where the contact angle θ of 10.7º was obtained by measuring the contact angle after dropping the AE-3000 liquid drop on the TiO_2 layer. And the thickness of the thermal boundary layer δ_T is calculated from the Fourier's heat conduction as given:

$$q_{\mathrm{w}} = k_{\mathrm{l}} \frac{T_{\mathrm{w}} - T_{\mathrm{sat}}}{\delta_{\mathrm{T}}} \tag{2.6}$$

Where k_{l} is the liquid thermal conductivity. The surface temperature for boiling incipience T_{ONB} ($\Delta T_{\mathrm{ONB}} + T_{\mathrm{sat}}$) and corresponding heat flux were put into T_{w} and q_{w} to calculate the thickness of the thermal boundary δ_{T} for triggering boiling. For example, boiling on the plain surface, the ΔT_{ONB} was 49.8 K and corresponding heat flux q_{w} was 6.0 W/cm^2. Based on the equation 2.6, the thickness δ_{T} was 68 μm.

Calculated range of active cavities was shown in the left-hand side of Fig. 2.8. Cavities ranging inside the curve was considered as active for nucleation and outside was non-active for nucleation. Based on the averaged ΔT_{ONB} (49.8 K), the diameter range of the active cavity was 0.056~23.849 μm. However, in our roughness measurement of the plain surface, the arithmetic average of the surface height deviation R_{a} and root mean square roughness R_{q} were 9.4 and 12.1 nm, respectively. These values indicate that the cavities on the plain surface lie in the non-active region at the ΔT_{ONB} of 49.8 K, suggesting a higher ΔT_{ONB} would be required for nucleation from these small-scale cavities. It is noteworthy that a smooth surface, as indicated by small R_{a} or R_{q} can also have a lot of cavities for nucleation. Many researchers reported the inadequacy of using an individual statistical parameter to characterize the surface roughness for pool boiling [81-83]. And Matteo et al. [84, 85] has employed an optical microscope to measure the condition of the ITO film. The scanning electron microscope (SEM) image showed rare imperfections on the ITO film in the micro-order range, which is consistent with the calculated minimum diameter of the active cavities.

Next, we compared our results with calculations obtained by using empirical formulas found in two-phase textbooks [86]. Here Fujii and Imura's correlation [87] was used to fit the experimental data for the natural convection regime. The rewritten version of Fujii and Imura's correlation is given as:

$$Nu = C_1 Ra^n \tag{2.5}$$

$$Ra = GrPr = \frac{g\beta(T_{\mathrm{w}} - T_{\infty}){D_{\mathrm{h}}}^3}{\nu_{\mathrm{l}}\alpha} \tag{2.6}$$

$$D_{\mathrm{h}} \equiv \frac{4A}{L} \tag{2.7}$$

where L in equation 2.7 was the perimeter of the heating ITO film.

For a horizontal heated plate facing upward with a large Rayleigh Number in our study (Ra > 10^7), the flow was considered as turbulent flow, the value of the exponent n was 1/3 and the coefficient C_1 was found ranging from 0.13 to 0.31 in earliest studies [87-90]. In this study, the constant coefficient C_1 was equal to 0.31, which was also used in Zuber's boiling data [89]. Theoretical fitting curve was represented by a dashed-dotted black curve in Fig. 2.7 (a) with a ±15% deviation indicated by the black shadow.

Rohsenow's correlation [91] (dashed-dotted green curve in Fig. 2.7(a)) is preferred for the nucleate boiling region, the rewritten version of Rohsenow's correlation is given as

$$\frac{C_{\mathrm{p,l}}\Delta T_{\mathrm{w}}}{h_{\mathrm{lv}}} = C_2 \left[\frac{q_w}{\mu_{\mathrm{l}} h_{\mathrm{lv}}} \sqrt{\frac{\sigma}{g(\rho_{\mathrm{l}} - \rho_{\mathrm{v}})}} \right]^{0.33} \left(\frac{C_{\mathrm{p,l}}\eta_{\mathrm{l}}}{k_{\mathrm{l}}} \right)^{C_3} \tag{2.8}$$

Where $C_{p,\mathrm{l}}$ denotes the liquid specific heat at constant pressure, h_{lv} is the latent heat of vaporization, μ_{l} is the liquid dynamic viscosity, and k_{l} is the liquid thermal conductivity. Note that the parametric constants C_2 = 0.0045 and C_3 = 1.47 were chosen for the fluid-surface combination of ethanol and chromium [92]. In this study, C_2 = 0.005 and C_3 = 1.7 were used and the deviation between the experimental data and theoretical formula is approximately ±5% as shown in green shadow in Fig. 2.7 (a). Given that this difference is of an acceptable magnitude, the pool boiling apparatus and data regression approach are adequate for further study.

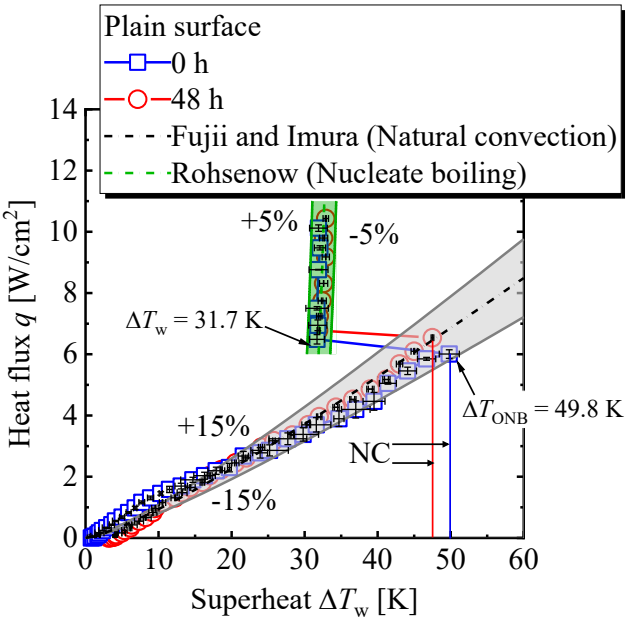

(a)

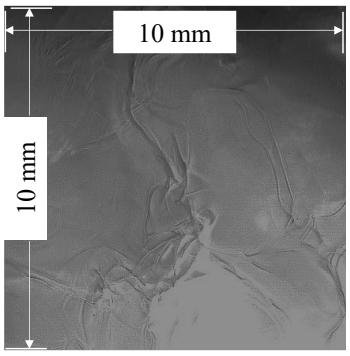

(b) ΔT_w = 49.8 K; q_w = 6.0 W/cm^2

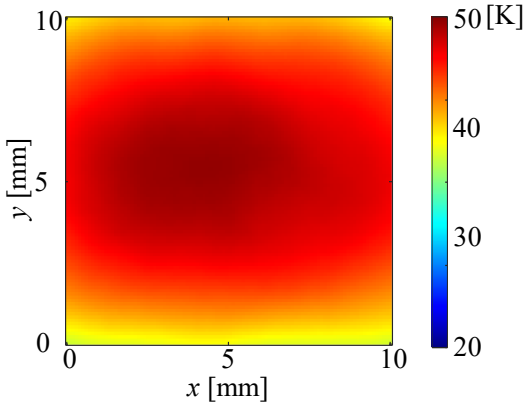

(c) ΔT_w = 49.8 K; q_w = 6.0 W/cm^2

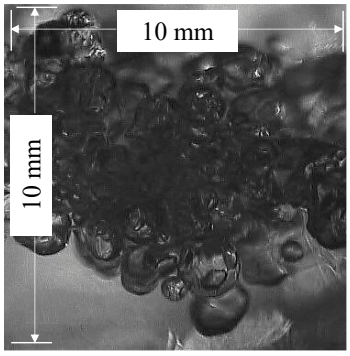

(d) ΔT_w = 31.7 K; q_w = 6.3 W/cm^2

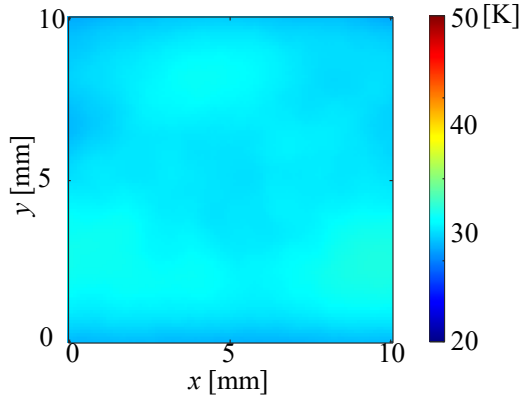

(e) ΔT_w = 31.7 K; q_w = 6.3 W/cm^2

Fig. 2.7 Fig. 2.7 (a) Boiling curve on the plain surface (b) HSV image at the ΔT_{ONB} (c) surface temperature distribution at the ΔT_{ONB} (d) HSV image after boiling occurred (e) surface temperature distribution after boiling occurred.

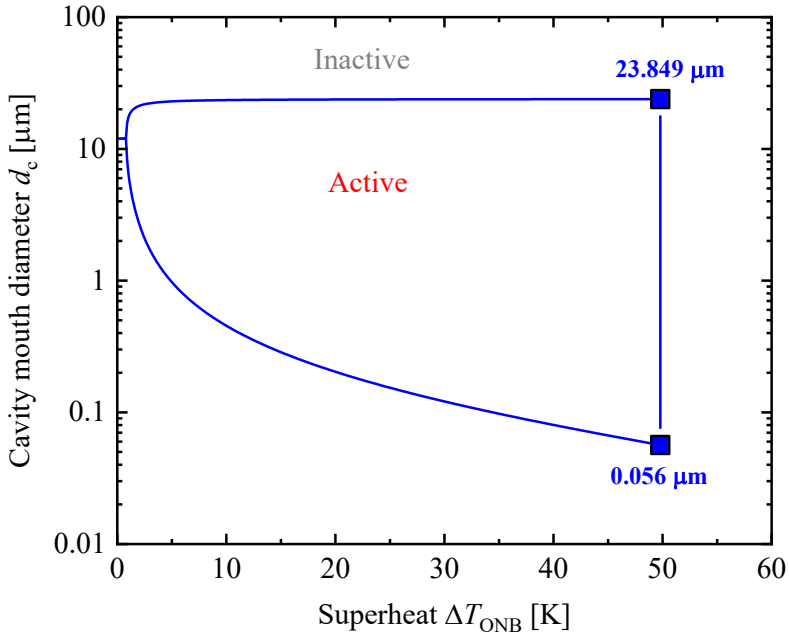

Fig. 2.8 Dependence of the range of the cavity diameter of the plain surface on the ΔT_{ONB} (Hsu model).

2.3.2 Boiling performance on the HPP1

Figure 2.9 presents the obtained boiling curves of AE-3000 on the HPP1. The boiling curve on the plain surface is also provided for comparison. In the natural convection regime, a unique bubble behavior, named local boiling, was observed. For example, in Fig. 2.9 (a), clusters bubble nucleation was observed in 4 cells of the HPP1 under the heat flux of 1.8 W/cm^2. Under this condition, significant wall temperature change over the entire surface through the measuring window of the IR camera (10 mm × 10 mm) was not observed. The surface superheat for triggering such occurrence of bubbles was considered as the local ΔT_{ONB} (local ΔT_{ONB} = 16.7 K) to define local boiling phenomenon during experiments. With the increase of the surface temperature, boiling cells were spreading, and a wall temperature drop over the entire surface was observed under the heat flux of 2.8 W/cm^2 as shown in Fig. 2.9 (b). In the boiling curves of Fig. 2.9, the averaged surface superheat ΔT_w was decreased from 19.7 K to 13.8 K. Finally, boiling occurred in entire cells of the HPP1, as shown in Fig. 2.9 (c).

Comparing boiling curves of the HPP1 and plain surface, lower surface superheat for the boiling incipience was achieved on the HPP1. The ΔT_{ONB} was reduced by 30.1 K on the HPP1 compared with that of the plain surface (ΔT_{ONB} = 49.8 K). For the HPP1, the local ΔT_{ONB} was approximately 16.7 K and the ΔT_{ONB} was approximately 19.7 K. By increasing nucleation cavities using the porous plate –

HPP1, the boiling incipience of dielectric liquid was significantly reduced.

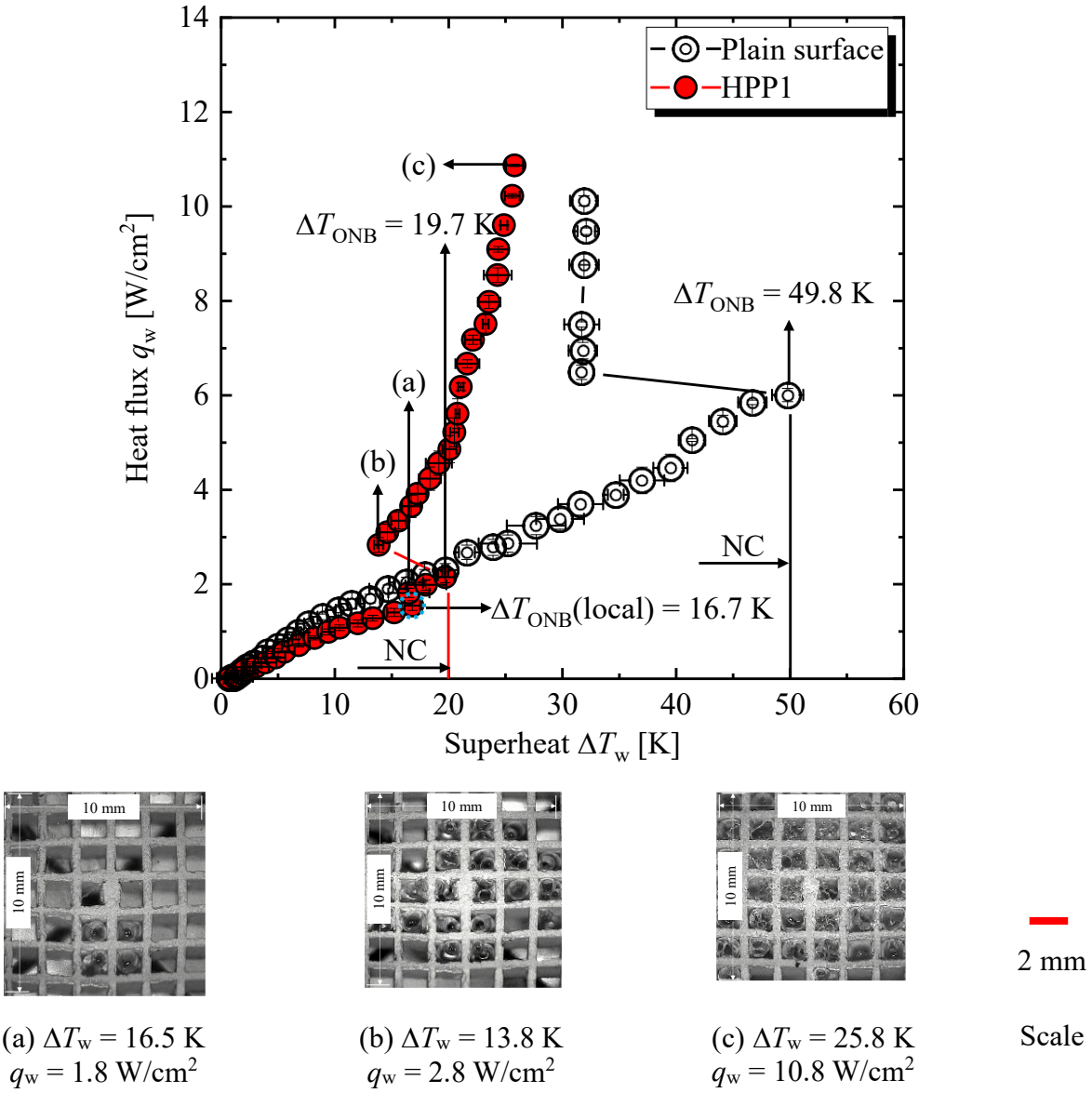

(a) ΔT_w = 16.5 K, q_w = 1.8 W/cm^2

(b) ΔT_w = 13.8 K, q_w = 2.8 W/cm^2

(c) ΔT_w = 25.8 K, q_w = 10.8 W/cm^2

Fig. 2.9 Effect of the HPP1 on ΔT_{ONB} in the case that experiments were performed immediately after degassing (0 h).

The HPP1 surface exhibited an approximately 1.5 times enhancement in the HTC compared to the plain surface in the nucleate boiling regime, as illustrated in Fig. 2.10. Later, detailed comparison between the plain surface and the HPP1 for the surface superheat distribution, heat transfer coefficient distribution and boiling configuration among the entire heating area (10 mm × 10 mm) was conducted. Refer to the nucleate boiling regime of the plain surface, three heat flux conditions (6.3 W/cm^2, 8.7 W/cm^2 and 10.1 W/cm^2) were chosen for comparison. The results were depicted in Fig. 2.11, 2.12 and 2.13, respectively. They demonstrate that both plain surface and HPP1 exhibit peaking values for

their heat transfer coefficient near the center of their entire surfaces. The reason for this peaking behavior at the center is that the center of the heating ITO layer experiences higher surface superheat due to heat diffusion effects. This higher surface superheat at the center promotes bubble nucleation in that region. Then heat can be efficiently removed through the latent heat associated with the phase change process.

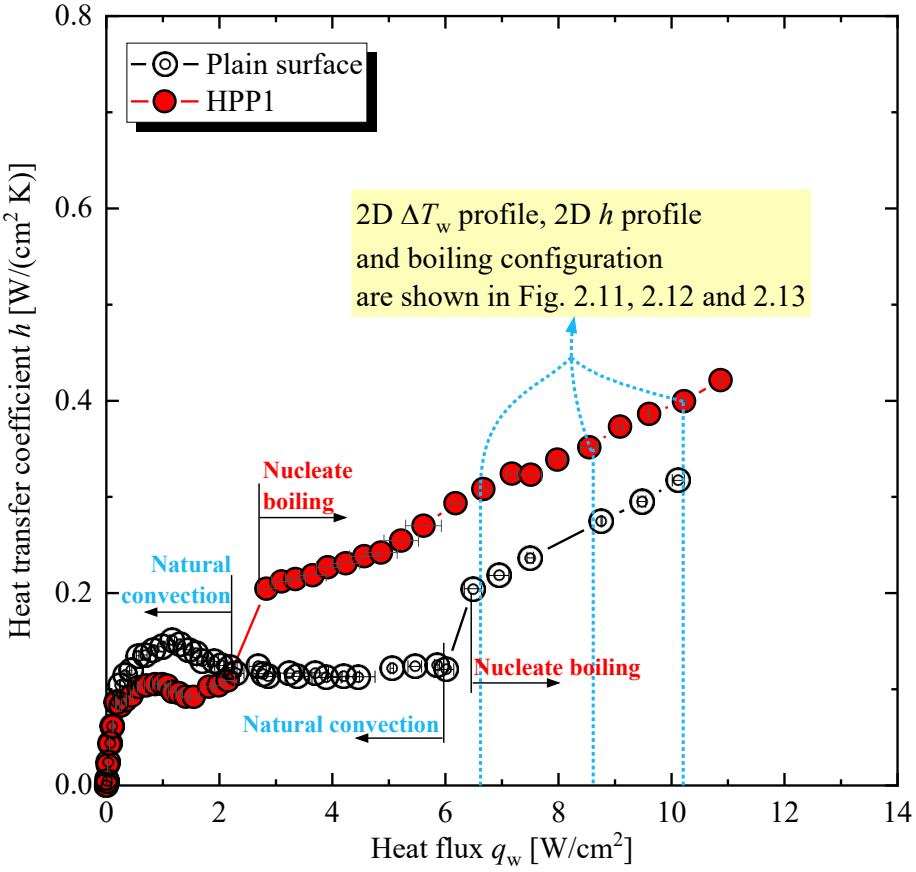

Fig. 2.10 Comparison of the HTC between the plain surface and HPP1 in the case that experiments were performed immediately after degassing (0 h).

However, the HPP1 surface shows a more varied and higher HTC distribution compared to the plain surface, suggesting that porous materials enhance local heat transfer rates more effectively. For example, at the heat flux condition of 6.3 W/cm^2, HTC value ranged from 1×10^4 to 2×10^4 W/(m^2 K) on the plain surface, indicating relatively uniform but moderate heat transfer. On the HPP1, HTC value ranged from 1×10^4 to over 3×10^4 W/(m^2 K), showing higher peak values and more significant spatial variation, which corresponds to localized intense boiling. With increase of the heat flux from 6.3 to 10.1 W/cm^2, the HPP1 consistently shows enhanced boiling performance compared to the plain surface, evidenced by the lower superheat and higher HTC values among the entire surface.

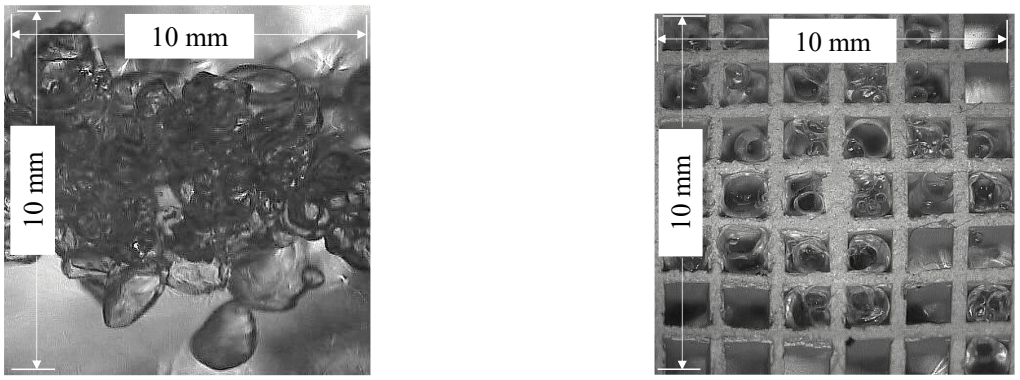

Plain surface HPP1

(a)

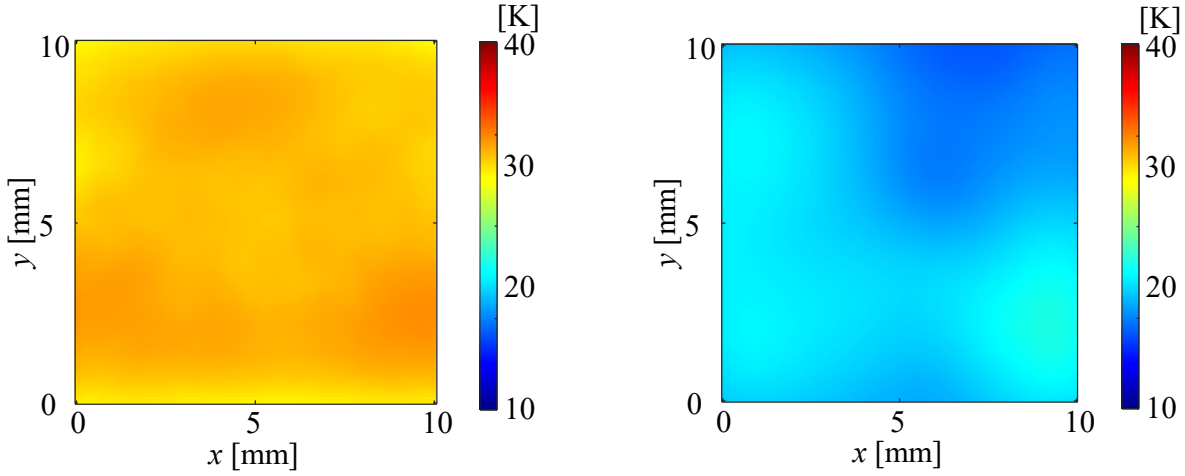

Plain surface HPP1

(b)

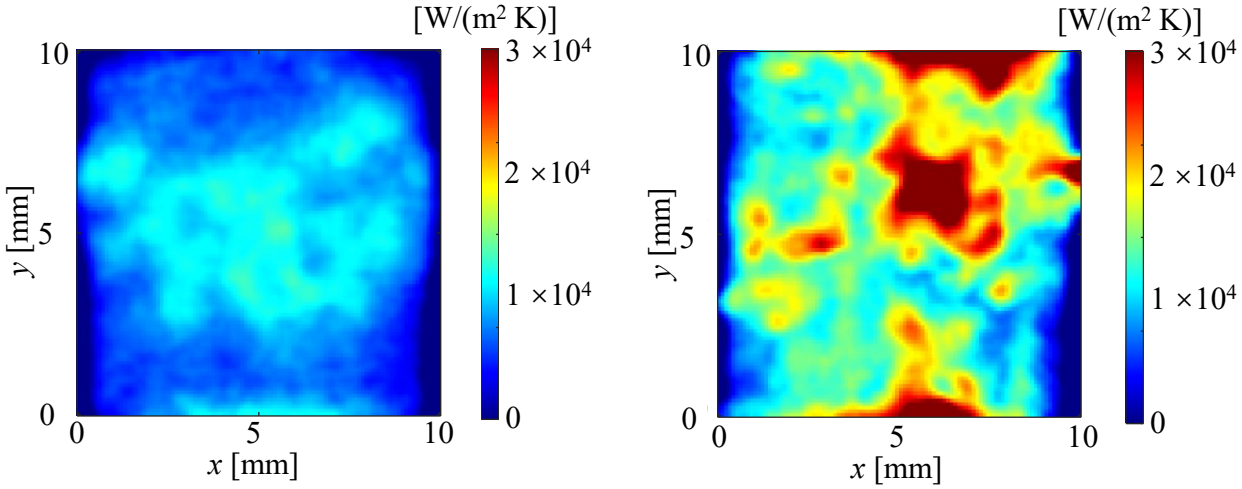

Plain surface HPP1

(c)

Fig. 2.11 Comparison between the plain surface and HPP1 under same heat flux of 6.3 W/cm^2 (a) boiling configuration, (b) surface superheat distribution and (c) heat transfer coefficient.

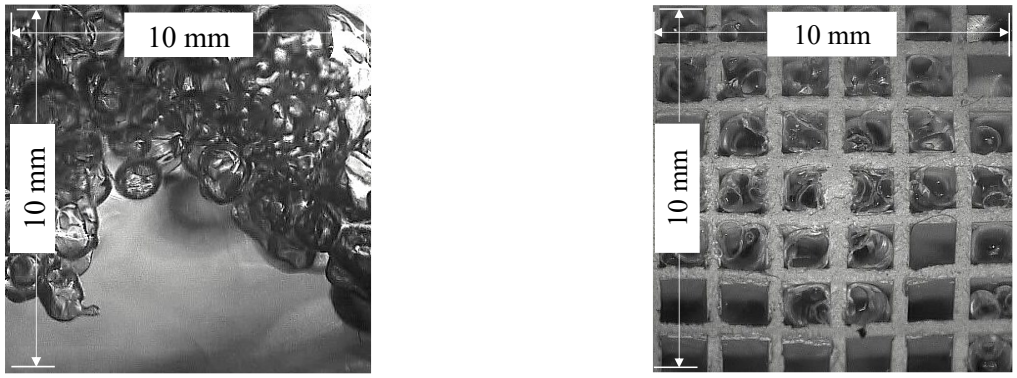

Plain surface HPP1

(a)

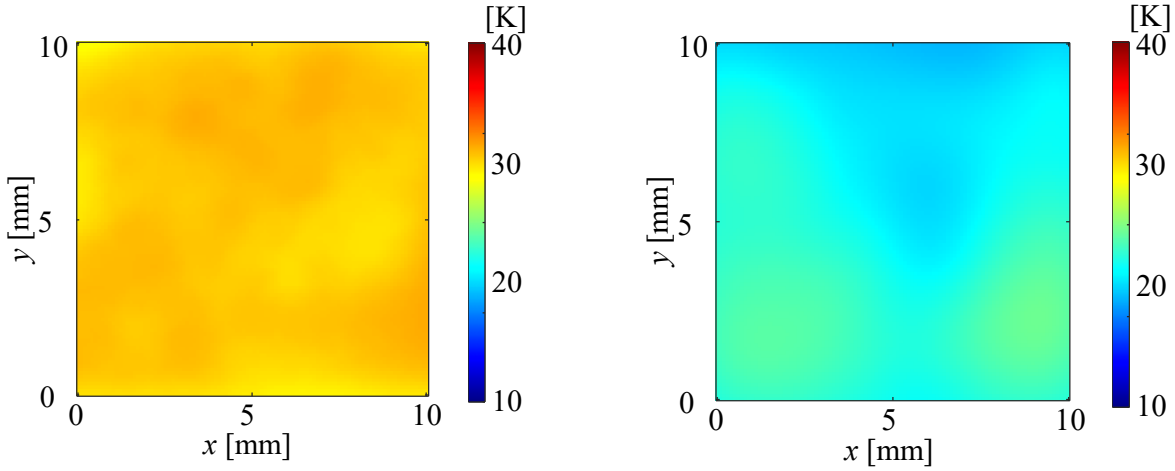

Plain surface HPP1

(b)

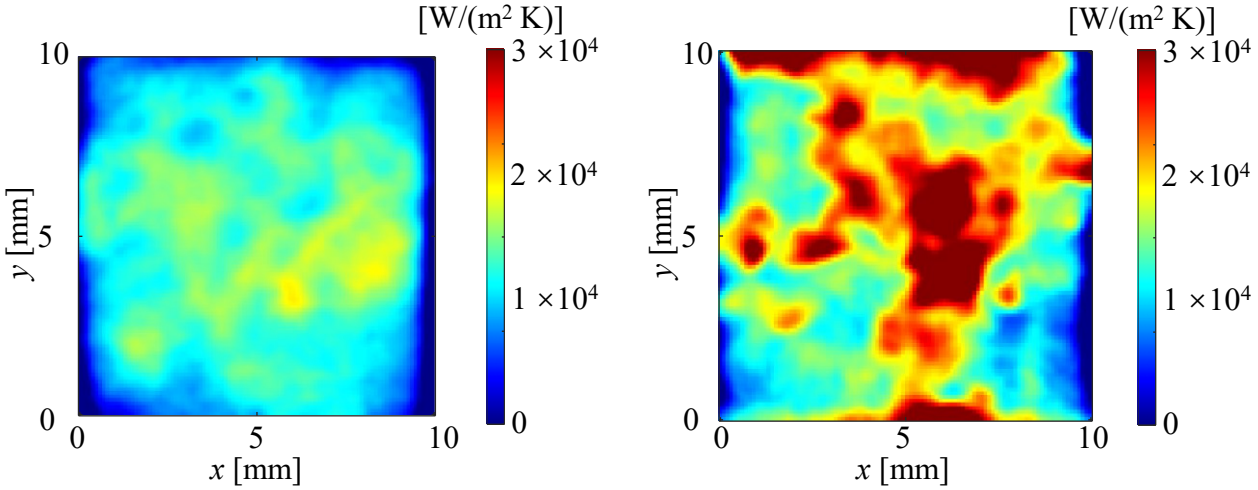

Plain surface HPP1

(c)

Fig. 2.12 Comparison between the plain surface and HPP1 under same heat flux of 8.7 W/cm^2 (a) boiling configuration, (b) surface superheat distribution and (c) heat transfer coefficient.

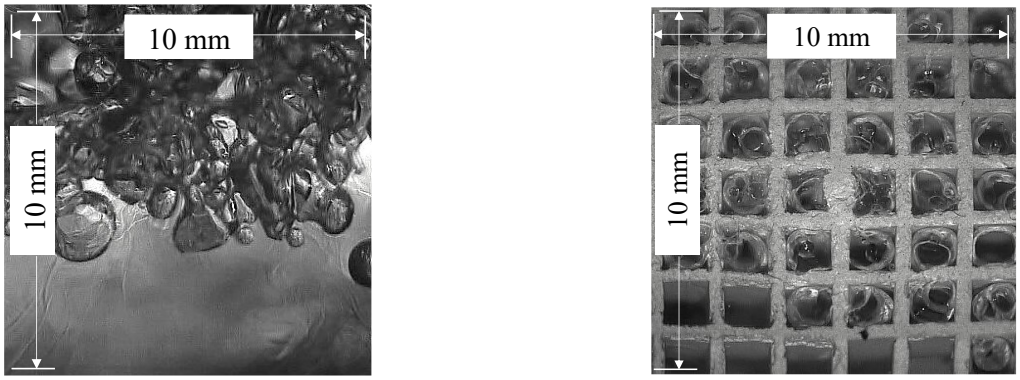

Plain surface HPP1

(a)

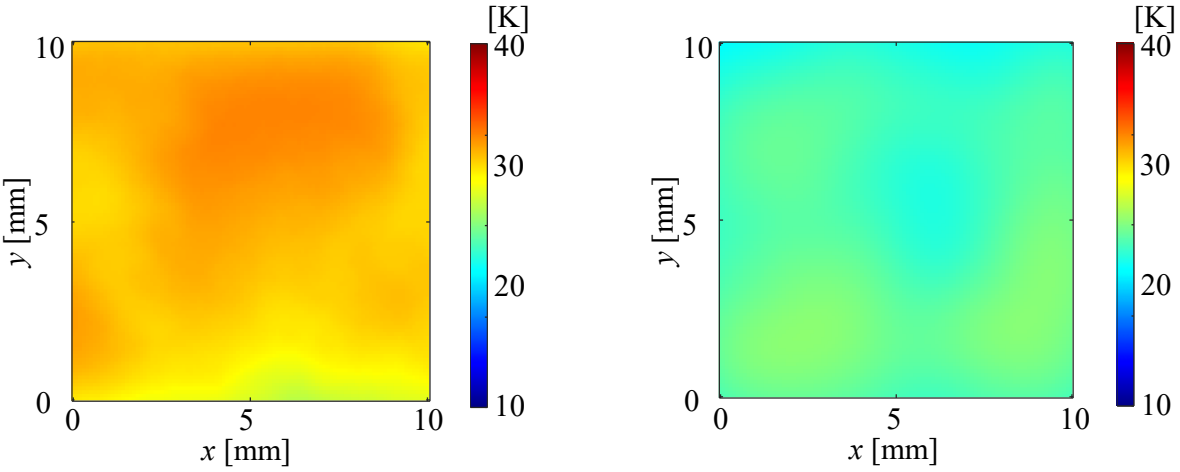

Plain surface HPP1

(b)

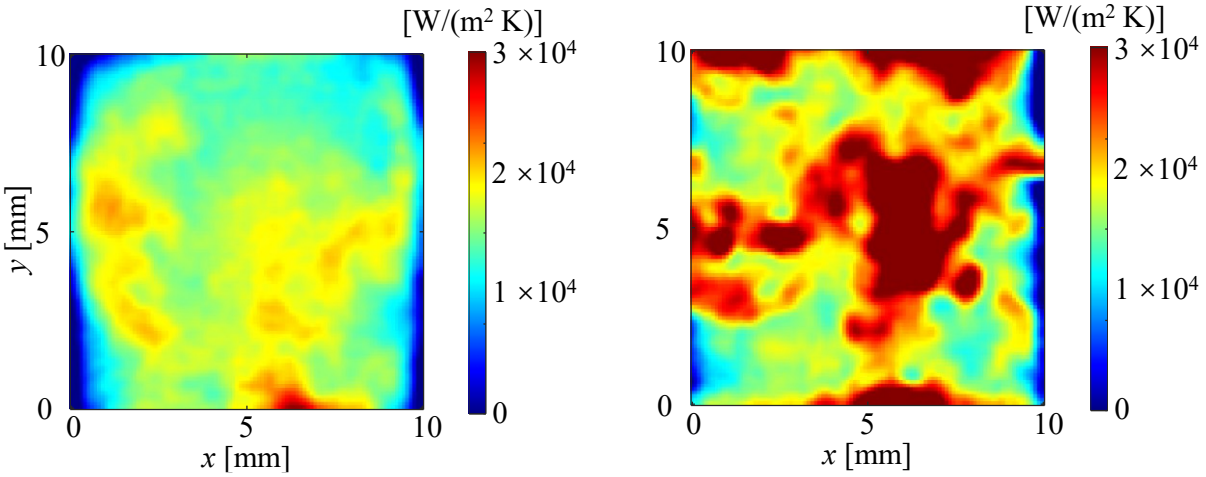

Plain surface HPP1

(c)

Fig. 2.13 Comparison between the plain surface and HPP1 under same heat flux of 10.1 W/cm^2 (a) boiling configuration, (b) surface superheat distribution and (c) heat transfer coefficient.

Figure 2.14 presents the surface superheat change over time for the plain surface and the HPP1 under three different heat flux conditions corresponding to those shown in Fig. 2.11, 2.12 and 2.13. From the lower heat flux of 6.3 W/cm^2 to the higher heat flux of 10.1 W/cm^2, the surface superheat variation for the plain surface was about 1.0 K. In contrast, the HPP1 surface generally exhibits stable surface superheat with a variation smaller than 0.2 K. The stable and low surface superheat variation observed for the HPP1 surface is advantageous from a material perspective. Minimizing temperature fluctuations can help mitigate thermal stresses and potential material degradation, leading to improved reliability and durability in applications involving boiling heat transfer.

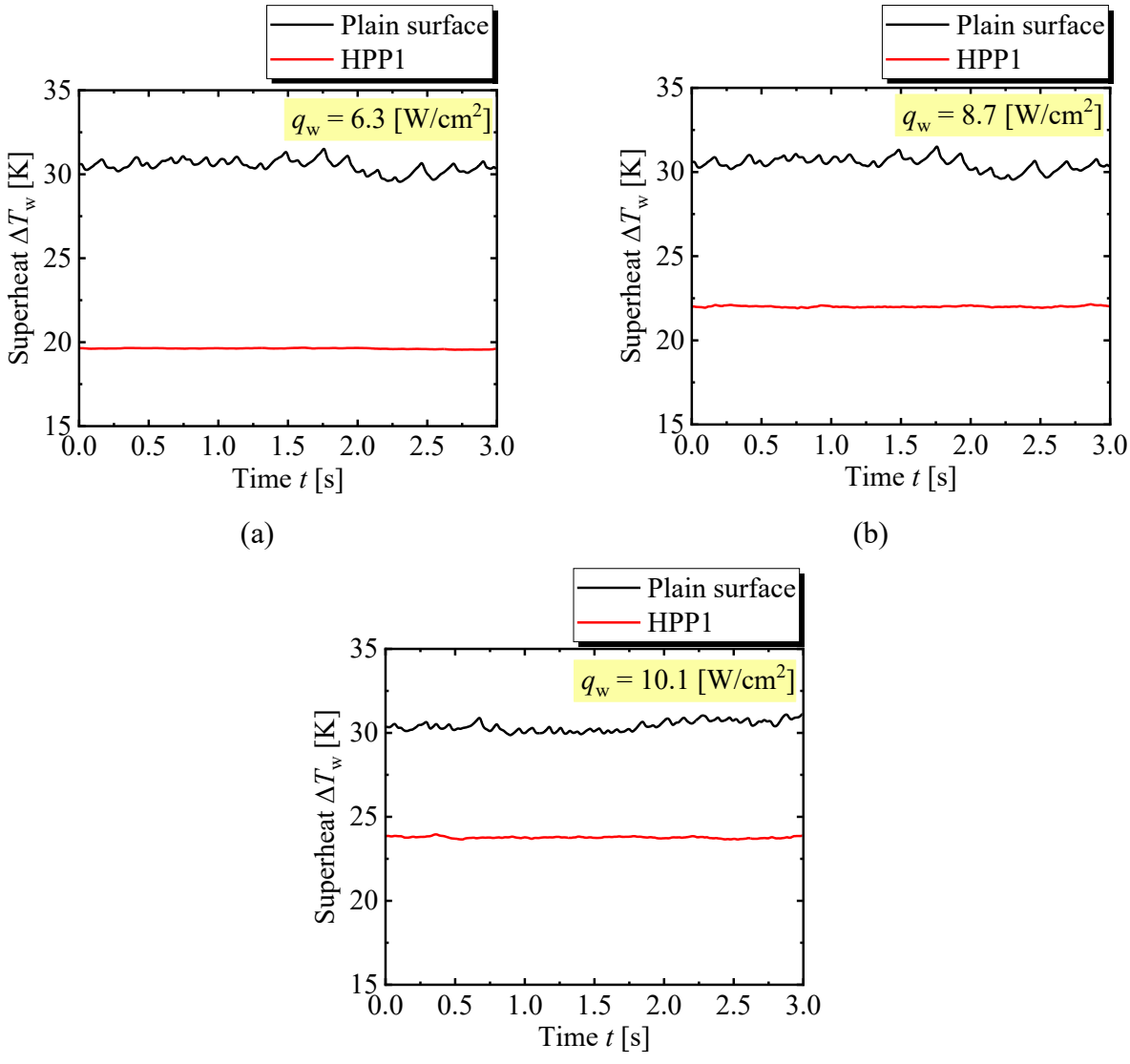

Fig. 2.14 Comparison between the plain surface and HPP1 of the surface superheat ΔT_w change over time under three different heat flux conditions of (a) 6.3 W/cm^2, (b) 8.7 W/cm^2 and (c) 10.1 W/cm^2.

2.3.3 Boiling performance on the HPP2 and HPP3

Similar to HPP1, the onset of nucleate boiling superheat ΔT_{ONB} was also decreased on the other porous plates, HPP2 and HPP3, as shown in Fig 2.15. The ΔT_{ONB} on the HPP2 was reduced at 11.8 K and there was no local ΔT_{ONB} observed in experiments. Most significantly, boiling on HPP3 was promoted with the elimination of temperature excursions typically observed during the process of boiling.

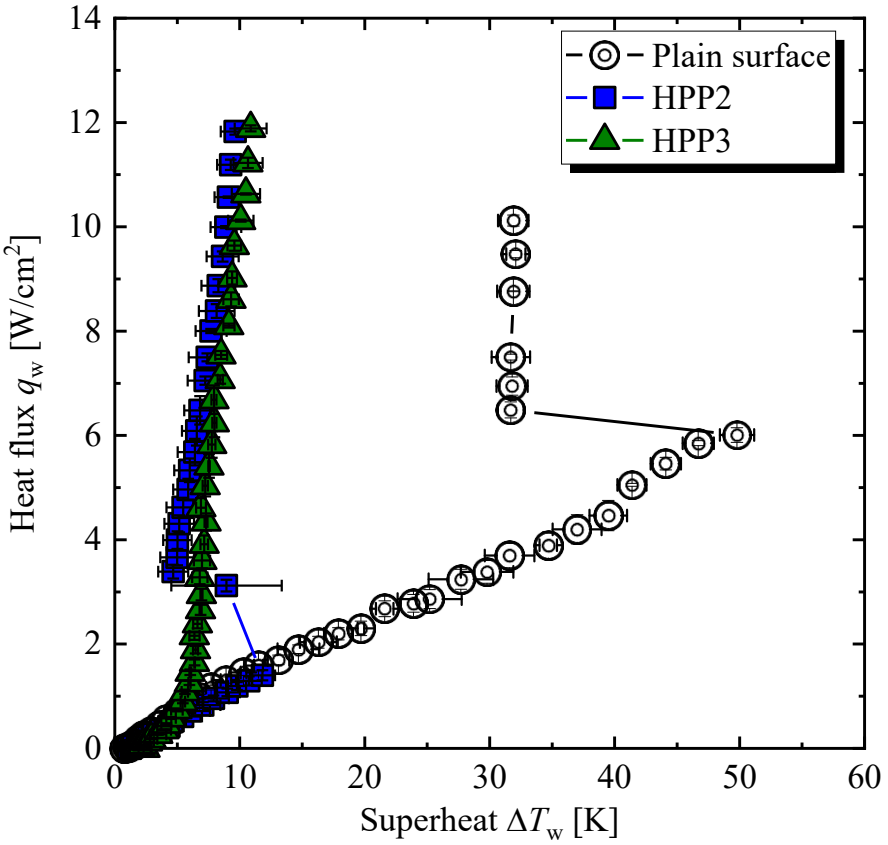

Fig. 2.15 Effect of the HPP2 and HPP3 on the ΔT_{ONB} in the case that experiments performed immediately after degassing (0 h).

When transitioning into the nucleate boiling regimes, the boiling curves for the porous plates (HPP2 and HPP3) exhibited a left-hand-side shift compared to the plain surface, suggesting enhanced heat transfer performance. The heat transfer coefficient (HTC) was increased by approximately 3.5 times for both HPP2 and HPP3. Note that slightly difference in the HTC was observed between HPP2 and HPP3, as depicted in Fig. 2.16, which was related to the boiling behavior on these porous plates.

To clarify the influence of boiling behavior, the boiling configurations and surface superheat distributions on HPP2 and HPP3 under different heat flux conditions are compared in Figs. 2.17 and 2.18, respectively. At lower heat fluxes, such as 1.5 W/cm^2 (Fig. 2.17 (a) and Fig. 2.18 (a)), local boiling was found on the HPP3, allowing efficient heat removal by local evaporation. As a result, a lower surface superheat was observed on HPP3, leading to a higher HTC compared to HPP2. However, as the heat flux increase to 3.4 W/cm^2 (Fig. 2.17 (b) and Fig. 2.18 (b)), boiling occurred across the entire HPP2 surface, while boiling did not occur in the center region of HPP3. The extensive boiling coverage on HPP2 resulted in a higher HTC compared to HPP3 at this heat flux condition. As the heat flux further increased to 4.3 W/cm^2 (Fig. 2.17 (c) and Fig. 2.18 (c)), total boiling occurred across the entire HPP3 surface as well. Consequently, the difference in HTC between these two porous plates diminished at this higher heat flux condition due to similar boiling coverage.

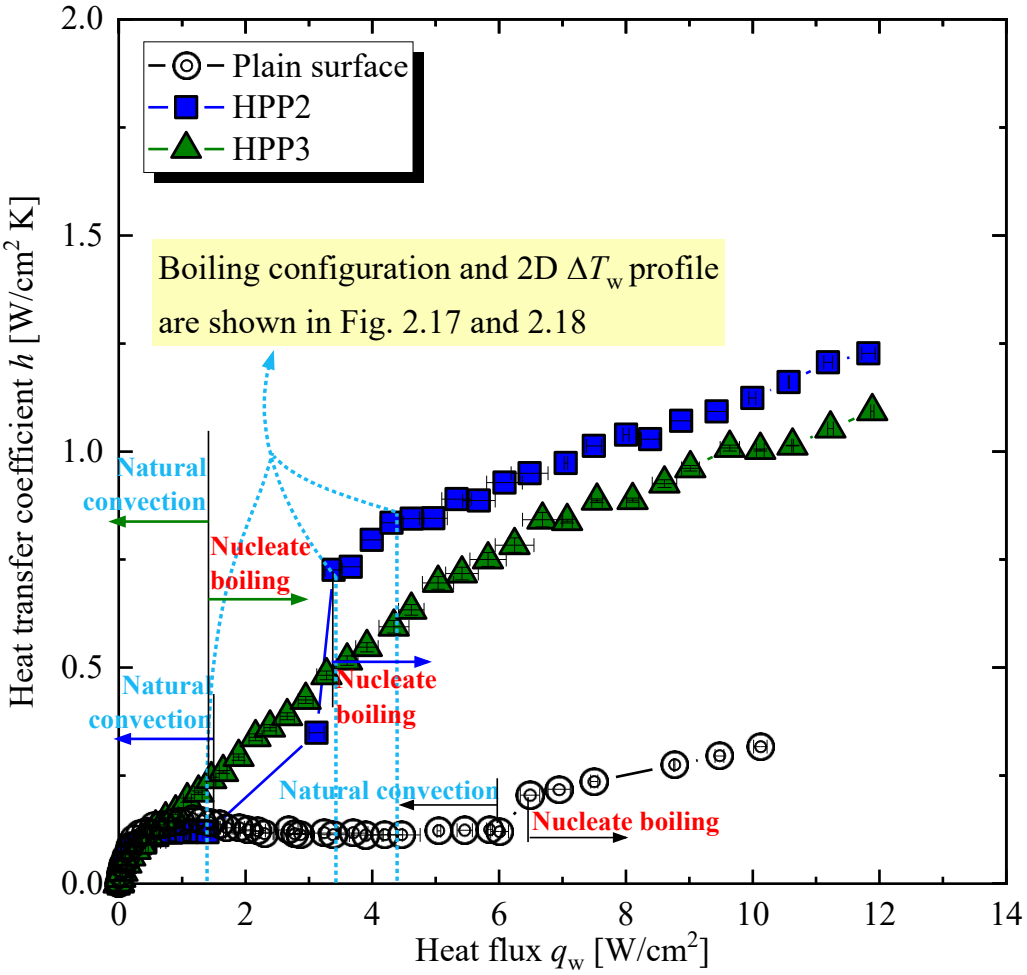

Fig. 2.16 HTC of the HPP2 and HPP3 in the case that experiments performed immediately after degassing (0 h).

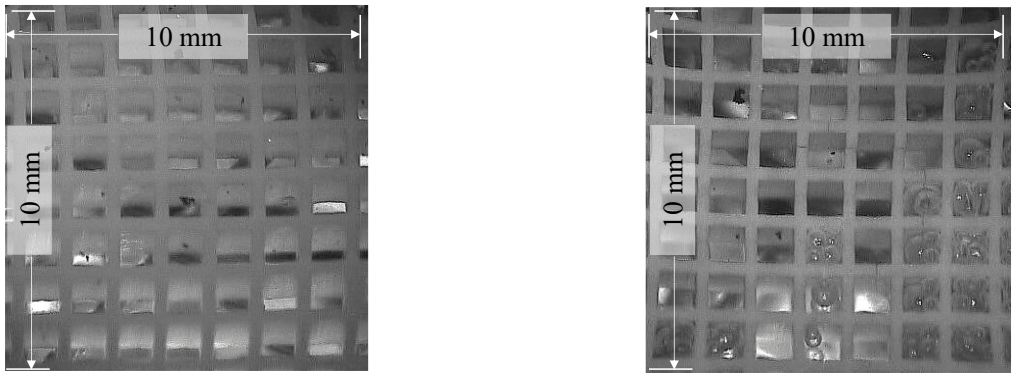

HPP2 HPP3

(a)

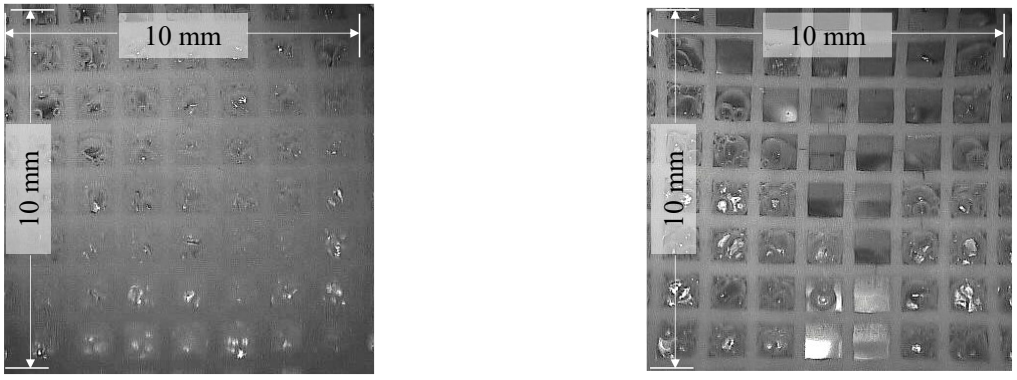

HPP2 HPP3

(b)

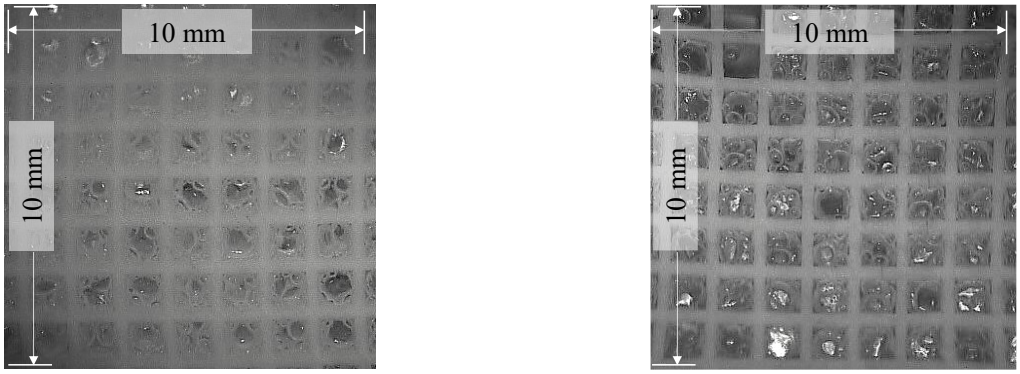

HPP2 HPP3

(c)

Fig. 2.17 Boiling configuration comparison between the HPP2 and HPP3 under same heat flux of (a) 1.5 W/cm^2, (b) 3.4 W/cm^2 and (c) 4.3 W/cm^2.

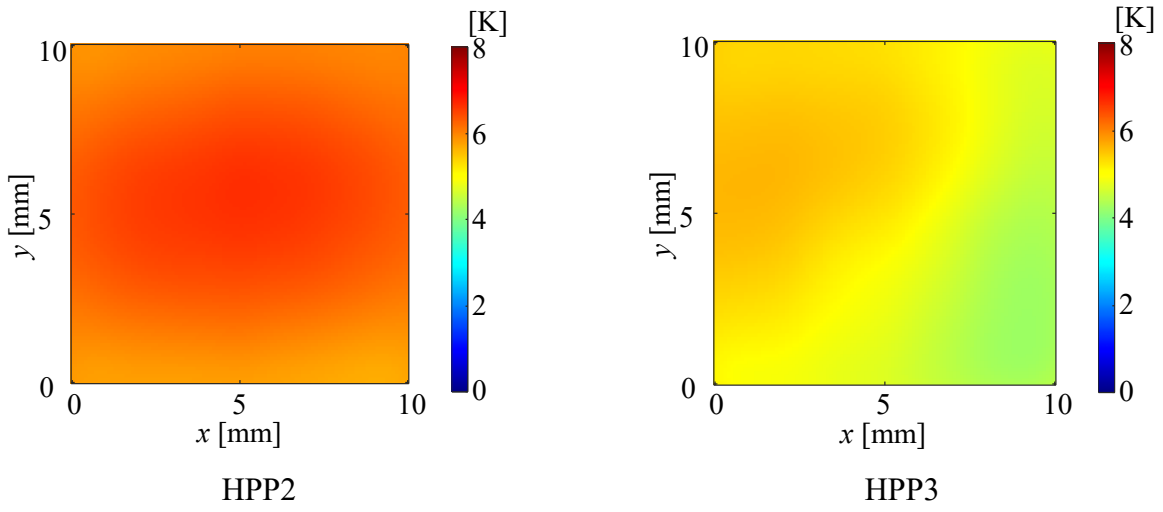

(a)

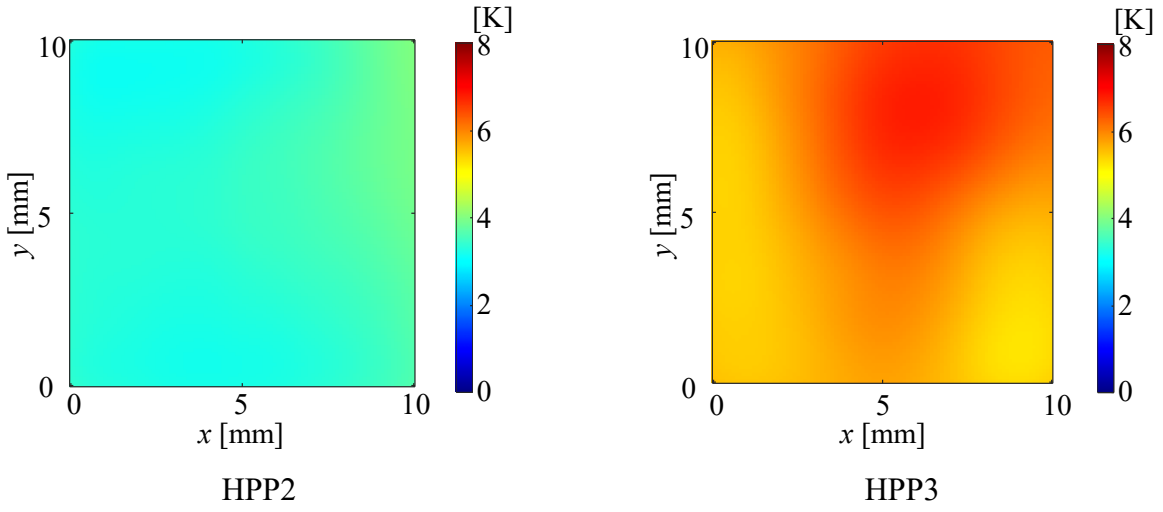

(b)

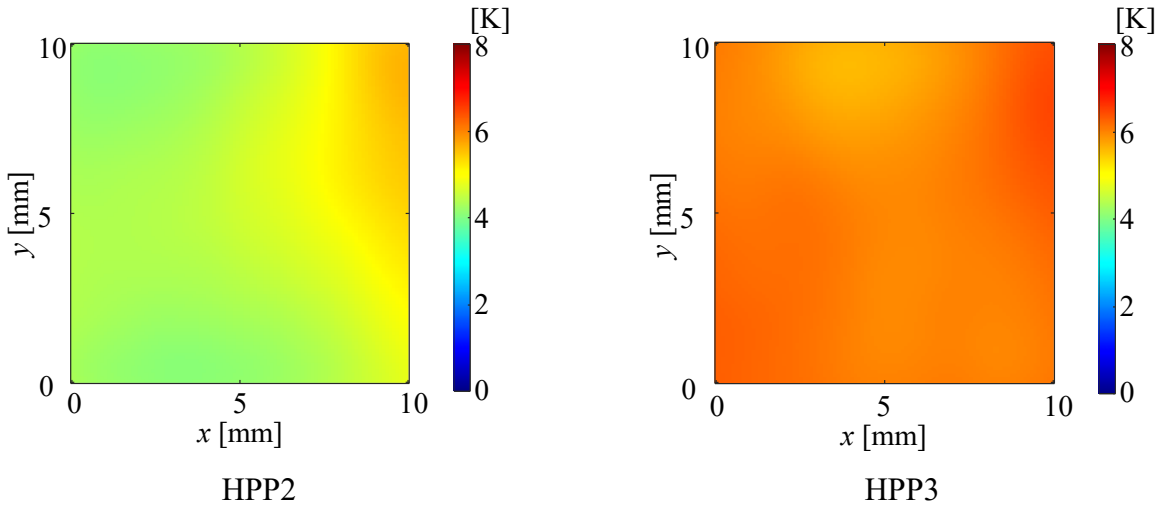

(c)

Fig. 2.18 Surface superheat distribution comparison between the HPP2 and HPP3 under same heat flux of (a) 1.5 W/cm^2, (b) 3.4 W/cm^2 and (c) 4.3 W/cm^2.

2.3.4 Boiling performance on the HPPs after 48-h immersion

Although surface superheat for triggering boiling ΔT_{ONB} significantly decreased on these porous plates, cavities in the porous structure were likely flooded by the fluid during immersion and may degrade the performance of these HPPs. In consideration of this effect, boiling experiments were performed on these HPPs after each HPP was left in the vessel immersed with AE-3000 liquid for 48 hours. The boiling curves are summarized in Fig. 2.19.

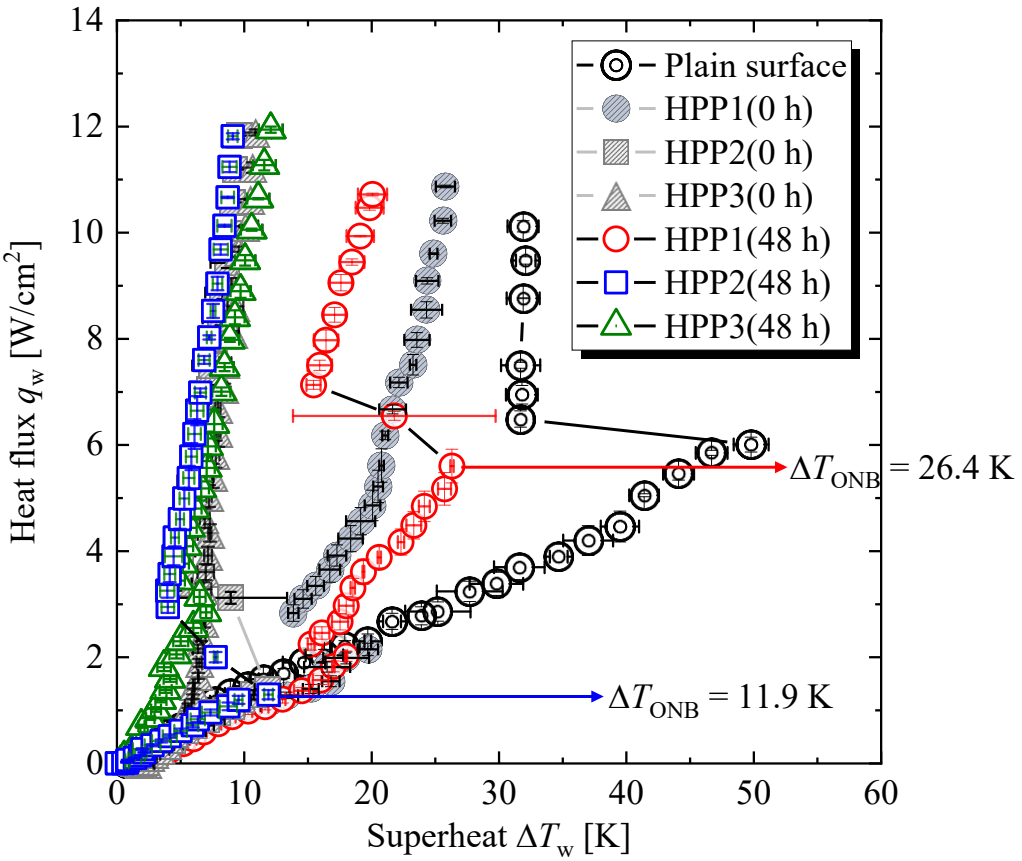

Fig. 2.19 Effect of the HPPs on ΔT_{ONB} in the case that experiments were after 48-h immersion.

After 48-h immersion, degradation of the ΔT_{ONB} on the HPP1 was found, for clear comparison, boiling curves of the HPPs during the initial run (0 h) was added in Fig. 2.19, as shown by the gray stripe symbols. An increase of 6.7 K of the averaged ΔT_{ONB} for the HPP1 was found after 48-h immersion, with the averaged ΔT_{ONB} increase from 19.7 K to 26.4 K. In contrast, the HPP2 and HPP3 surfaces maintained their reliable boiling performance. For the HPP2, the ΔT_{ONB} was 11.9 K after 48-h immersion, indicating no significant degradation compared to the initial run (ΔT_{ONB} = 11.8 K). For

the HPP3, nearly smooth boiling curves was also attained, with just a small surface superheat drop of less than 1.0 K observed at a surface superheat of 8.0 K.

Figure 2.19 showed the averaged surface superheat for incipience boiling (ΔT_{ONB}), detailed information of the local ΔT_{ONB} and average ΔT_{ONB} was checked next. For example, on the HPP1, local boiling phenomenon was first found at the surface superheat of 16.7 K initially (0 h) and 18.0 K after immersion (48 h). The corresponding boiling configuration and two-dimensional surface superheat profiles were also shown in Fig 2.20 (a), (b) and 2.21 (a), (b), respectively. It can be seen that earlier local boiling occurred initially (Fig 2.20 (a), (b)) and the local boiling was triggered under a lower ΔT_w of 16.7 K with q_w of 1.5 W/cm^2. In contrast, delayed local boiling was triggered when the experiments were restarted after immersion (Fig 2.21 (a), (b)), under a higher ΔT_w of 18.0 K with q_w of 2.0 W/cm^2. Figure 2.21 (b) also showed more bubbles were generated, and a corresponding lower surface superheat was observed. This suggests that more cavities were active when boiling was triggered during the restarting experiments.

Boiling configuration and two-dimensional surface superheat profiles for the average ΔT_{ONB} condition of the HPP1 were also shown in Fig 2.22 (a), (b) and 2.23 (a), (b). Initially, most cavities were activated under a lower ΔT_{ONB} of 19.7 K with q_w of 2.1 W/cm^2. It was found that the q_w for activating most cavities in the initial run was close to the q_w condition for activating partial cavities in the restarting run. Therefore, the local boiling after immersion was the failure reproduction for activating most nucleation cavities as the initial run. Most cavities were active until higher surface superheat was reached, with the average ΔT_{ONB} of 26.4 K in boiling curves (Fig 2.23). Accurate local surface superheat for triggering the remained non-active cavities after local boiling could be confirmed by the surface superheat distribution. A local hotspot which over ranged the operation temperature (85℃) was found at the ONB condition during the restarting experiment. For clear confirmation, ΔT_w histograms of the IR thermograph was added in Fig 2.23 (c). The vertical axis represents the ratio between the corresponding counts of specific superheat to the total measured counts (one measured point represents the area of 50 μm × 50 μm). The highest surface superheat required for active cavities was about 33.0 K (88℃) after immersion. In the same way, the highest surface superheat required for active cavities was about 21.0 K (76℃) initially.

It is noted that better HTC in the nucleate boiling regime was attained after immersion compared with the initial run. The higher surface superheat was advanced for activating more nucleation cavities which contributed to a better HTC.

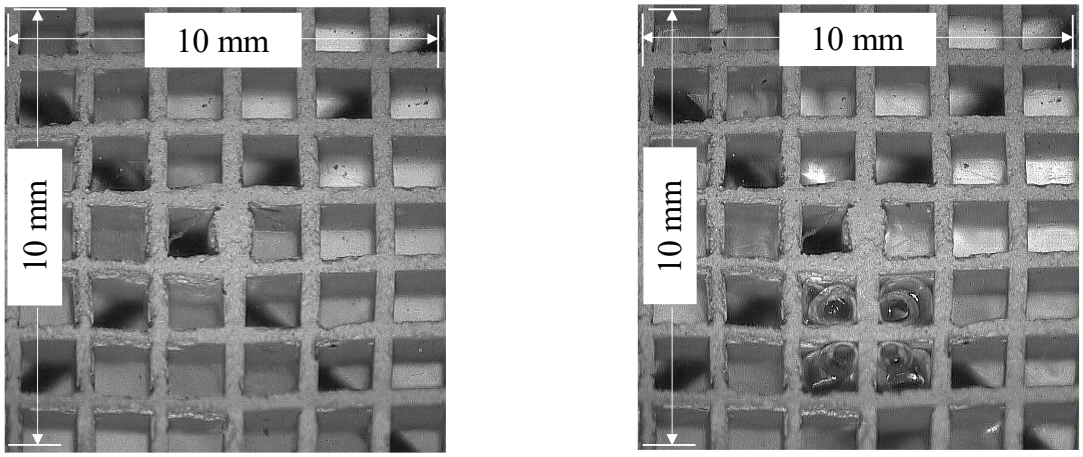

ΔT_w = 16.7 K, q_w = 1.5 W/cm^2 (Local ΔT_{ONB})

ΔT_w = 16.5 K, q_w = 1.8 W/cm^2

(a)

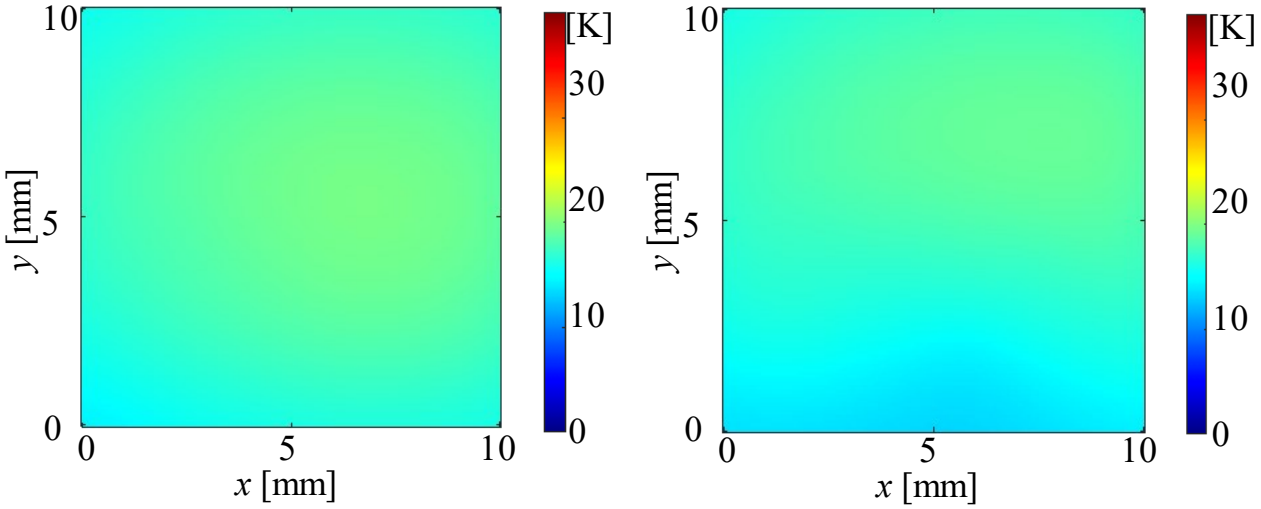

ΔT_w = 16.7 K, q_w = 1.5 W/cm^2

ΔT_w = 16.5 K, q_w = 1.8 W/cm^2

(b)

Fig. 2.20 (a) Boiling configuration and (b) 2D surface superheat ΔT_w distribution during the local boiling process of the HPP1 for the initial run (0 h).

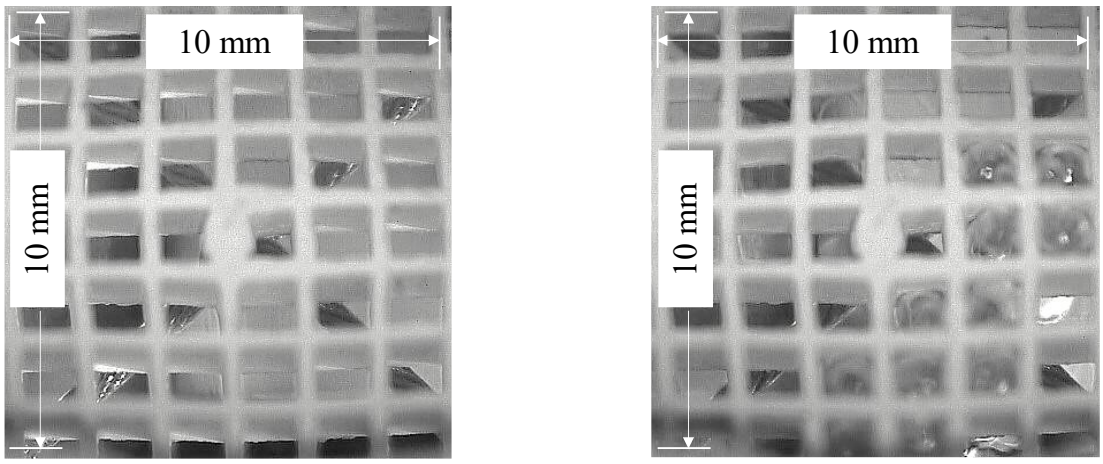

ΔT_w = 18.0 K, q_w = 2.0 W/cm^2

(Local ΔT_{ONB})

ΔT_w = 15.3 K, q_w = 2.2 W/cm^2

(a)

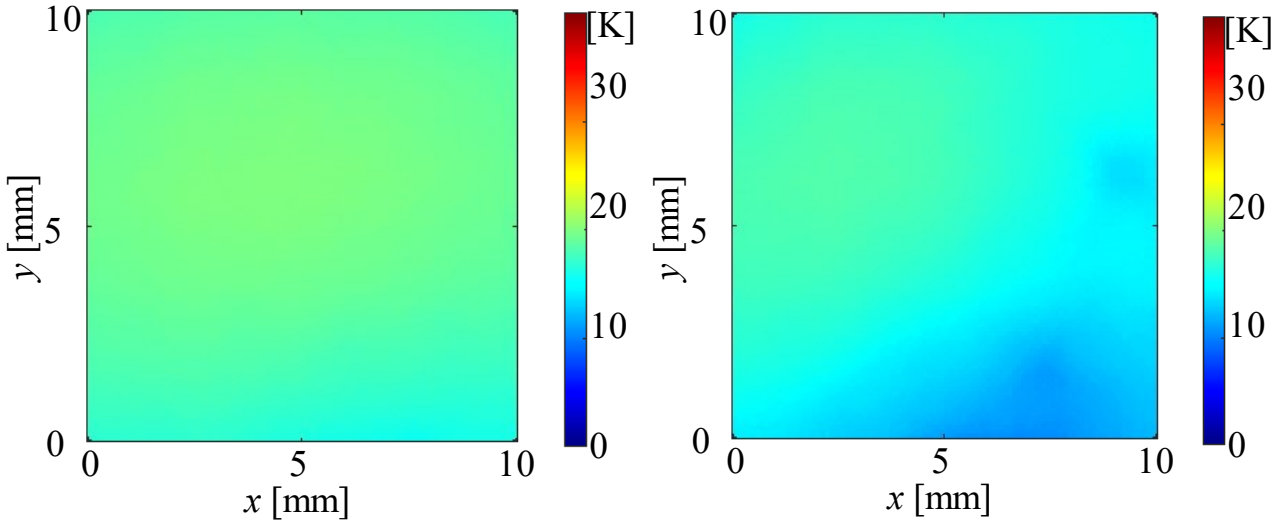

ΔT_w = 18.0 K, q_w = 2.0 W/cm^2

ΔT_w = 15.3 K, q_w = 2.2 W/cm^2

(b)

Fig. 2.21 (a) Boiling configuration and (b) 2D surface superheat ΔT_w distribution during the first local boiling process of the HPP1 for the immersion run (48 h).

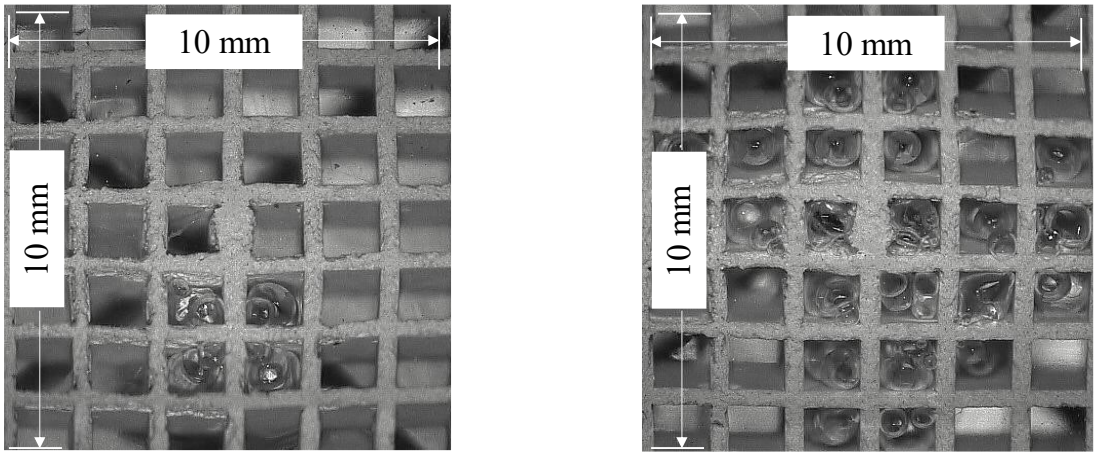

ΔT_w = 19.7 K, q_w = 2.1 W/cm^2

(Average ΔT_{ONB})

ΔT_w = 13.8 K, q_w = 2.8 W/cm^2

(a)

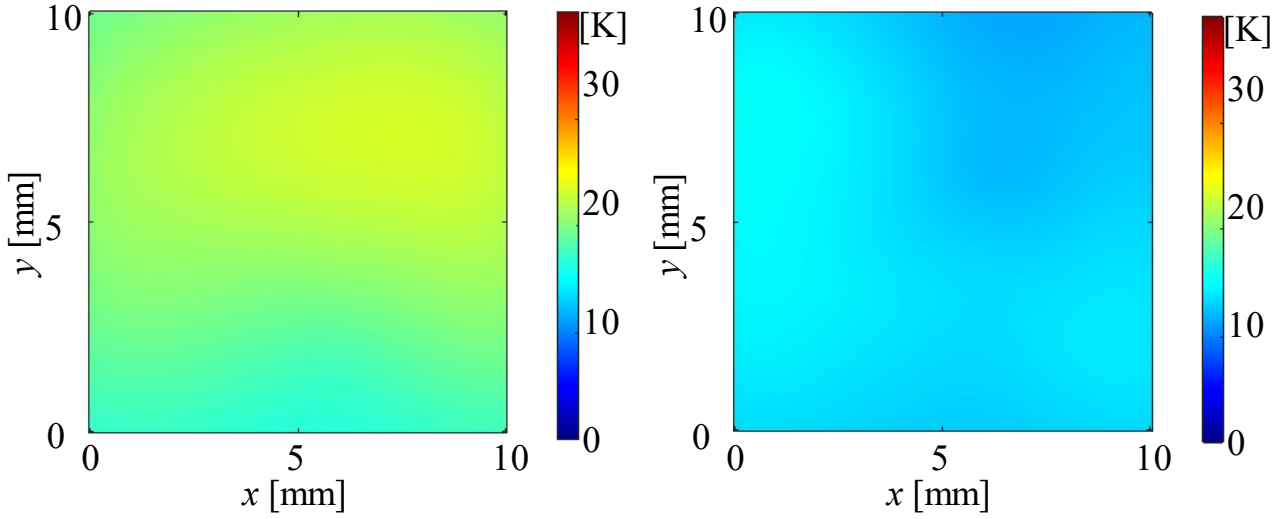

ΔT_w = 19.7 K, q_w = 2.1 W/cm^2

ΔT_w = 13.8 K, q_w = 2.8 W/cm^2

(b)

Fig. 2.22 (a) Boiling configuration and (b) 2D surface superheat ΔT_w distribution for the total boiling (average ΔT_{ONB}) of the HPP1 for the initial run (0 h).

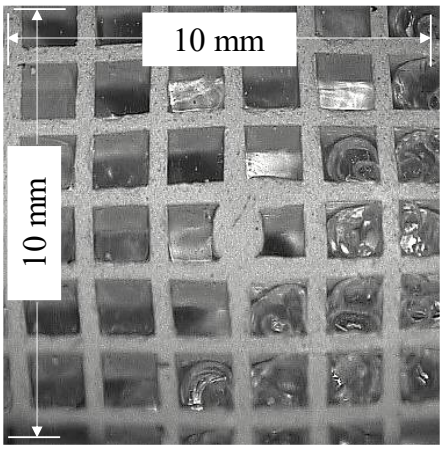

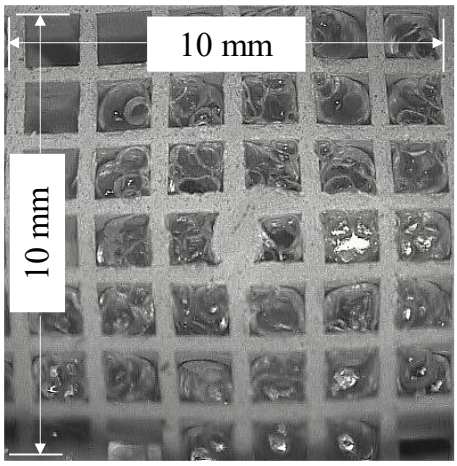

ΔT_w = 26.4 K, q_w = 5.6 W/cm^2

(Average ΔT_{ONB})

ΔT_w = 15.4 K, q_w = 7.1 W/cm^2

(a)

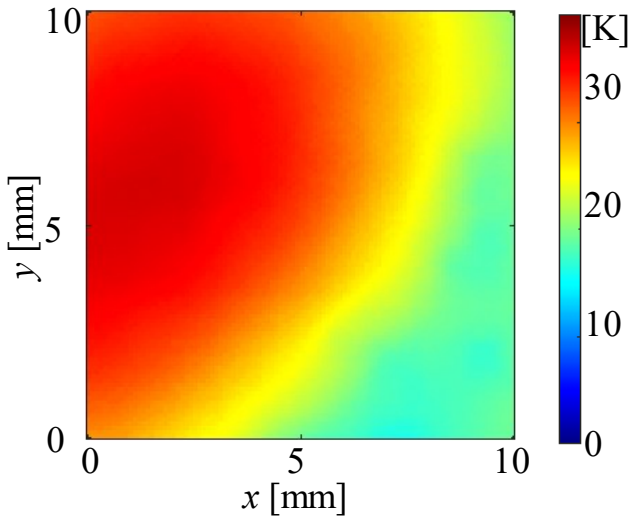

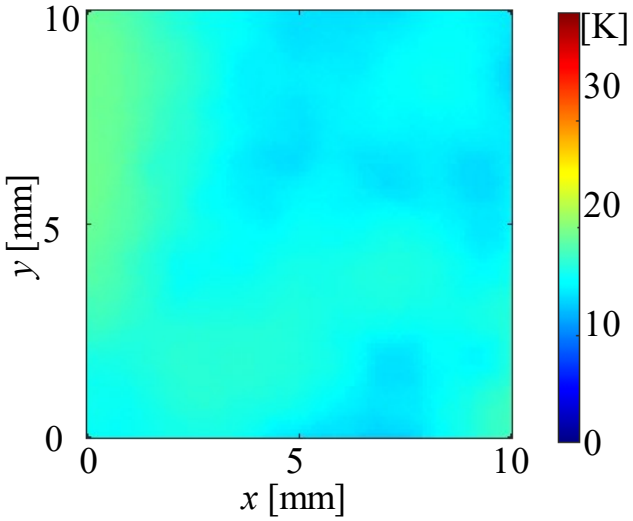

ΔT_w = 26.4 K, q_w = 5.6 W/cm^2

ΔT_w = 15.4 K, q_w = 7.1 W/cm^2

(b)

Fig. 2.23 (a) Boiling configuration, (b) 2D surface superheat ΔT_w distribution and (c) ΔT_w distribution for the total boiling (average ΔT_{ONB}) of the HPP1 for the immersion run (48 h).

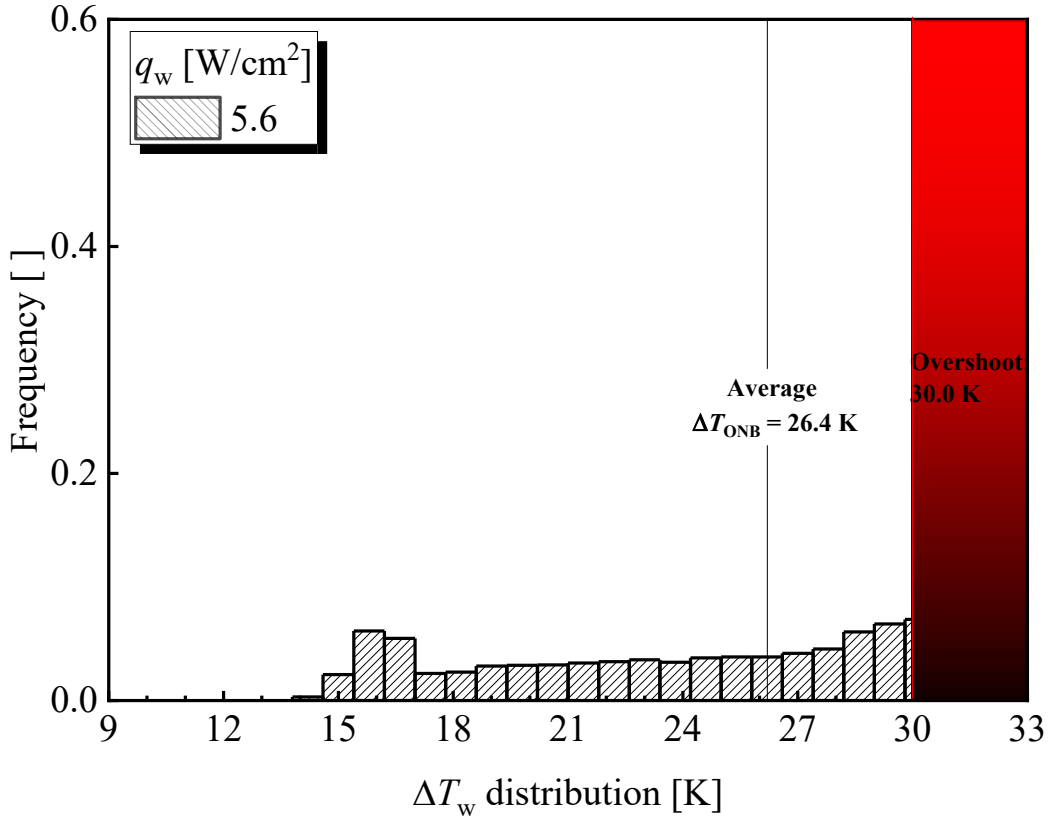

(c)

Fig. 2.23 (Continued).

Local boiling was not observed on the HPP2 for both initial and immersion run, the average surface superheat of the boiling curves was considered representative for incipience boiling. The detailed surface superheat distribution was not discussed here. The absence of the local boiling was considered to be caused by the pore distribution difference in the HPP2, which will be compared after the ΔT_{ONB} of all the HPPs was analyzed.

Unlike the HPP1, HPP3 exhibited a gradual local boiling process with eliminated superheat changes of boiling curves. Specific two-dimensional surface superheat profiles were chosen for explanation, starting from when local boiling was first observed until boiling occurred across the entire surface. The results were shown in Fig. 2.24 and 2.25 for the initial run and Fig. 2.26 and 2.27 for the immersion run.

The results showed that the surface superheat for the first local boiling observation on the HPP3 was 2.6 K and 4.3 K during the initial run and immersion run, respectively. And when boiling occurred in the entire surface, the required maximum surface superheat was 7.4 K and 8.0 K during the initial run and immersion run, respectively. Good reproduction of the ΔT_{ONB} on the HPP3 was confirmed. And surface superheat for the boiling incipience including averaged ΔT_{ONB} and local ΔT_{ONB} for each

porous plate was summarized in Table 2.3. Local ΔT_{ONB} range was defined as the average surface superheat for the first local boiling observation and the maximum surface superheat for the final local boiling observation.

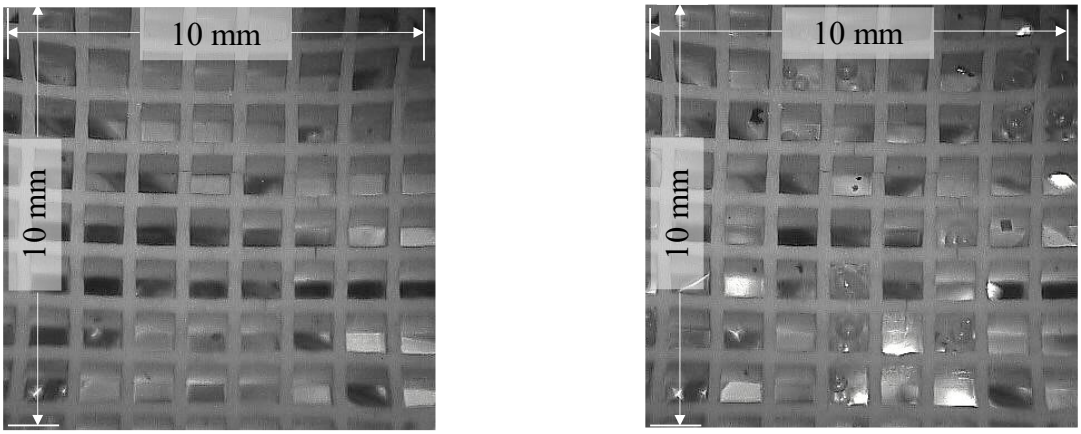

ΔT_w = 2.6 K, q_w = 0.9 W/cm^2 ΔT_w = 2.9 K, q_w = 1.1 W/cm^2

(a)

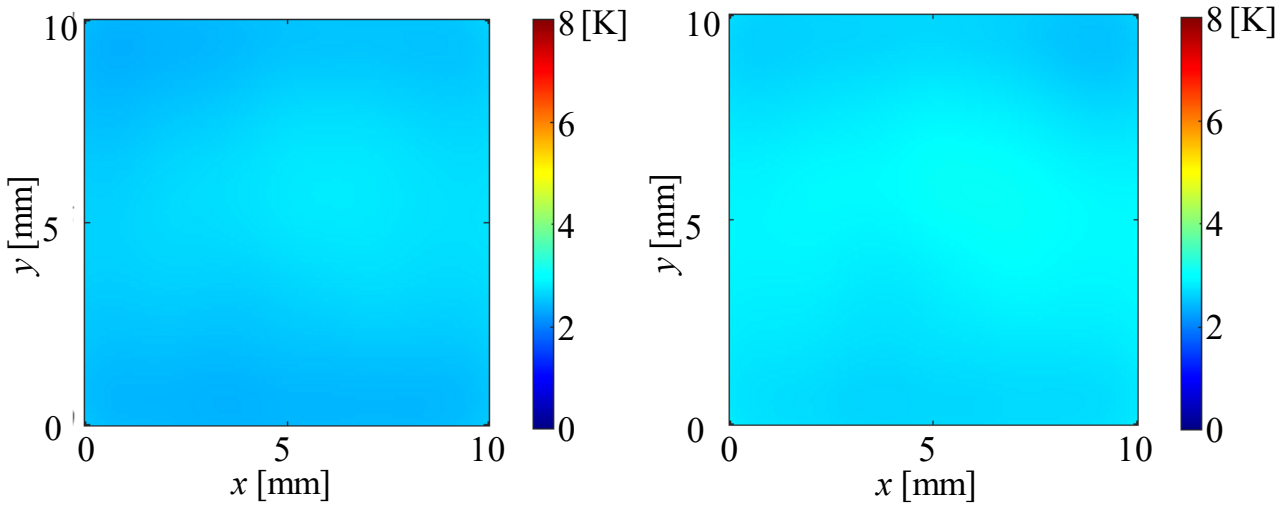

ΔT_w = 2.6 K, q_w = 0.9 W/cm^2 ΔT_w = 2.9 K, q_w = 1.1 W/cm^2

(b)

Fig. 2.24 (a) Boiling configuration and (b) 2D surface superheat ΔT_w distribution during the first local boiling process of the HPP3 for the initial run (0 h).

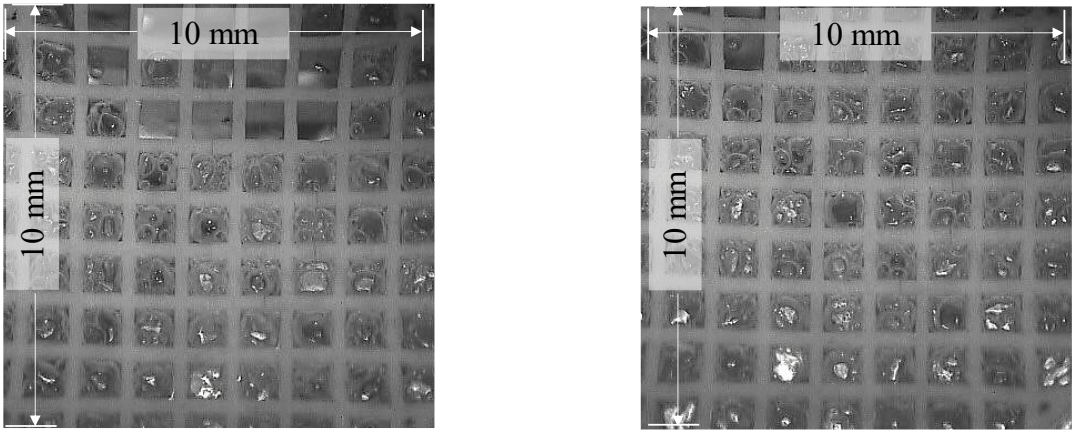

ΔT_w = 6.3 K, q_w = 2.3 W/cm^2 ΔT_w = 6.0 K, q_w = 2.6 W/cm^2

(a)

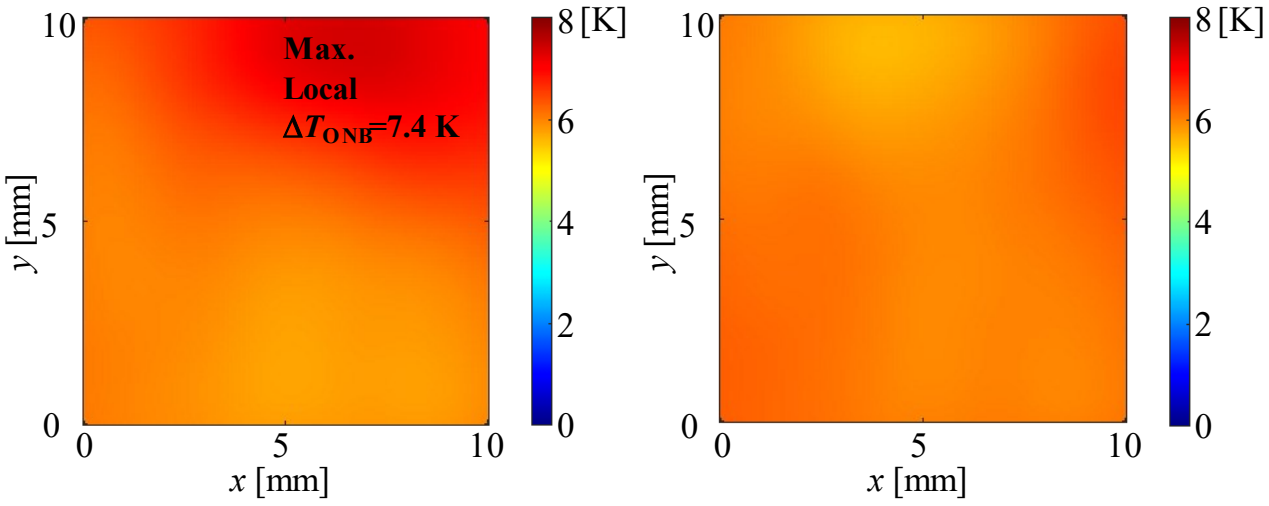

ΔT_w = 6.3 K, q_w = 2.3 W/cm^2 ΔT_w = 6.0 K, q_w = 2.6 W/cm^2

(b)

Fig. 2.25 (a) Boiling configuration and (b) 2D surface superheat ΔT_w distribution during the final local boiling process of the HPP3 for the initial run (0 h).

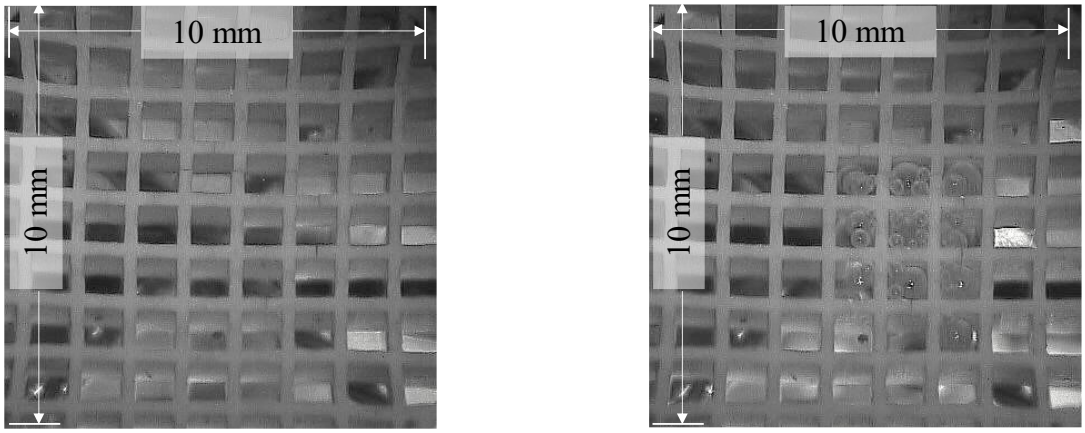

ΔT_w = 4.3 K, q_w = 1.6 W/cm^2 ΔT_w = 3.7 K, q_w = 1.8 W/cm^2

(a)

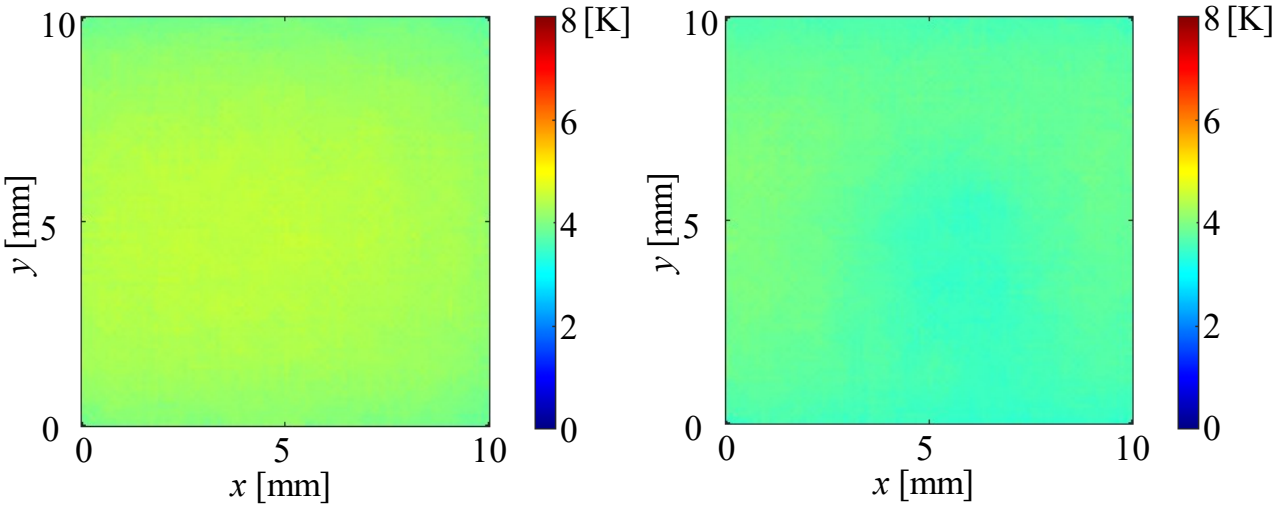

ΔT_w = 4.3 K, q_w = 1.6 W/cm^2 ΔT_w = 3.7 K, q_w = 1.8 W/cm^2

(b)

Fig. 2.26 (a) Boiling configuration and (b) 2D surface superheat ΔT_w distribution during the first local boiling process of the HPP3 for the immersion run (48 h).

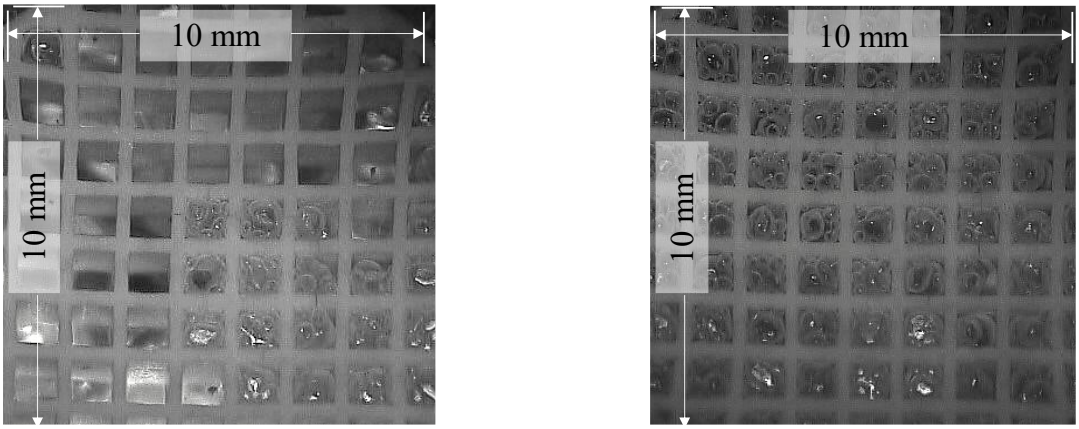

ΔT_w = 7.0 K, q_w = 2.8 W/cm^2 ΔT_w = 4.9 K, q_w = 3.3 W/cm^2

(a)

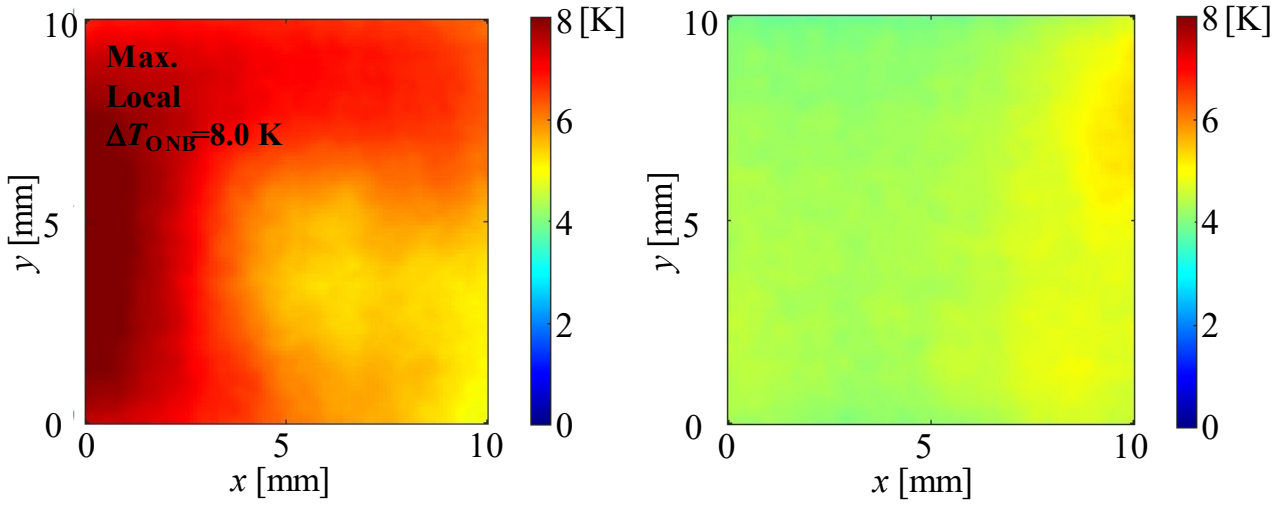

ΔT_w = 7.0 K, q_w = 2.8 W/cm^2 ΔT_w = 4.9 K, q_w = 3.3 W/cm^2

(b)

Fig. 2.27 (a) Boiling configuration and (b) 2D surface superheat ΔT_w distribution during the final local boiling process of the HPP3 for the immersion run (48 h).

Table 2.4 Surface superheat for the boiling incipience of the HPPs

Experiment condition	Immediately after degassing (0 h)	After immersion and degassing (48 h)
	HPP1	**HPP1**
	Average ΔT_{ONB}	Average ΔT_{ONB}
	19.7 K	26.4 K
	Local ΔT_{ONB} range	Local ΔT_{ONB} range
	15.2 K~21.0 K	18.0 K~33.0 K
	HPP2	**HPP2**
	Average ΔT_{ONB}	Average ΔT_{ONB}
	11.8 K	11.9 K
	Local ΔT_{ONB} range	Local ΔT_{ONB} range
	None	None
	HPP3	**HPP3**
	Average ΔT_{ONB}	Average ΔT_{ONB}
	Nearly eliminated ΔT_w excursion	Nearly eliminated ΔT_w excursion
	Local ΔT_{ONB} range	Local ΔT_{ONB} range
	2.6 K~7.4 K	4.3 K~8.0 K

2.3.5 Relationship of activated cavities with ΔT_{ONB} reduction

Figure 2.28 presents the obtained ΔT_{ONB} on the porous plates during initial run and immersion run. Actual pore size distribution on these porous plates was added in the top side. It was found that the scattered pore size distribution, such as the HPP1 and HPP3, was prone to cause a variable ΔT_{ONB}. The corresponding phenomenon during experiments was the occurrence of the local boiling. Besides, with the pore size distribution shifted to a large level, the ΔT_{ONB} on these porous plates was reduced.

Hsu's correlation [67] (Eq. 2.5) was considered to confirm the relationship between the active cavity range and ΔT_{ONB}. Although Hsu's correlation [67] was derived based on a conical cavity, good match was also found on structured surfaces in others research [93-94]. Calculated range of active cavities was shown in the left-hand side of Fig. 2.29. Cavities ranging inside the curve was considered as active for nucleation and outside was non-active for nucleation. The pore size distribution (PSD) was also shown on the right of Fig. 2.29. The detail information of the PSD can also be found in the

Table 2.2 and Fig. 2.6. The minimum and maximum pore sizes are defined based on the first derivative of the intruded volume with respect to the logarithm of the pore diameter $dV_{pore}/d(\log d)$. In my study, pores smaller than a threshold value 10^{-5} cm³/g are considered negligible and they represent a very small fraction of the total pore volume.

On the HPP1, when the local boiling occurred at the surface superheat of 18.0 K, the minimum diameter of active cavities was 0.23 μm and the maximum diameter of active cavities of 0.9 μm was depended on the actual maximum pore diameter of the HPP1. For the final occurrence of boiling at the surface superheat of 33.0 K, the diameter range of the active cavity was 0.10~0.9 μm. Based on the averaged ΔT_{ONB} (26.4 K), the diameter range of the active cavity was 0.16~0.9 μm. On the HPP2, the diameter range of the active cavity was 0.43~4.8 μm based on the averaged ΔT_{ONB} (11.9 K). On the HPP3, the active cavities range calculated from the ΔT_{ONB} was all included in the actual pore size range. For example, diameter range of active cavities was 1.2~12.1 μm for the first local boiling ΔT_{ONB} (4.3 K). With the final local ΔT_{ONB} of 8 .0 K, diameter range of active cavities was found in the green dot line, the diameter of active cavities was 0.64~12.7 μm.

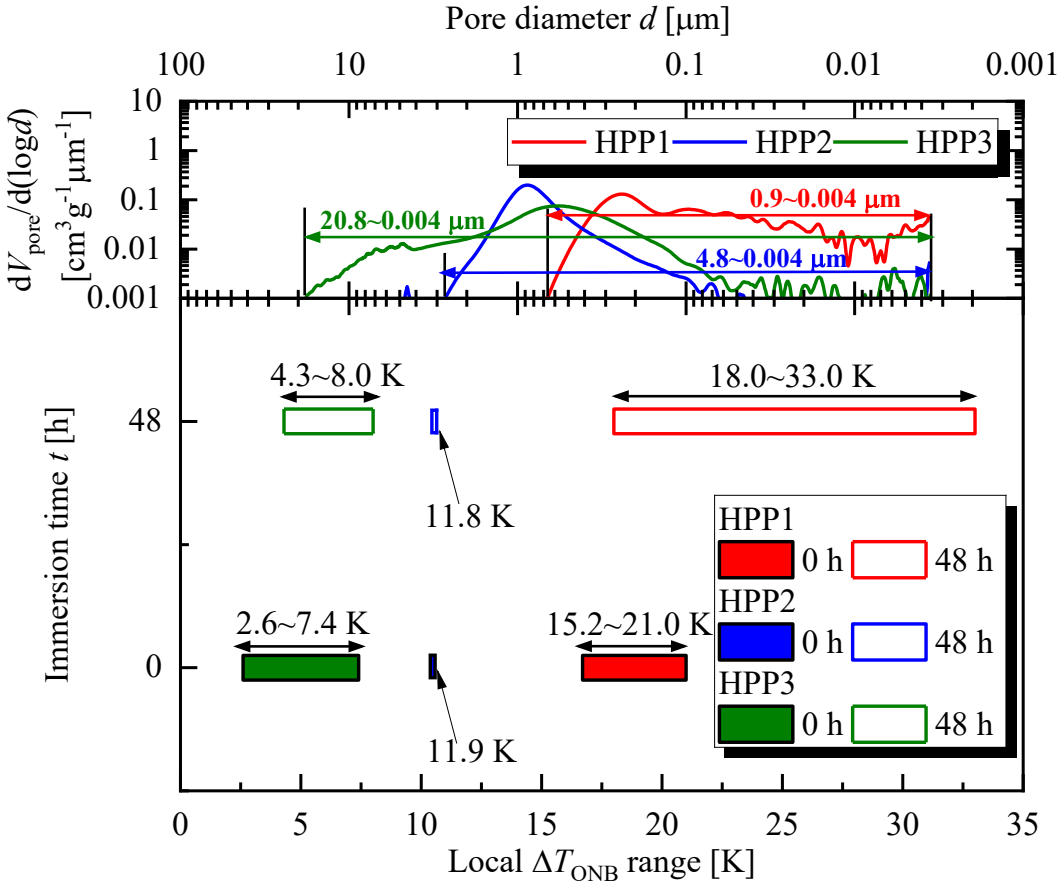

Fig. 2.28 Local ΔT_{ONB} distribution and pore size distribution of the HPPs.

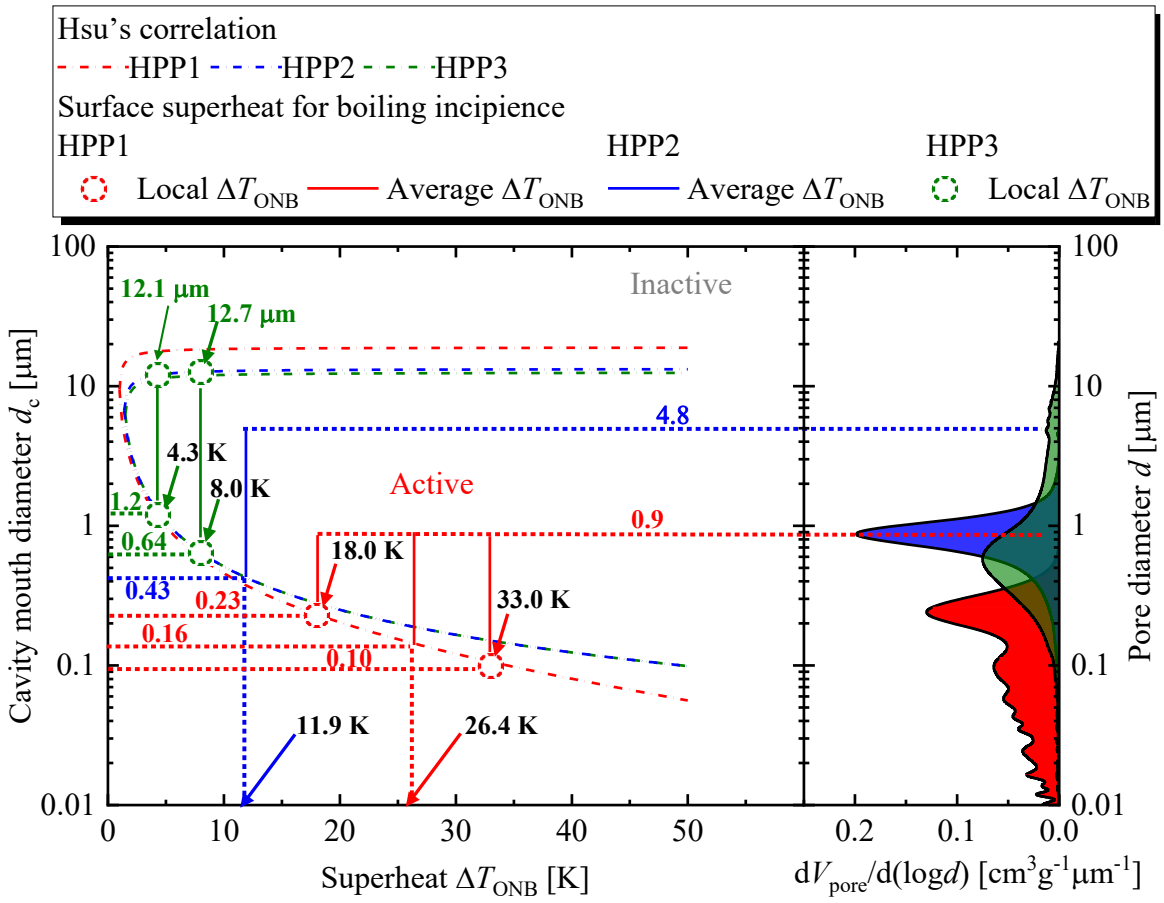

Fig. 2.29 Dependence of the range of the cavity diameter on the ΔT_{ONB} (Hsu model).

2.4 Conclusions

This chapter performed nucleate pool boiling on HPPs and plain surfaces (ITO heater surfaces) using saturated AE-3000 working fluid. Experimentally, the performance of boiling incipience temperatures on three different HPPs has been investigated. The results of the experiment are summarized below:

(1) In the initial test, significant decrease in ΔT_{ONB} was achieved on HPPs comparing with the plain surface. Particularly, nearly eliminated temperature excursion was achieved on the HPP3 having the peak pore diameter of 0.6 μm (pore diameter range: 0.004~20.8 μm).

(2) After immersion, increasing ΔT_{ONB} was observed on the porous plate with the smallest pore size range. Averaged ΔT_{ONB} was increased by 6.7 K on the HPP1 with peak pore diameters of 0.2 μm (pore diameter range: 0.004~0.9 μm).

(3) After immersion, reliable ΔT_{ONB} was still achieved on the porous plate with larger pore size

range. Particularly, nearly eliminated temperature excursion was also maintained on the HPP3.

(4) The scattered pore size distribution in the porous plates led to a variable range of ΔT_{ONB} which was related to local boiling in the HPP1 and HPP3. In contrast, a focused pore size distribution in the HPP2 resulted in boiling incipience at a single surface superheat, which is the average ΔT_{ONB} in boiling curves.

CHAPTER 3

Improvement in the onset of the nucleate pool boiling of AE-3000 with the use of a honeycomb porous plate and heated fine film

In the previous chapter (Chapter 2), increased ΔT_{ONB} was observed on the HPP1 during the restarting boiling experiment after immersing the HPP1 in the liquid (AE-3000) for 48 hours. The increase in ΔT_{ONB} indicated that cavities were flooded with the highly wetting AE-3000 liquid and nucleation sites underwent deactivation during the immersion period. In the current chapter, a novel approach was introduced to re-activate the flooded cavities by inserting a heated fined film (HF) between the HPP1 and ITO heater. Tiny bubbles were confirmed from the HF, which was helpful to replace liquid from the flooded cavities and then be effective in re-activating the flooded cavities on the HPP1. Besides, the influence of the heated film on the plain surface was also checked by setting the heated film above the ITO film. Finally, the focus of this chapter is to address the re-activation performance of the HF on the flooded cavities of the HPP1. Different voltage pattern was applied on the HF to investigate the ΔT_{ONB} during boiling experiments conducted after 48-h immersion.

3.1 Experimental apparatus and procedures

The boiling apparatus used in this chapter is similar to the one introduced in Chapter 2, except for the heating surface section. Setup for the HPP1 with the HF was described in Fig. 3.1. A heated fine film was installed horizontally, facing the ITO heater beneath the HPP1. Actual experimental setup was shown in the middle of the Fig. 3.1. To confirm good contact between the porous plate and the ITO heating surface, a channel for the HF insertion was made on the grid wall part of the HPP1, as shown in the right larger view of the HF part.

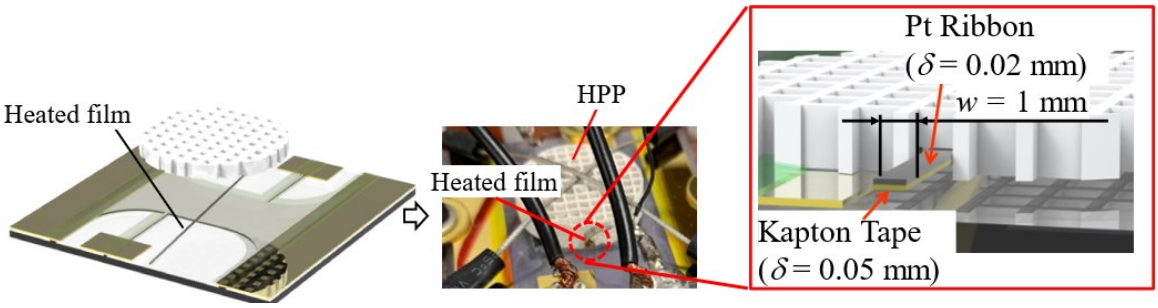

Fig. 3.1 Description of the HPP1 with the HF insertion.

Considering the HF surface condition such as roughness may have influence on the ΔT_{ONB}, boiling experiments was also performed on the section HPP1 with the HF without input power.

The dimensions of the heated film, including its width, length, and thickness, were 1 mm, 15 mm and 0.07 mm. The thickness of 0.07 mm for the heated film comprises 0.02 mm film made of Pt100 and 0.05 mm Kapton tape for insulation.

The heated fine film was connected to a DC power supply that generated current, as shown in Fig. 3.2. During this experiment, an Advantech data acquisition module (Keyence NR-500) was used to collect voltage and current signals from the test section.

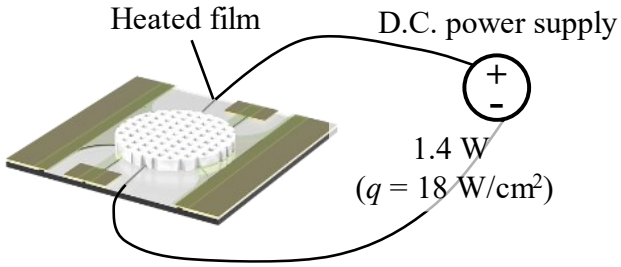

Fig. 3.2 Circuit description of the HPP1 with the HF insertion.

A consistent voltage of 1.0 V (corresponding to a heat flux of 18 W/cm^2) was applied to the HF. This voltage to the HF was very small compared to the stepwise increasing voltage supplied by the ITO heater as shown in Fig. 3.3.

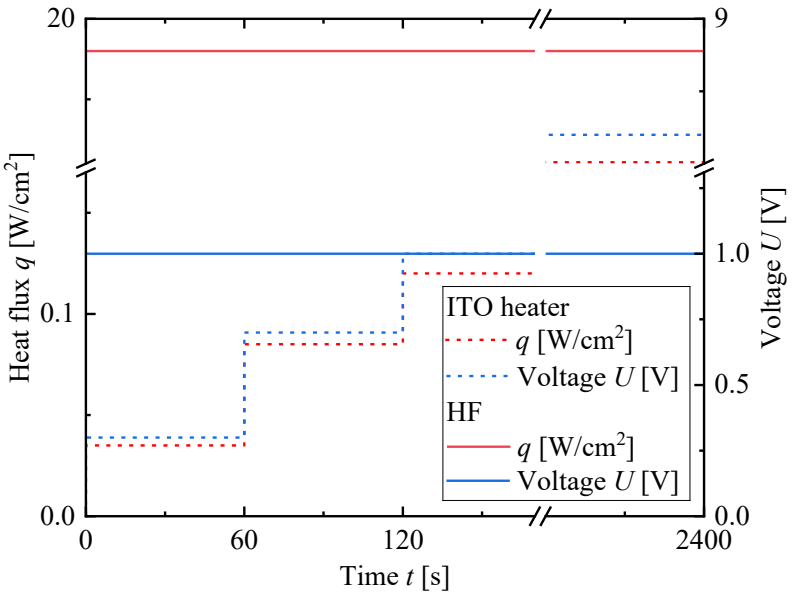

Fig. 3.3 Applied voltage to the HF (ITO heater voltage was added for reference).

Besides, this small input power to the HF was confirmed to be sufficient to generate bubbles, as evidenced by Fig. 3.4.

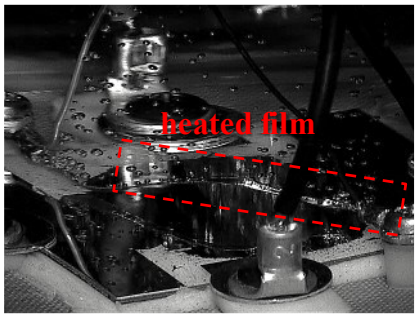

Fig. 3.4 Visualization of the bubbles generating from the HF for cavity reactivation.

Same experimental procedure as Chapter 2 was followed. AE-3000 was added to the boiling chamber until the interface was 60 mm above the boiling surface. The working liquid was boiled at 2.3 W/cm^2 for 2 hours to remove trapped gas. Heat flux was then increased gradually using an ITO heater while maintaining the liquid at saturation temperature. An IR camera captured the temperature of the boiling surface.

3.2 Results and discussion

3.3.1 Re-activation of the flooded cavities on the HPP1&HF

In Chapter 2, an overshoot at the ΔT_{ONB} the was observed after 48 hours of immersion on the HPP1, during which the surface superheat for boiling incipience increased at 34.3 K at most. To tackle the degraded ΔT_{ONB}, a hybrid section, HPP1 coupled with a heated film (HF), was investigated in this chapter. To isolate the effects of the surface geometry change by the HF insertion, boiling experiments were conducted on the hybrid section with no voltage supplied to HF, as shown in the red symbol with 'With the HPP1' label in Fig. 3.5. The overall tendency of the ΔT_{ONB} between initial and immersion test was attained. At the initial test (0 h), the local ΔT_{ONB} was approximately 8.1 K and the ΔT_{ONB} was approximately 17.3 K. Beyond ΔT_{ONB} of 17.3 K, bubble coverage of 70% was observed on the heating surface. After 48-h immersion, no local ΔT_{ONB} was found and the ΔT_{ONB} increased at 32.4 K, suggesting some cavities in the HPP1 became de-activated during the immersion period.

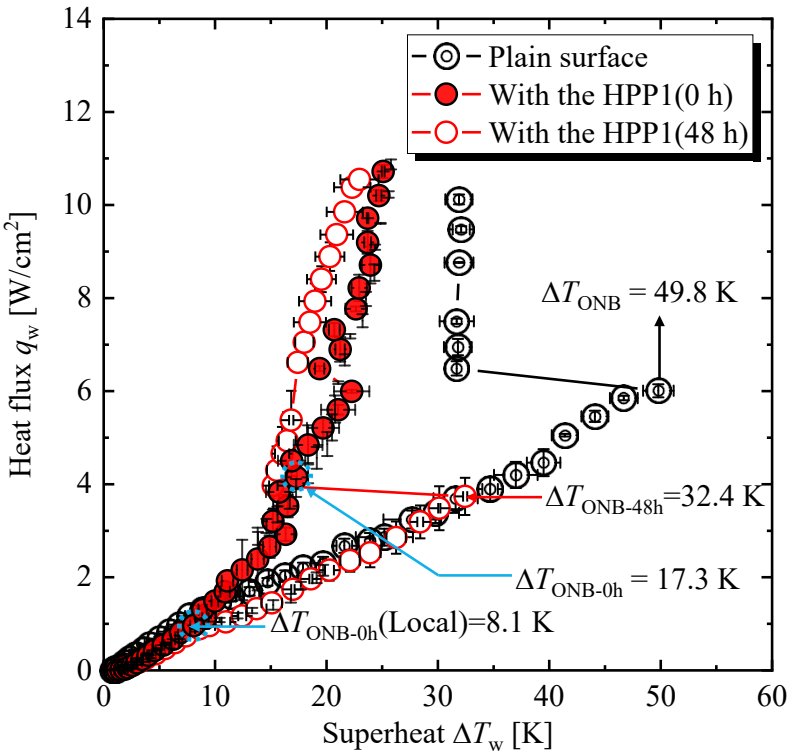

Fig. 3.5 De-activation of the cavities in the HPP1 after 48-h immersion.

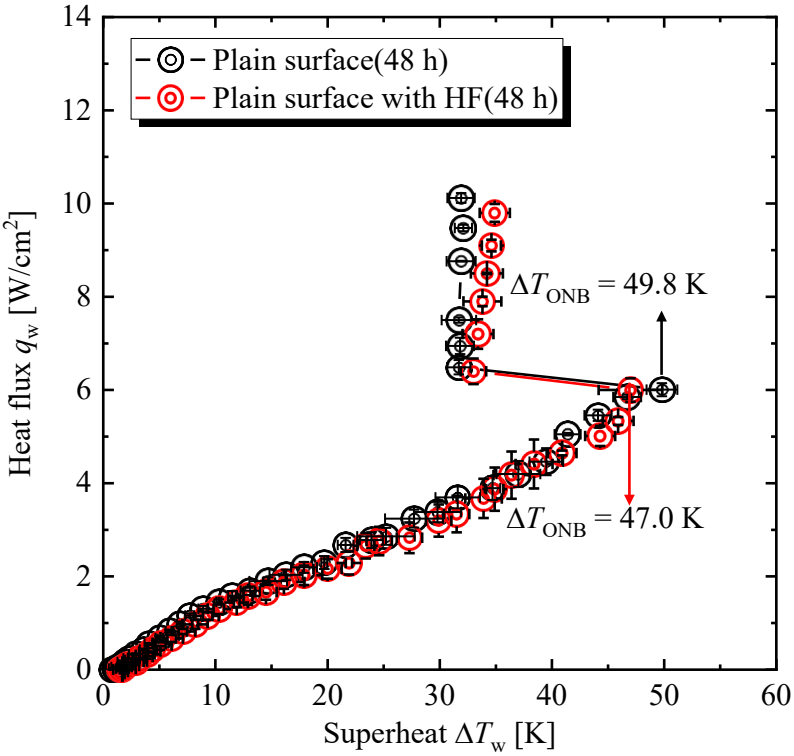

Fig. 3.6 Boiling curves on the plain surface and plain surface coupled with the HF after 48-h immersion.

Besides, influence of the tiny bubbles generated from the HF on the cavities on the on the plain surface (ITO film) was also checked. After immersing the plain surface coupled with the HF for 48 hours, boiling experiments were performed. The repeatable results shown in Fig. 3.6 indicated that these external tiny bubbles coming from the HF had no promotional effect on activating the cavities on the plain surface.

Boiling curves of the HPP1 with a heated HF were presented in Fig. 3.7. The local ΔT_{ONB} could not be recognized due to the presence of the pre-existing bubbles from the HF. However, for all the runs (0 h and 48 h), similar boiling phenomenon was observed. It is noted that nearly eliminated temperature excursion boiling curves were attained on the HPP1 coupled with the HF with localized boiling. The averaged ΔT_{ONB} was defined as the surface superheat for triggering bubbles covering 70% of the entire surface. The averaged ΔT_{ONB} was 21.3 K for the initial run and 19.6 K after 48-h immersion. Finally, surface superheat for boiling incipience after immersion for the HPP1, the plain surface coupled with a heated HF and the HPP1 coupled with a heated HF was summarized in Table 3.1.

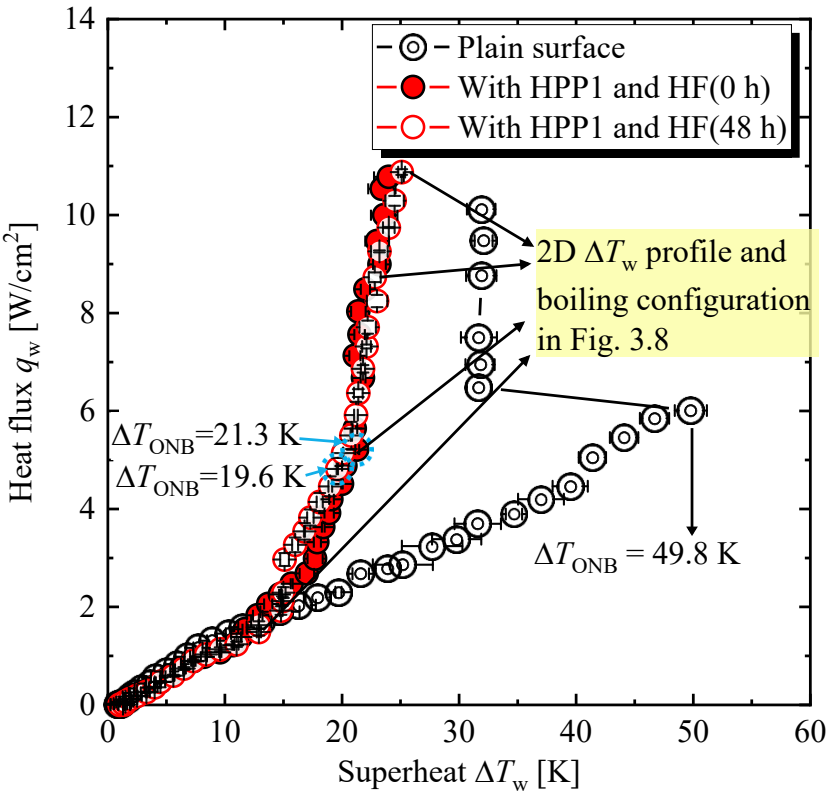

Fig. 3.7 Boiling curves of the HPP1&HF during the initial and restarting test after 48-h immersion.

Table 3.1 ΔT_{ONB} of the HPP1, the plain surface coupled with a heated HF and the HPP1 coupled with a heated HF.

Surface	Immersion run (48 h)
With the HPP1	32.4 K
Plain surface with the heated HF	47.0 K
HPP1 with the heated HF	19.6 K

To under the mechanism for the cavity's re-activation by the heated film. Boiling configuration and surface superheat distribution under different heat flux condition was shown later. As the surface temperature increased gradually, boiling started occurring in a localized manner on the HPP1 coupled with the HF section, as seen in the boiling configuration in Fig. 3.8. At the heat flux q_w of 1.6 W/cm^2, bubble nucleation always started from the surrounding grid walls of the HF. As the heat flux was increased further, More and more bubble generated in the area surrounding the HF. These bubbles then spread out among cells created for vapor channels. In the surface superheat distribution of Fig. 3.8, a local low superheat region was observed in the center, caused by the earlier nucleation from the surrounding cavities of the HF. Although this localized lower superheat region may underestimate the averaged surface superheat, the entire surface superheat was confirmed to be below the device operation temperature (85ºC).

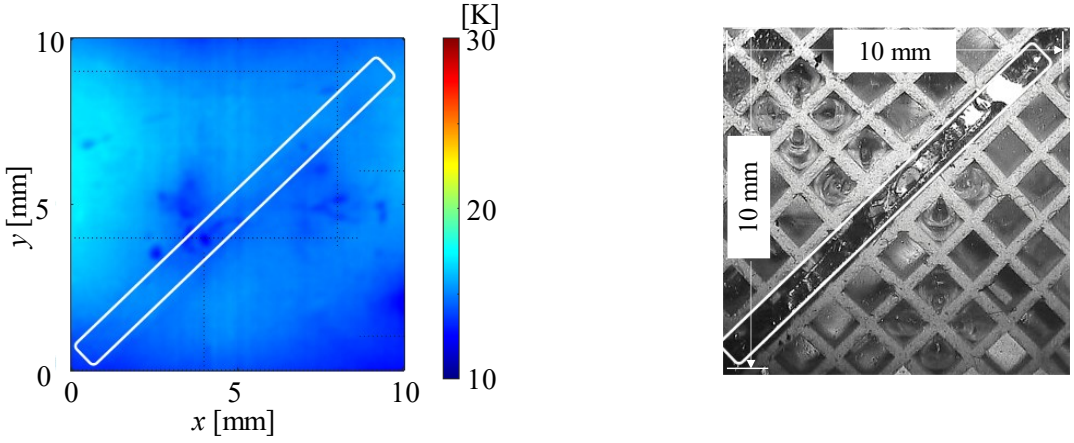

Surface superheat distribution Boiling configuration

(a)

Fig. 3.8 Surface superheat distribution (left) and boiling configuration (right) under the heat flux condition of (a) 1.6 W/cm^2 (ΔT_w = 12.9 K) (b) 5.1 W/cm^2 (ΔT_w = 20.1 K), (c) 8.7 W/cm^2 (ΔT_w = 22.8 K) and (d) 10.9 W/cm^2 (ΔT_w = 25.1 K).

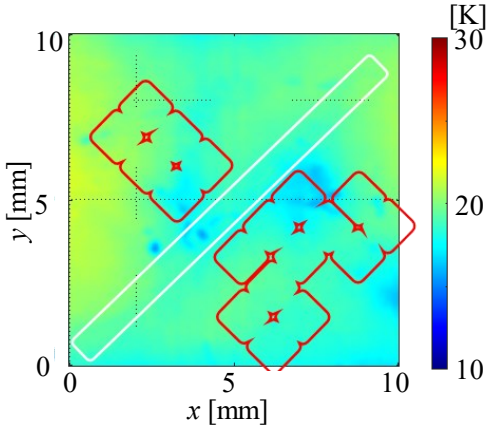

Surface superheat distribution

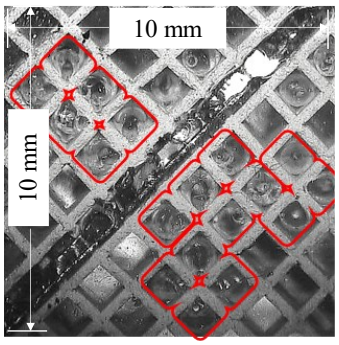

Boiling configuration

(b)

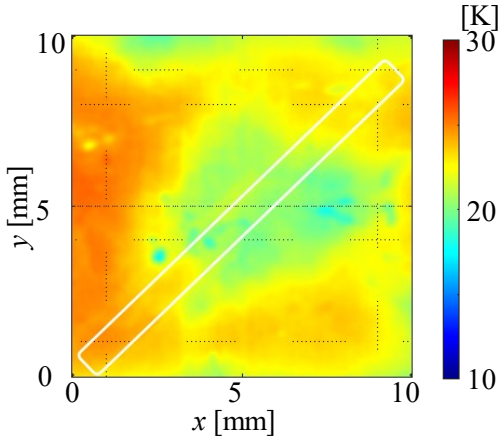

Surface superheat distribution

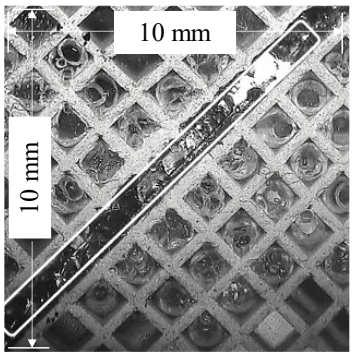

Boiling configuration

(c)

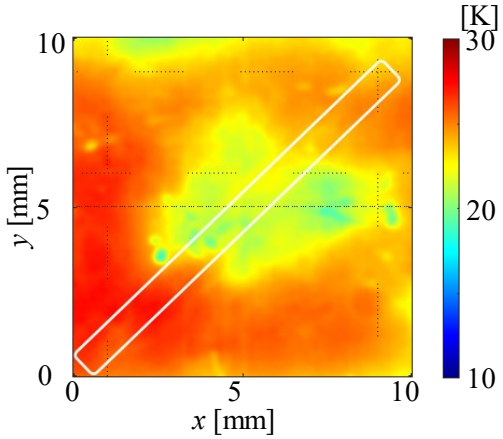

Surface superheat distribution

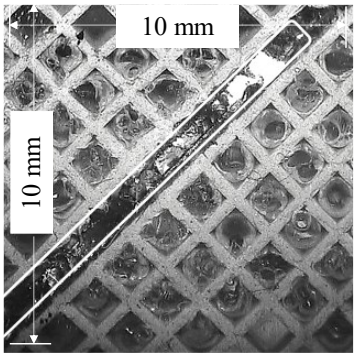

Boiling configuration

(d)

Fig. 3.8 (Continued).

In order to under the principle of the cavity re-activation by the HF, the nucleation patterns for

the HPP and HPP coupled with the HF after the 48-h immersion period are presented in Fig. 3.9. The magnified top views of the porous structure are shown in the bottom of the figure to clarify the difference in nucleation between the two surface sections. The gray part represents the solid ceramic material, and the spaces between the solid parts are the cavities prepared for nucleation. However, as shown in Fig. 3.9 (a), most of the prepared cavities for nucleation were flooded after 48 h of immersion in AE-3000 in the boiling vessel in contact with the HPP1, resulting in boiling hysteresis phenomena (ΔT_{ONB} = 32.4 K). When the heated fine film was utilized, tiny bubbles generated from the heated wire created interruptions in the bottom part of the HPP1 and replaced some flooded cavities during immersion, which promoted nucleation during boiling, as illustrated in Fig. 3.9 (b).

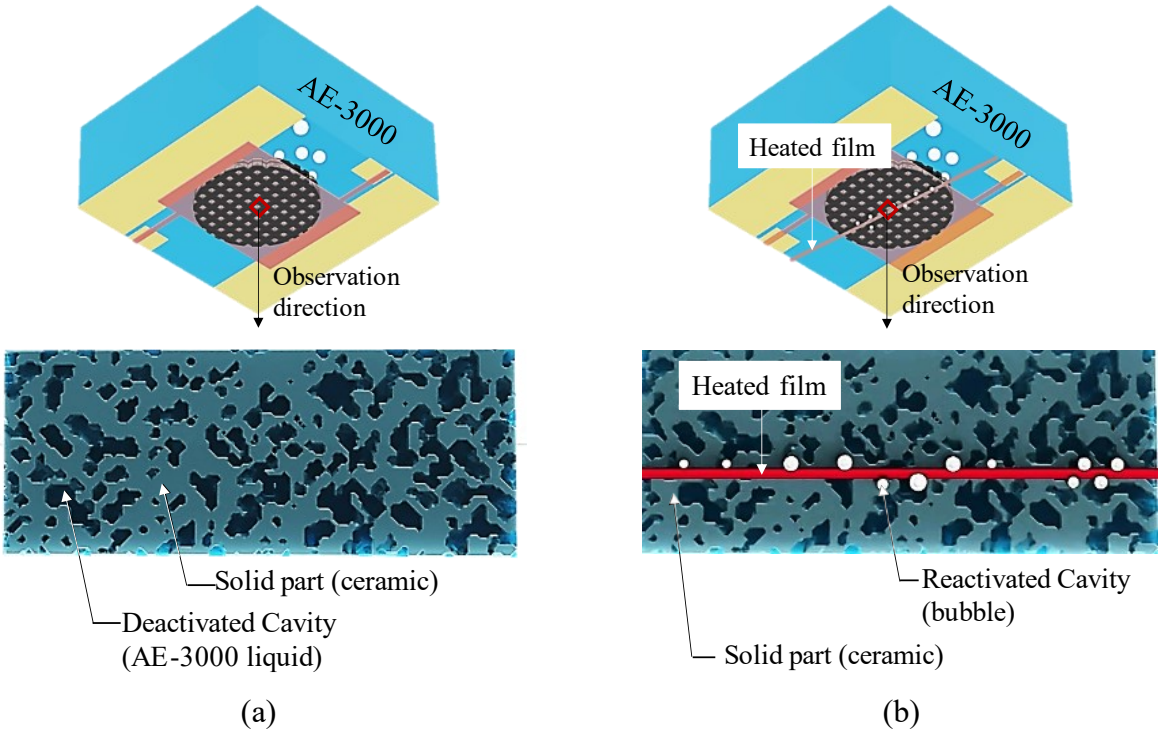

Fig. 3.9 (a) De-activation of the cavities of the HPP1 and (b) re-activation mechanism of the HPP1coupled with the HF.

The actual visualization for tiny bubbles generating from the heated film entering into the surrounding cavities was captured by the bottom HSV, as shown in Fig. 3.10. Once launching the HF, explosive boiling occurred on the HF, pushing bubbles entering into the surrounding cells of the HPP1 due to the increasing vapor pressure. These bubbles can potentially displace the liquid trapped within the flooded cavities and be trapped into the cavities. Besides, the heat flux of the heated film was confirmed by the generation of the bubble. In this study, the heated film was just for generating the seed bubbles for cavities re-activation. So, the influence of the heat flux was not included in.

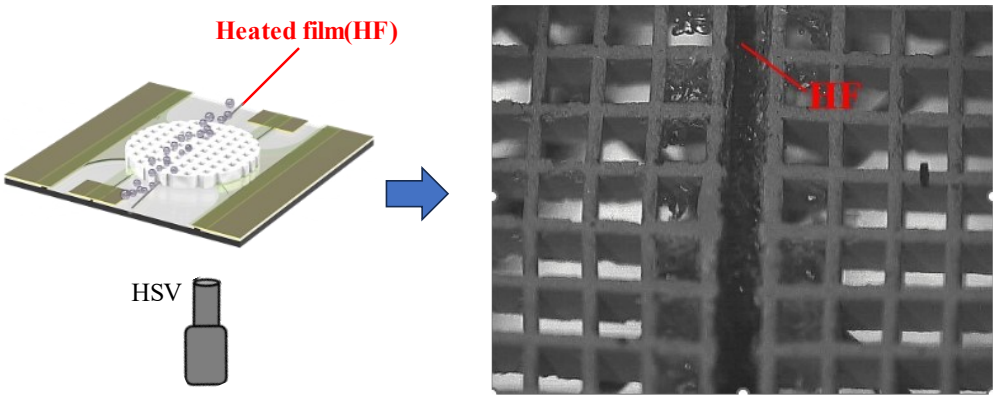

Fig. 3.10 Visualization of the tiny bubbles generating from the HF entering into the surrounding cells.

3.3.2 Relationship of activated cavities with ΔT_{ONB} reduction

Hsu's correlation [67] (Eq. 2.5 and 2.6) was considered to confirm the relationship between the active cavity range and ΔT_{ONB}. The thickness of the thermal boundary layer δ_T was calculated from the ΔT_{ONB} of each experiment. Figure 3.11 illustrates that the minimum diameter of the active cavity was determined by the superheat of ΔT_{ONB}, and the maximum diameter of the active cavity depended on the actual maximum pore diameter of the HPP1 (0.9 μm). The PSD of the HPP1 was shown on the right of Fig. 3.11 for reference. The detail information of the PSD can also be found in the Chapter 2 (Table 2.2 and Fig. 2.6).

The range of active cavities for each test was labeled with a solid line, and the area outside the solid line was considered an area of inactive cavities. Input the ΔT_{ONB} of the HPP1 of the initial (17.3 K) and 48-h immersion run (32.4 K). The active cavity diameter range of the HPP1 section was 0.24 ~ 0.9 μm for the initial run and 0.11 ~ 0.24 μm after 48 h. Nucleation cavities larger than 0.24 μm has been flooded by AE-3000 after 48 h of immersion. Only one third of the cavities in the HPP1 was effective for nucleation after immersion. These unflooded small cavities can be only active under the higher ΔT_{ONB} of 32.4 K. And such surface superheat was high enough for activating most of the cavities resulting in a better HTC than that of the 0 h.

With a heated HF, the active cavity diameter showed slight shifts and ranged from 0.19 ~ 0.9 μm and 0.21 ~ 0.9 μm at 0 and 48 h, as shown in Fig. 3.12. The flooded cavities filled with fluid during immersion were replaced by tiny bubbles from the HF, and the final active range for nucleation was averagely determined as: 0.2 ~ 0.9 μm. The average minimum diameter (0.2 μm) of nucleation

cavities matched the peak pore diameter (0.2 μm) of the HPP1 obtained through mercury penetration porosimetry, implying that the heated film successfully reactivated the most of cavities prepared for nucleation after immersion.

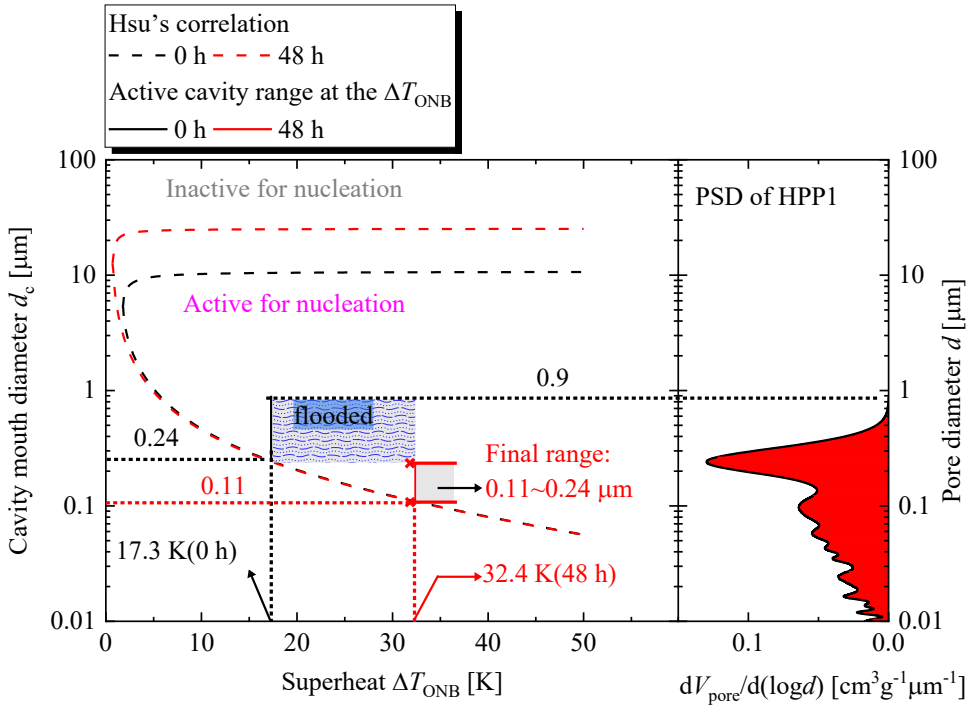

Fig. 3.11 Analysis of the re-activated cavity on the HPP1.

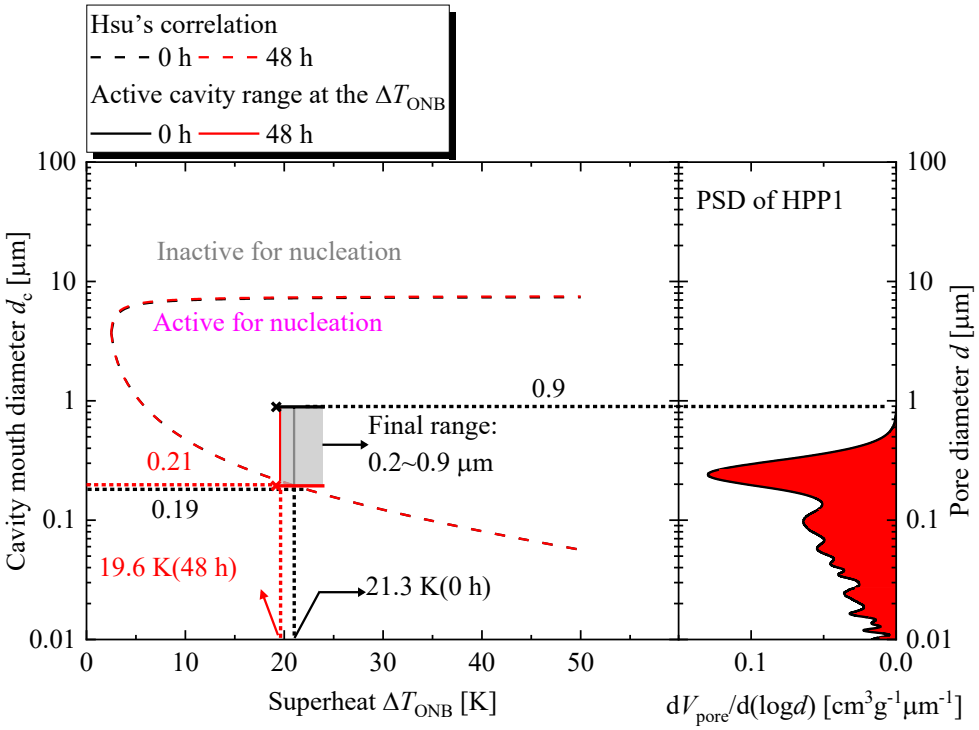

Fig. 3.12 Analysis of the re-activated cavity on the HPP1 coupled with a heated film.

3.3.3 Effect of the HF heating period on cavity re-activation (pulse voltage on the HF)

In this section, a discontinuous voltage was applied to the HF. A comparative study was conducted by applying different patterns of the discontinuous HF voltage with three different frequencies, as shown in Fig. 3.13:

a) *t*_on = 5 s for the HF with heating, *t*_off = 5 s for the HF without heating - repeated cyclically.

b) *t*_on = 10 s for the HF with heating, *t*_off = 10 s for the HF without heating - repeated cyclically.

c) *t*_on = 30 s for the HF with heating, *t*_off = 30 s for the HF without heating - repeated cyclically.

During the heating period, the value of the HF voltage was set to be the same as the continuous voltage applied to the HF in the previous section.

These different heating and waiting patterns were applied until the end of the experiments. The main motivation was to investigate the effect of these different HF patterns on the cavity reactivation process after 48 hours of immersion. Therefore, the results and discussion focused specifically on the data after 48 hours of immersion. Boiling curves of the HPP1 coupled with the heated HF with continuous applied voltage was also included for comparison.

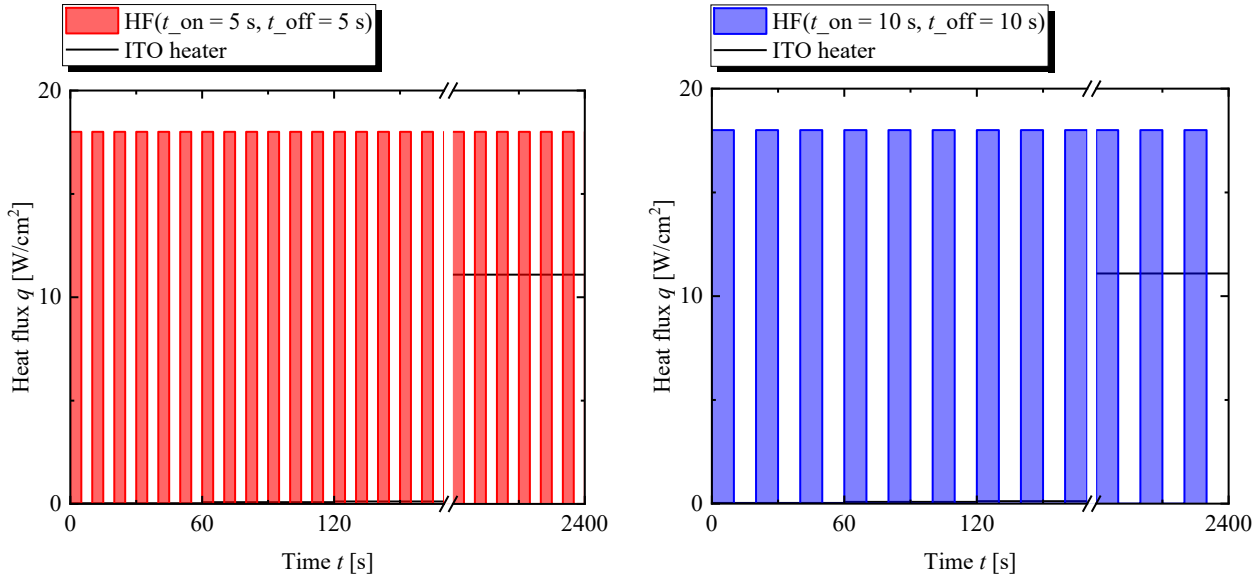

(a) (b)

Fig. 3.13 Applied voltage parameter of the HF (ITO heater voltage was added for reference) (a) repeatedly input power on the HF for 5 seconds and wait for 5 seconds, (b) repeatedly input power on the HF for 10 seconds and wait for 10 seconds and (c) repeatedly input power on the HF for 30 seconds and wait for 30 seconds.

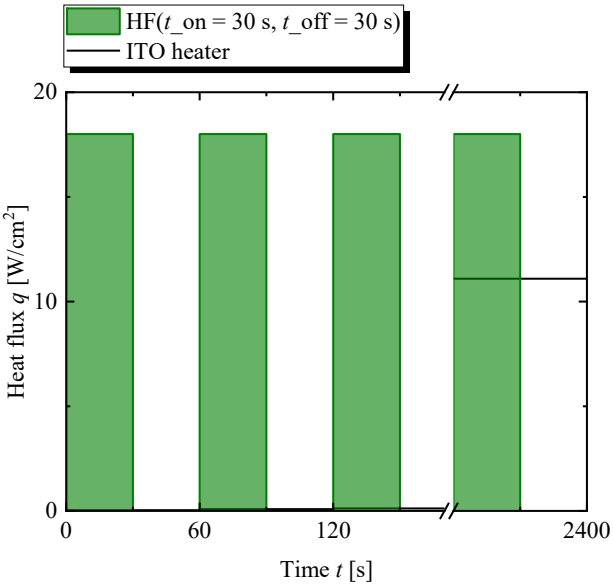

(c)

Fig. 3.13 (Continued).

Figure 3.14 shows the immersed boiling curve (48 h) for the HPP1&HF section when a cyclical t_on = 5 s, t_off = 5 s voltage pattern and t_on = 10 s, t_off = 10 s voltage pattern was applied to the HF, respectively. The boiling performance observed with these cyclical heated HF patterns was similar to the case with a continuously heated HF. Nearly eliminated temperature excursion boiling curves were also attained on the HPP1 coupled with these cyclical heated HF patterns. Also, because there is no clear temperature excursion during boiling process on the HPP1&HF with t_on = 5 s, t_off = 5 s and t_on = 10 s, t_off = 10 s voltage, surface superheat for triggering bubbles covering 70% of the entire surface was defined as the ΔT_{ONB}. After immersing HPP1&HF into the liquid for 48 hours, the ΔT_{ONB} of the HPP1 with the cyclical t_on = 5 s, t_off = 5 s HF pattern was about 23.4 K. And the ΔT_{ONB} of the HPP1 with the cyclical t_on = 10 s, t_off = 10 s HF pattern was about 22.5 K. The similarity in boiling performance between the cyclical and continuous cases suggests that cavity reactivation can be effectively achieved even with a pulsed voltage applied to the HF. This finding indicates that external power supplied to the HF for cavity reactivation can be reduced by using a pulsed voltage approach. The comparable performance between t_on = 5 s, t_off = 5 s and t_on = 10 s, t_off = 10 s patterns suggest that increasing the frequency beyond 10s ON/OFF may not provide additional benefits.

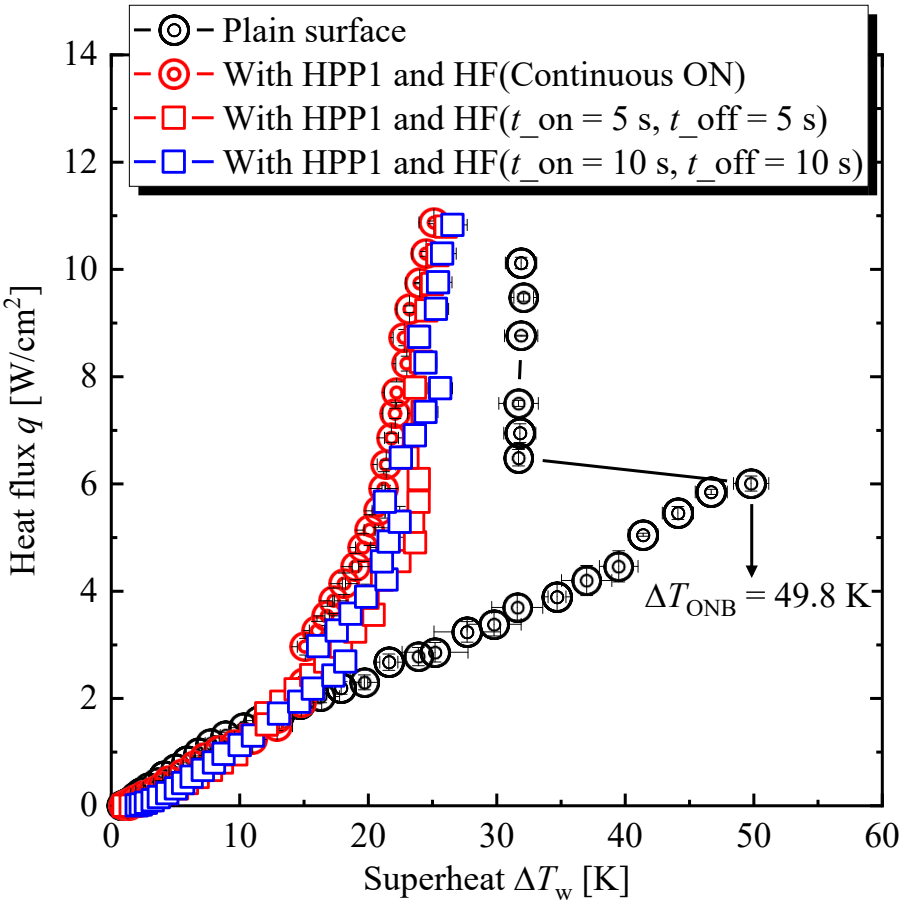

Fig. 3.14 Boiling curves of the HPP1&HF with a cyclical 5 seconds on and 5 seconds off and 10 seconds on and 10 seconds off voltage pattern after 48-h immersion.

Figure 3.15 shows the immersed boiling curve (48 h) for the HPP1&HF section when a t_on = 30 s, t_off = 30 s cyclical voltage pattern was applied to the HF. Different from the previous tested two cyclical heated HF cases, some surface superheats excursions were observed during the boiling process. HF with low frequency applied voltage showed worse delayed ΔT_{ONB} compared with the previous tested two cyclical heated HF cases. Although the heating time for the HF was longest.

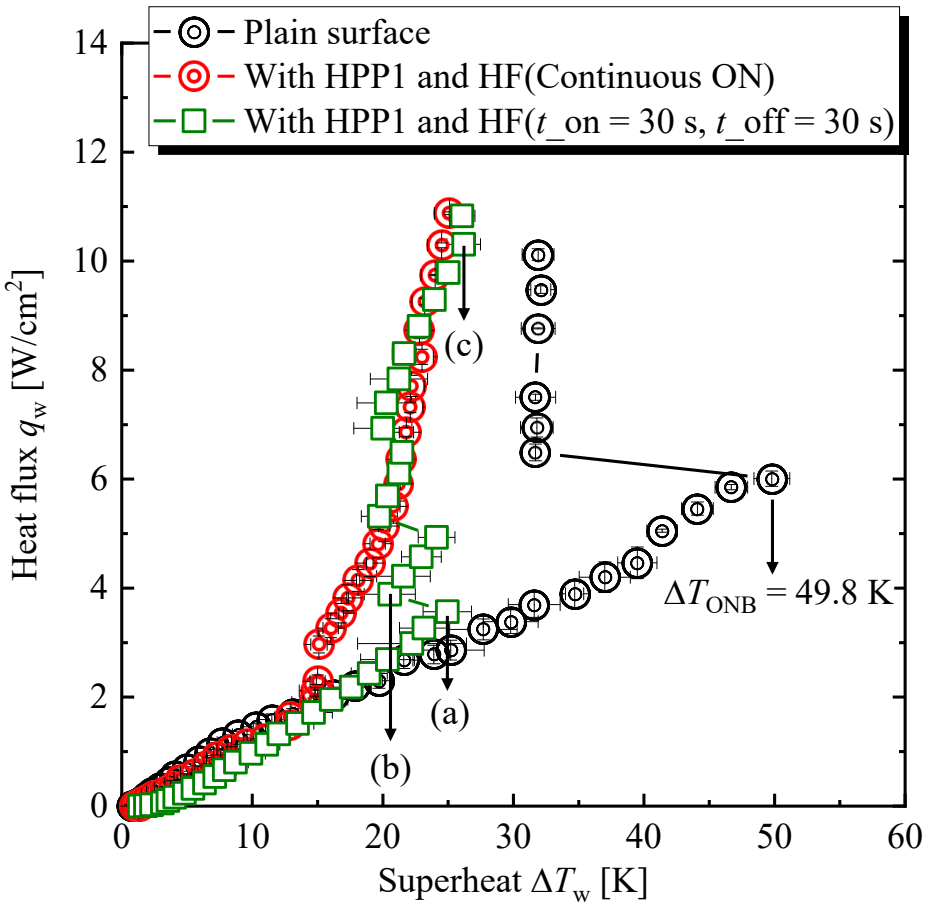

Fig. 3.15 Boiling curves of the HPP1&HF with a cyclical 30 seconds on and 30 seconds off voltage pattern after 48-h immersion.

On the HPP1&HF section with a t_on = 30 s, t_off = 30 s cyclical voltage pattern applied to the HF. There was limited vapor from the HF enter into the flooded cavities, which caused a delayed ΔT_{ONB}. For example, at the first delayed ΔT_{ONB} = 24.9 K, a liquid layer was found beneath the HF and ITO heater before the superheat drop, as shown in Fig 3.16 (a). This liquid layer existed from that point onwards. When the surface temperature was increased further, nucleation was triggered from the surrounding grid walls of this liquid layer, as depicted in Fig 3.16 (b). The reason behind the nucleation mechanism was considered as following. As the heat flux increased, the thermal boundary layer thickness over the heating surface grew larger. The occurrence of the liquid layer indicated that the thermal boundary layer thickness had become large enough to sustain some vapor generated from the heated HF, without allowing it to immediately condense. This sustained vapor from the HF could then potentially displace the liquid trapped inside the flooded cavities on the HPP1 surface, thereby reactivating those cavities and triggering nucleation from those sites.

For another delayed ΔT_{ONB} = 26.2 K, a surface superheat drops of 0.2 K was observed,

indicating the occurrence of new nucleation sites activating. However, such late nucleation under high heat flux conditions was likely triggered only at these high surface superheat levels. Figure 3.16 (c) shows the surface superheat distribution before this new nucleation event occurred. The local triggering superheat for this new nucleation site was found to be around 31.0 K. This 31.0 K triggering superheat already exceeds the recommended maximum operating temperature (85°C) for the device. Therefore, any superheat drops observed under high heat flux conditions after immersion should be carefully checked for their local nucleation triggering superheat levels.

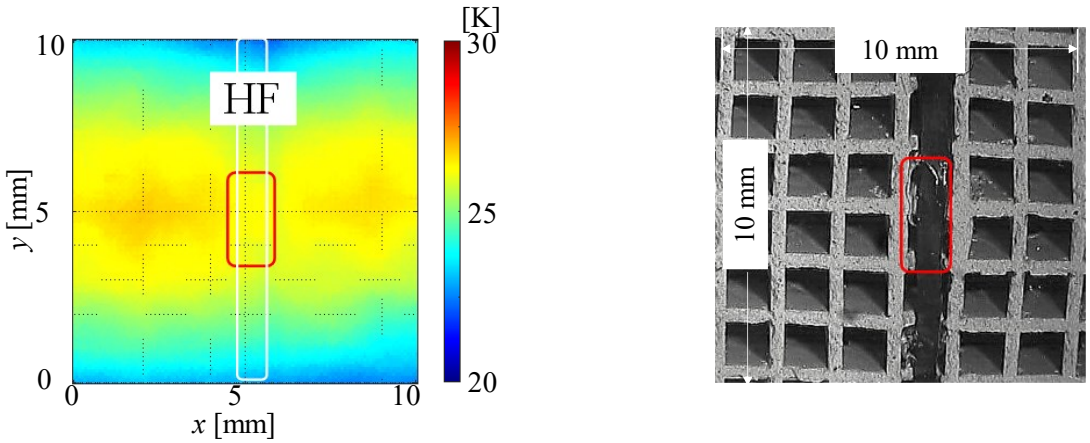

Surface superheat distribution Boiling configuration

(a)

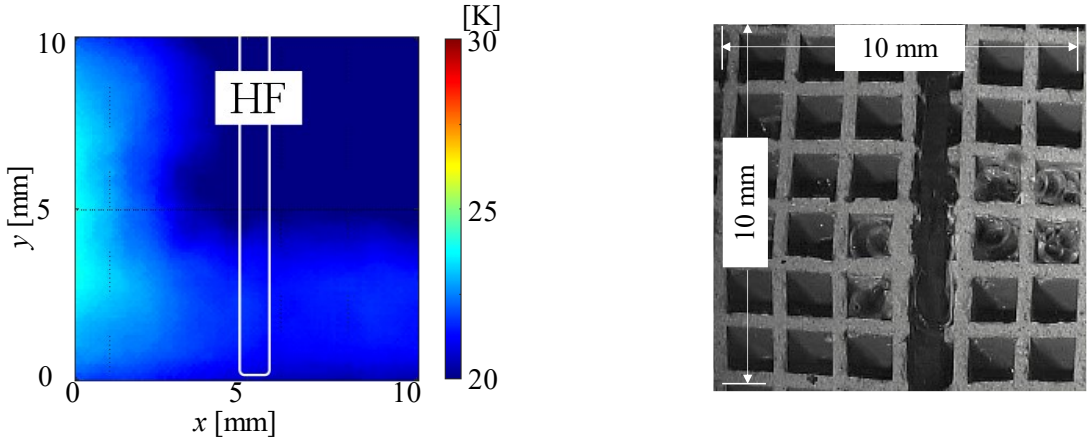

Surface superheat distribution Boiling configuration

(b)

Fig. 3.16 Surface superheat distribution (left) and boiling configuration (right) under the heat flux condition of (a) 3.6 W/cm^2 (ΔT_w = 24.9 K) (b) 3.9 W/cm^2 (ΔT_w = 20.5 K) and (c) 10.3 W/cm^2 (ΔT_w = 26.2 K).

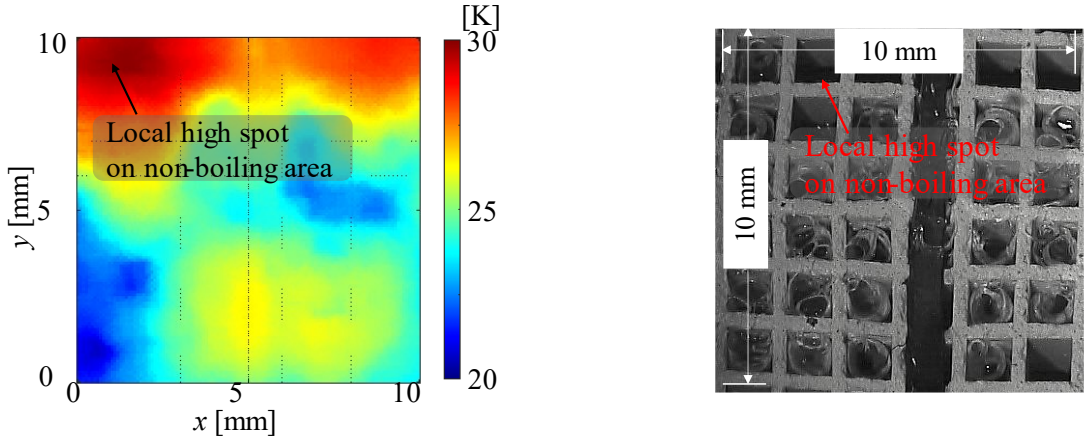

Surface superheat distribution Boiling configuration

(c)

Fig. 3.16 (Continued).

Here, surface superheat for boiling incipience on the HPP1 coupled with the heated HF with pulse applied voltage the was summarized in Table 3.2. For the applied HF voltage of 5s/5s and 10/10s, nearly eliminated boiling curves were attained, same as the continuous HF voltage section, the averaged ΔT_{ONB} was defined as the surface superheat for triggering bubbles covering 70% of the entire surface.

Table 3.2 ΔT_{ONB} of the HPP1 coupled with the heated HF with pulse applied voltage.

HF parameter	t_on = 5 s, t_off = 5 s	t_on = 10 s, t_off = 10 s	t_on = 30 s, t_off = 30 s
ΔT_{ONB}	20.4 K	21.0 K	24.9 K

3.3.4 Effect of the HF heating period on cavity re-activation (non-uniform voltage on the HF)

In a previous section, pulsed voltage heating with alternating 5 sec heating/5 sec waiting and 10 sec heating/10 sec waiting cycles was applied to a heated film. This pulsed heating maintained stable boiling performance after immersion. In this section, a non-uniform voltage was applied on the heated film to further investigate how much voltage/power consumption on the heated film can be reduced while still maintaining stable boiling performance. Two groups of comparative experiments are being done:

- Group 1: Comparing different non-uniform voltage patterns against the t_on = 5 s, t_off = 5 s pulsed pattern that achieved stable boiling previously. The HF voltage pattern was given in Fig. 3.17:

a) t_on = 5 s for the HF with heating, t_off = 15 s for the HF without heating - repeated cyclically, and the energy consumption with this pattern is 1/4 of the continuous HF input.

b) t_on = 5 s for the HF with heating, t_off = 25 s for the HF without heating - repeated cyclically, and the energy consumption with this pattern is 1/6 of the continuous HF input.

During the heating period, the value of the HF voltage was set to be the same as the continuous voltage applied to the HF in the previous section.

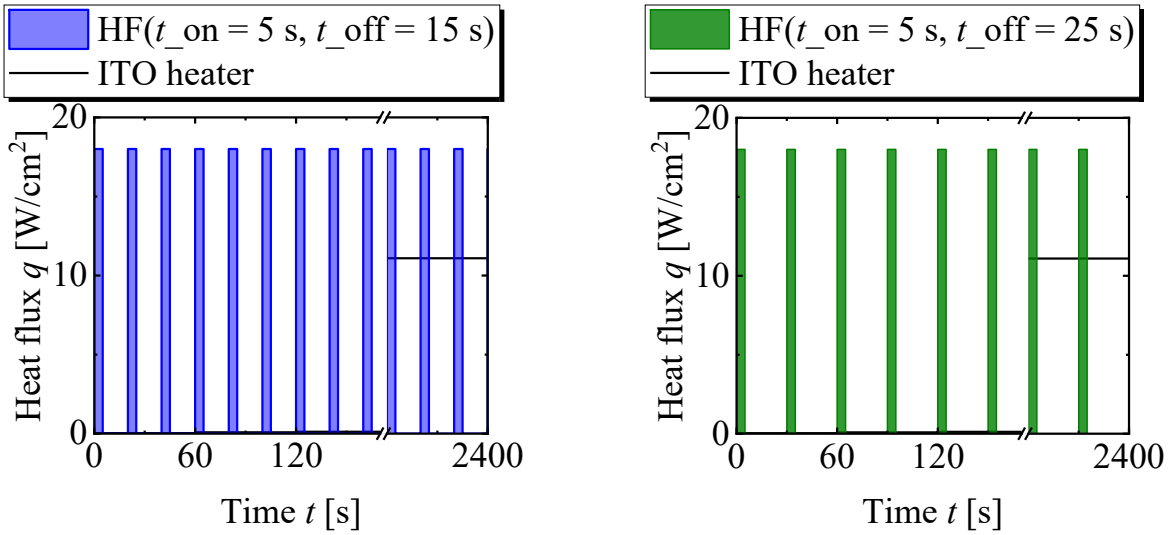

(a) (b)

Fig. 3.17 Non-uniform voltage parameter of the HF (ITO heater voltage was added for reference) (a) repeatedly input power on the HF for 5 seconds and wait for 15 seconds and (b) repeatedly input power on the HF for 5 seconds and wait for 25 seconds.

- Group 2: Comparing different non-uniform voltage patterns against the t_on = 10 s, t_off = 10 s pulsed pattern that achieved stable boiling previously. The HF voltage pattern was given in Fig. 3.18:

  a) t_on = 10 s for the HF with heating, t_off = 20 s for the HF without heating - repeated cyclically, and the energy consumption with this pattern is 1/3 of the continuous HF input. With a relatively short waiting period, this pattern is expected to maintain adequate ΔT_{ONB} by quickly resuming heating.

  b) t_on = 10 s for the HF with heating, t_off = 30 s for the HF without heating - repeated cyclically, and the energy consumption with this pattern is 1/4 of the continuous HF input.

  c) t_on = 10 s for the HF with heating, t_off = 50 s for the HF without heating - repeated cyclically, and the energy consumption with this pattern is 1/6 of the continuous HF input.

Most importantly, the period for the stepwise heat flux of the ITO heater was 60 s. If the heating period for the HF was constant of 10 s, the maximum waiting period was 50 s. In other word, this pattern was expected to save most energy consumption of the HF.

During the heating period, the value of the HF voltage was set to be the same as the continuous voltage applied to the HF in the previous section.

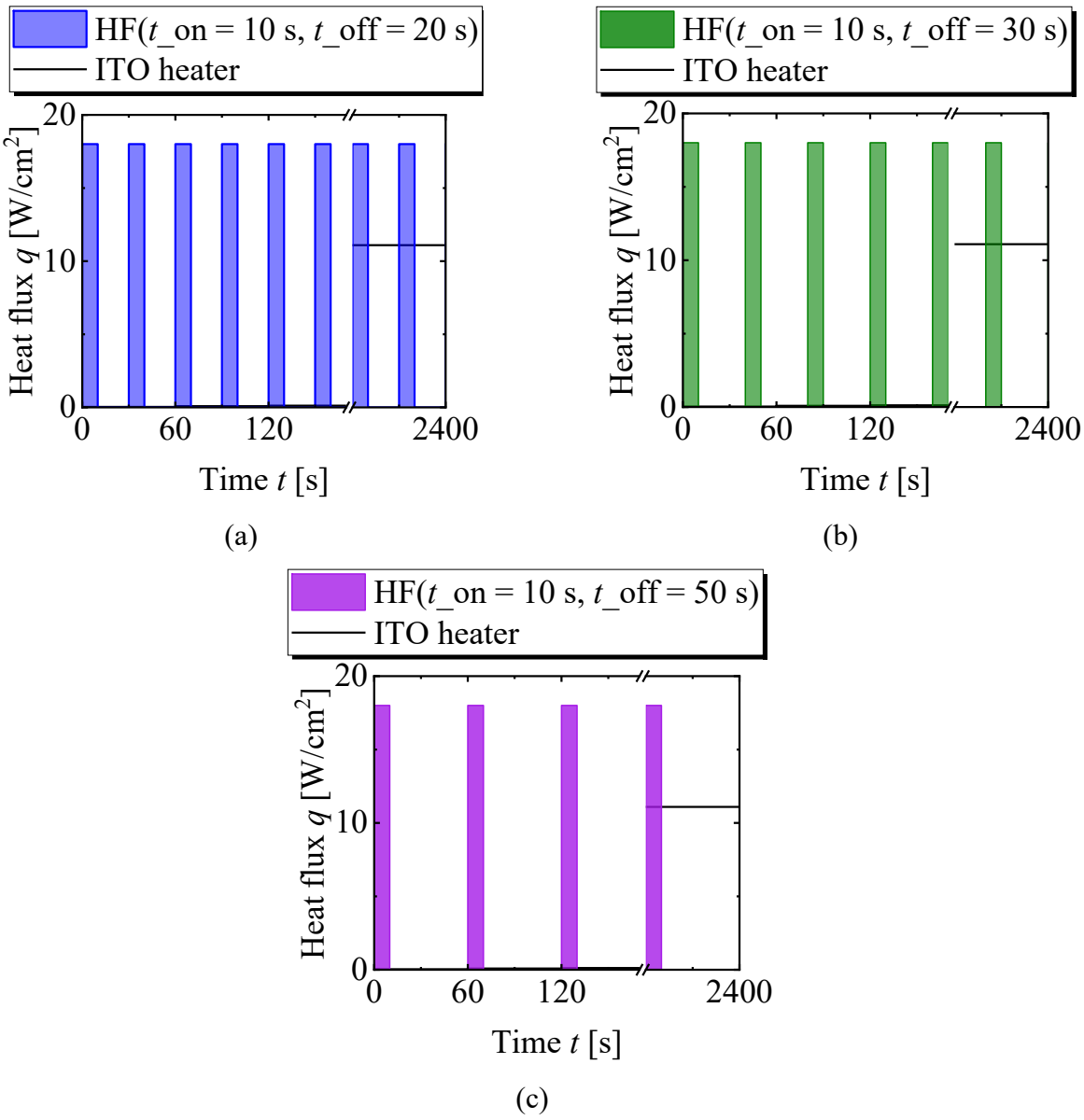

Fig. 3.18 Non-uniform voltage parameter of the HF (ITO heater voltage was added for reference) (a) repeatedly input power on the HF for 10 seconds and wait for 20 seconds, (b) repeatedly input power on the HF for 10 seconds and wait for 30 seconds and (c) repeatedly input power on the HF for 10 seconds and wait for 50 seconds.

Figure 3.19 shows the immersed boiling curve (48 h) for the HPP1&HF section with a cyclical non-uniformed HF voltage pattern (5 sec heating/15 sec waiting and 5 sec heating/25 sec waiting cycles). The ΔT_{ONB} of the HPP1 with the cyclical $t\_on = 5$ s, $t\_off = 15$ s HF pattern was about 22.3 K. And the ΔT_{ONB} of the HPP1 with the cyclical $t\_on = 5$ s, $t\_off = 25$ s HF pattern was about 27.4 K. The results of the ΔT_{ONB} were summarized in Table 3.3. As a conclusion, applying the cyclical 5s ON/25s OFF voltage on the HF can still trigger boiling below the operation temperature (77.3℃ < 85℃) although it showed a temperature excursion. With increasing the waiting time from 15s to 25s for the HF input voltage, occurrence of boiling was significantly delayed, which was almost same with operation temperature (82.4℃).

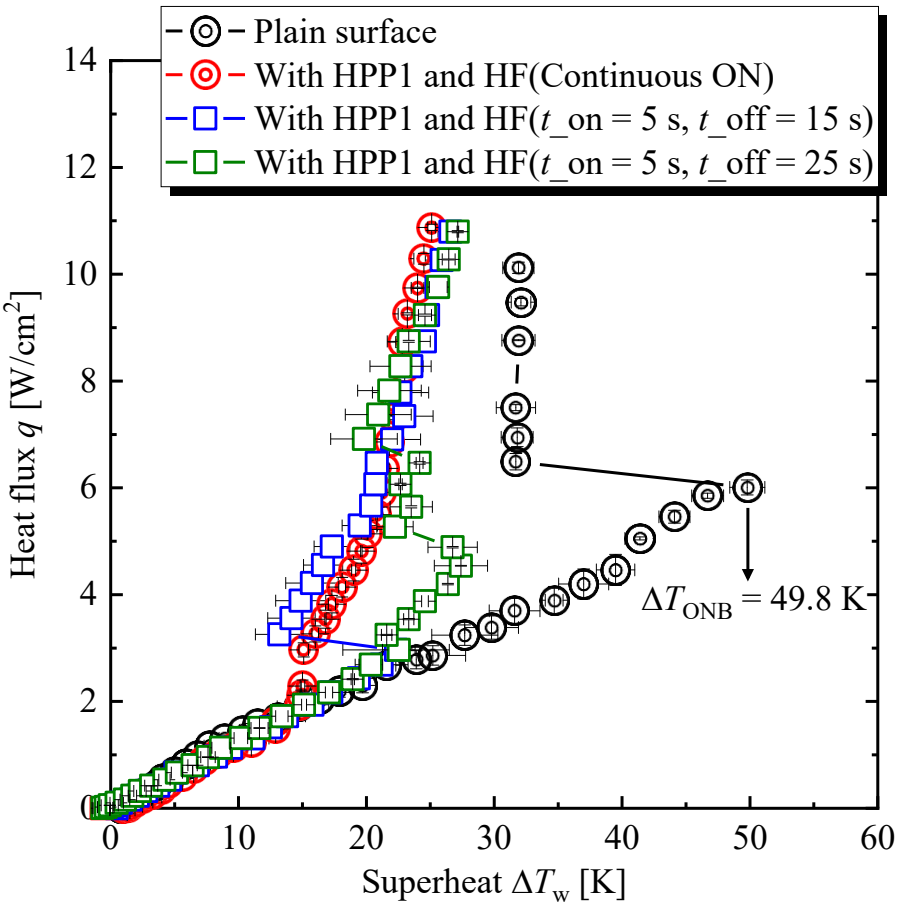

Fig. 3.19 Boiling curves of the HPP1&HF with a cyclical 30 seconds on and 30 seconds off voltage pattern after 48-h immersion.

Table 3.3 ΔT_{ONB} of the HPP1 coupled with the heated HF with non-uniformed applied voltage.

HF parameter	$t\_on = 5$ s, $t\_off = 15$ s	$t\_on = 5$ s, $t\_off = 25$ s
ΔT_{ONB}	22.3 K	27.4 K

Figure 3.20 shows the immersed boiling curve (48 h) for the HPP1&HF section with a cyclical non-uniformed HF voltage pattern (10 sec heating/20 sec waiting, 10 sec heating/30 sec waiting and 10 sec heating/50 sec waiting cycles). The results of the ΔT_{ONB} were summarized in Table 3.4. The cyclical heating patterns with 10s heating and varying waiting periods (20s, 30s, 50s) all show delayed boiling occurrence after immersion. It was suggested that for a constant 10s heating period, utilizing a pulsed voltage HF heating pattern (with shorter waiting times) would be a better option to maintain a more stable and consistent ΔT_{ONB} compared to the longer waiting period cycles tested.

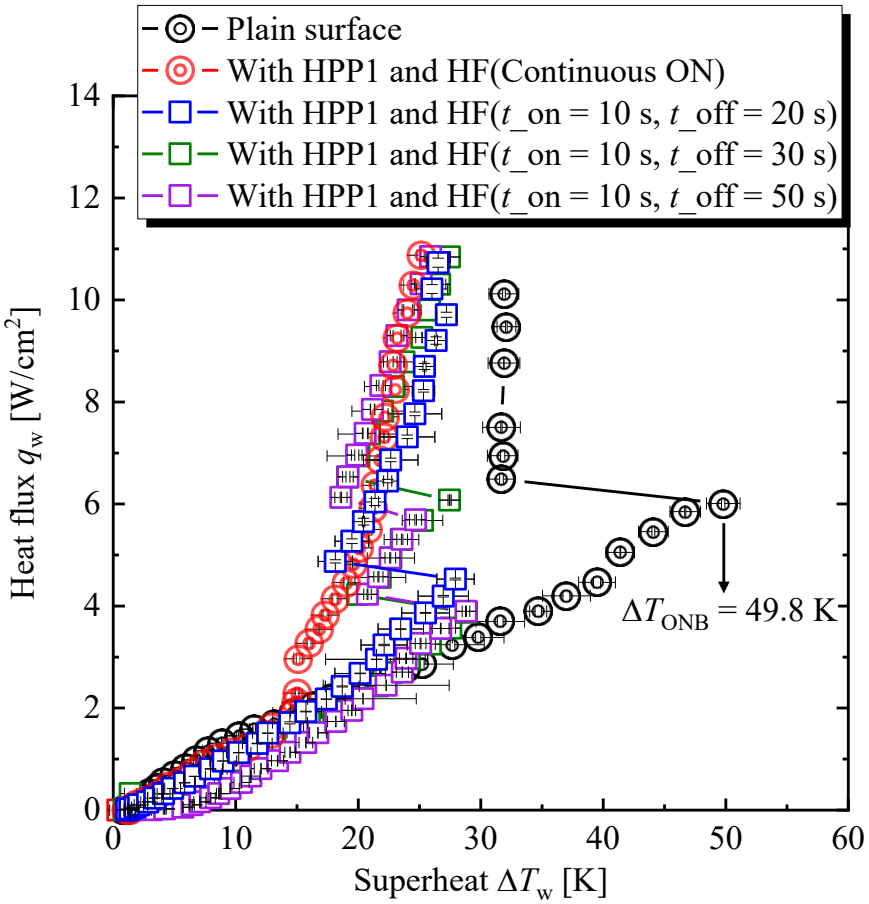

Fig. 3.20 Boiling curves of the HPP1&HF with a cyclical 30 seconds on and 30 seconds off voltage pattern after 48-h immersion.

Table 3.4 ΔT_{ONB} of the HPP1 coupled with the heated HF with non-uniformed applied voltage.

HF parameter	t_on = 10 s, t_off = 20 s	t_on = 10 s, t_off = 30 s	t_on = 10 s, t_off = 50 s
ΔT_{ONB}	27.9 K	27.5 K	28.8 K

Finally, a 3D plot analyzing the tradeoff between the superheat required for the onset of nucleate boiling ΔT_{ONB} and the potential for saving heated film (HF) voltage by using intermittent or pulsed heating patterns. The red bars represent ΔT_{ONB} under different heating condition of the HF after immersion. The green bars represent ratio of the saving voltage on the HF compared with continuous voltage. The reliable ΔT_{ONB} range was set as the value lower than the ΔT_{ONB} (ΔT_{ONB} = 26.4 K) for the HPP1&HF with a t_on = 30 s, t_off = 30 s cyclical HF pattern. Although this averaged ΔT_{ONB} was still below the operation temperature (85ºC), but local hotspot with a local ΔT_{ONB} of 31.0 K (85ºC) at higher high flux was found. Thus, to mitigate the risk of premature boiling incipience and ensure reliable operation, averaged ΔT_{ONB} for the HPP1&HF with a t_on = 30 s, t_off = 30 s cyclical HF pattern was used as the reference value.

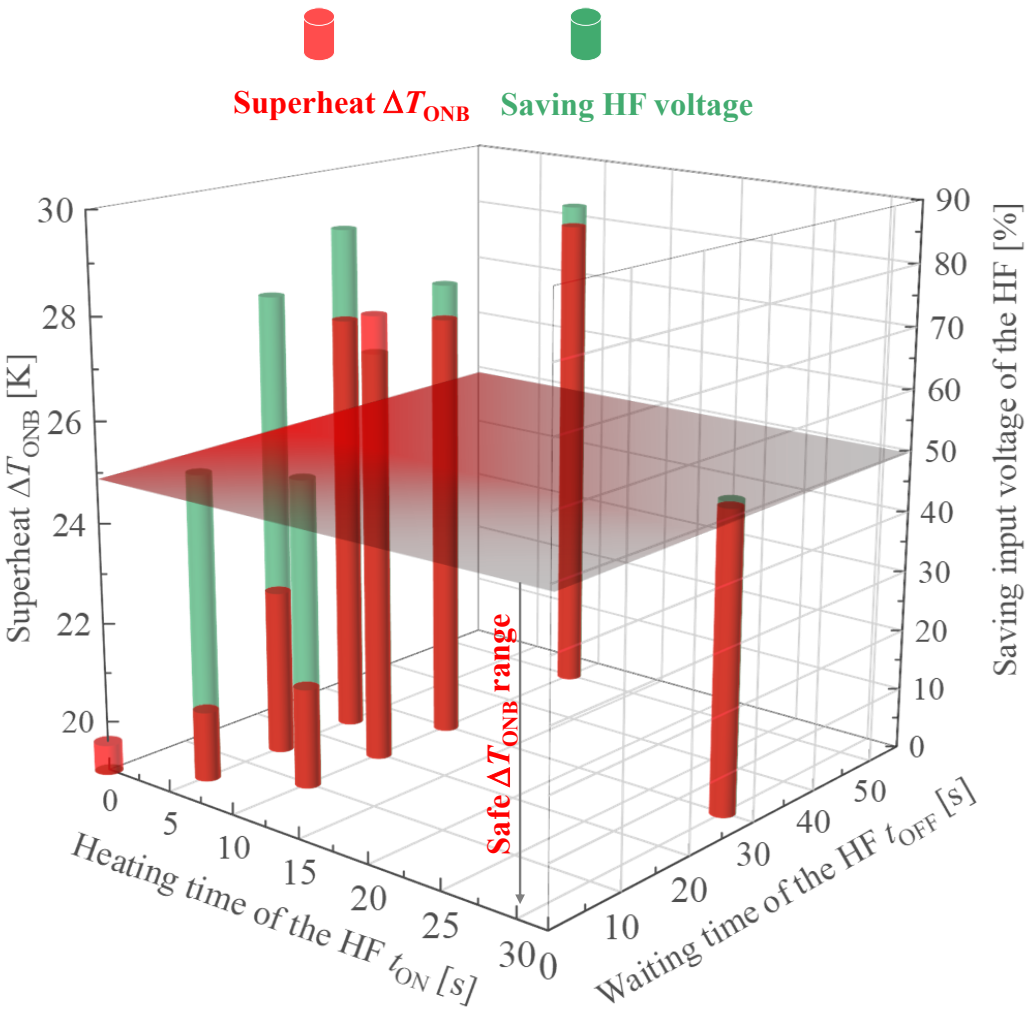

Fig. 3.21 3D tradeoff plot between the ΔT_{ONB} and the potential for saving heated film (HF) voltage.

As a result, no stable ΔT_{ONB} was achieved when waiting period for the HF applied voltage was longer than 20s. Among the HF condition below operation temperature, the best option for saving HF voltage (taller green bars) was 5 sec heating/15 sec waiting. And for a best boiling incipience superheat, the best HF pattern was 5s and 10s pulse voltage pattern.

3.4 Conclusion

In this chapter, nucleate pool boiling experiments were performed on the HPP1 coupled with a fine heated film (HF). Continuous and discontinuous voltage was applied to the HF. The performance of the nucleation cavities of the HPP1 at the onset of nucleate pool boiling during immersion time was investigated experimentally. The results are summarized as follows:

(1) The superheat at boiling incipience on the HPP1 was sensitive to immersion time. It deteriorated during immersion, and the superheat of ΔT_{ONB} on the HPP1 was 32.4 K.

(2) The hybrid section - HPP1 coupled with a heated fine film with continuous voltage could provide more stable nucleation over immersion time. In addition, the range of active cavities calculated on the basis of Hsu's model showed slight changes when the heated fine film was used, and the average minimum diameter for nucleation was close to the median pore diameter of the HPP1, indicating that the heated film was effective in sustaining active cavities for nucleation after immersion.

(3) Based on the analysis of the boiling curves among the different pulse HF voltage patterns (5s ON/OFF, 10s ON/OFF, and 30s ON/OFF), it was concluded that heating the HF with a higher frequency voltage pulsing pattern is beneficial for facilitating vapor entrapment within the flooded cavities on the HPP1 surface.

(4) It was found that a pulsing frequency of 10s ON/OFF was sufficient for achieving effective cavity reactivation. Increasing the frequency further by going to shorter ON/OFF periods like 5s ON/OFF did not provide any significant additional benefits in terms of cavity reactivation and boiling performance enhancement.

(5) Based on the analysis of the boiling curves among the different HF voltage patterns, it was concluded that waiting period for the HF applied voltage longer than 20s are impossible to provide a reliable ΔT_{ONB}. The best option for saving HF voltage was 5s ON /15s OFF pattern. And for a best boiling incipience superheat, the best HF pattern was 5s ON /5s OFF and 10s ON /10s OFF.

CHAPTER 4

Summary and prospect

The final chapter summarizes the research findings of all the above chapters and provides a prospect for future research.

4.1 Summary

Boiling is an efficient heat dissipation method implemented in microelectronic devices. However, given that microelectronic components have operating temperature limits (below 85°C), suitable coolants and enhanced technology for the onset of nucleate pool boiling are crucial for their further application. The dielectric liquids possess superior environmental properties and a low boiling point that can satisfy the requirement for engineered surfaces in the nucleate boiling region. However, higher superheating at ΔT_{ONB} is observed before nucleate boiling is triggered due to the high wettability of dielectric liquids. The surface temperature for triggering boiling on the original section was almost close to the operation temperature limitation, enhanced technology with an early ΔT_{ONB} has a pivotal role in further operation.

The focus of this paper is to investigate the effectiveness of the cavities in promoting vapor embryo and reducing the ΔT_{ONB} in immersion boiling of AE-3000. The emphasis of the experiments was on incipient boiling temperature, the critical heat flux (CHF) was not included in this study. Nucleate pool boiling experiments on the HPP were performed to investigate the ΔT_{ONB} promotion. Particularly, a stable reducing ΔT_{ONB} was also necessary for prolonged immersion cooling. Thus, nucleate pool boiling experiments were restarted after immersing a plain surface and HPP in AE-3000 for 48 h.

Firstly, we introduce honeycomb porous plates (HPP) with varied cavity ranges to promote the ΔT_{ONB}. Three HPPs were designed: HPP1 (peak pore diameter 0.2 μm, range 0.004-0.9 μm), HPP2 (0.9 μm, 0.004-4.8 μm), and HPP3 (0.6 μm, 0.004-20.8 μm). Initial tests revealed that HPPs significantly lowered the ΔT_{ONB} compared to a plain surface, with HPP3 nearly eliminating temperature excursions.

Crucially, we examined boiling performance after 48-hour immersion to assess long-term stability. HPP1, with the smallest pores, showed an increased ΔT_{ONB} by 6.7 K due to cavity flooding. In contrast, HPP3 maintained a reliably low ΔT_{ONB} with minimal temperature excursions. We observed that scattered pore sizes in HPP1 and HPP3 led to variable ΔT_{ONB} due to local boiling, while

HPP2's focused pore distribution resulted in uniform ΔT_{ONB} without local boiling.

To solve cavity flooding in HPP1, we introduced a novel hybrid surface section coupling HPP1 with a fine heated film (HF). Continuous low-power HF voltage stabilized nucleation, with Hsu's model confirming HF effectiveness in sustaining active cavities. Further, we found that pulse HF voltage (5s ON/OFF and 10s ON/OFF) can also reactivated flooded cavities after immersion.

Lastly, we optimized HF pulsing patterns for energy efficiency and performance. A 5s ON/15s OFF pattern best saved HF consumption voltage, while 5s ON/5s OFF or 10s ON/10s OFF patterns provided the lowest ΔT_{ONB}. These findings demonstrate that intermittent, high-frequency HF heating can maintain low ΔT_{ONB} while reducing energy consumption.

In conclusion, this study presents a comprehensive strategy for enhancing immersion boiling of dielectric liquids. First, optimized HPP designs were provided for ONB promotion, with HPP3's larger, re-entrant cavities achieving the best long-term performance. Then, a prepared plan for solving worsening ΔT_{ONB} in smaller-pore HPPs was provided through the novel hybrid HPP-HF surface. This approach not only reactivated flooded cavities but also optimized energy consumption through pulsed HF heating. Actually, the impact of dissolved gases on the ΔT_{ONB} is not fully understood. The dielectrics, like AE-3000, has a high capacity to dissolve gases than water. The presence of these gases can significantly affect the ΔT_{ONB}. In a perfectly sealed system, where concentration of dissolved gases was small, the HPP3 alone might not be sufficient to achieve the desired boiling performance. By studying HF inserting, we can gain better control over the nucleation process to help optimize ΔT_{ONB} under various operational conditions.

4.2 Prospect

1. Long-Term Stability and Performance: Extended experiments should be conducted to assess the long-term stability and performance of the HPP surfaces. This includes studying the durability of the surfaces and the consistency of the reduced ΔT_{ONB} over prolonged periods. Part of the boiling experiments results for the best performance porous plate (HPP3) was shown in Appendix C. for reference.

2. Dissolved gases effect on the ΔT_{ONB}: Previous studies have shown that the presence of dissolved gases leads to highly unstable and non-repeatable boiling incipience superheat during the boiling experiments of FC-72 and R-113 liquid. To solve this issue, dissolved gases can be removed by pre-

boiling the liquid with a pre-heater for a sufficient duration. However, it was hypothesized that extending the number of consecutive boiling experiments could further reduce the dissolved gas concentration in the vicinity of the ITO heating surface. Also increasing the number of consecutive boiling experiments may also accelerate flooding of the cavities by liquid cooling.

Based on this consideration, boiling experiments with increased running times is considered in the further research, and some results of the pre-experiments were shown in Appendix D.

3. Optimization of Cavity Geometry: Further research should explore the optimization of cavity geometries beyond size, including shape, distribution, and arrangement on the HPP surfaces. Advanced modeling and simulation techniques could be employed to predict the most effective designs.

4. Integration with Microelectronic Devices: Practical integration of optimized HPP surfaces with actual microelectronic devices should be explored. This involves addressing challenges related to manufacturing, scalability, and compatibility with existing cooling systems.

5. Advanced Measurement Techniques: Develop and implement advanced measurement techniques to capture local superheat and nucleation events more accurately. High-resolution thermal imaging and micro-scale sensors could provide deeper insights into the boiling processes on engineered surfaces.

References

[1] M. Sharma, K. Arunachalam, D. Sharma, Analyzing the Data Center Efficiency by Using PUE to Make Data Centers More Energy Efficient by Reducing the Electrical Consumption and Exploring New Strategies, Procedia Computer Science 48 (2015) 142–148.

[2] C. Nadjahi, H. Louahlia, S. Lemasson, A review of thermal management and innovative cooling strategies for data center, Sustainable Computing: Informatics and Systems 19 (2018) 14–28.

[3] A.C. Kheirabadi, D. Groulx, Cooling of server electronics: A design review of existing technology, Applied Thermal Engineering 105 (2016) 622–638.

[4] Z. Zhang, X. Wang, Y. Yan, A review of the state-of-the-art in electronic cooling, E-Prime - Advances in Electrical Engineering, Electronics and Energy 1 (2021) 100009.

[5] K.C. Leong, J.Y. Ho, K.K. Wong, A critical review of pool and flow boiling heat transfer of dielectric fluids on enhanced surfaces, Applied Thermal Engineering 112 (2017) 999–1019.

[6] J.R. Black, Electromigration—A brief survey and some recent results, IEEE Transactions on Electron Devices 16 (1969) 338–347.

[7] Advanced Flip Chip Packaging, SpringerLink, (n.d.).

[8] Full article: Evaluation of Jet Impingement, Spray and Microchannel Chip Cooling Options for High Heat Flux Removal, (n.d.).

[9] D.A. Hall, G.C. Vliet, T.L. Bergman, Natural Convection Cooling of Vertical Rectangular Channels in Air Considering Radiation and Wall Conduction, Journal of Electronic Packaging 121 (1999) 75–84.

[10] N.A. Pambudi, A. Sarifudin, R.A. Firdaus, D.K. Ulfa, I.M. Gandidi, R. Romadhon, The immersion cooling technology: Current and future development in energy saving, Alexandria Engineering Journal 61 (2022) 9509–9527.

[11] M.K. Sung, I. Mudawar, Single-phase and two-phase hybrid cooling schemes for high-heat-flux thermal management of defense electronics, J. Electron. Packag.131 (2009).

[12] M. Visaria, I. Mudawar, Application of two-phase spray cooling for thermal management of electronic devices, IEEE Trans. Compon. Packag. Technol. 32(2009) 784–793.

[13] I. Mudawar, Assessment of high-heat-flux thermal management schemes, IEEE Trans. Compon. Packag. Technol. 24 (2001) 122–141.

[14] M. Arik, A. Bar-Cohen, S.M. You, Enhancement of pool boiling critical heat flux in dielectric liquids by microporous coatings, Int. J. Heat Mass Transf. 50 (2007)997–1009.

[15] A. Bar-Cohen, W. Tong, T.W. Simon, Theoretical aspects of nucleate pool boiling with

dielectric liquids, J. Therm. Sci. 1 (1992) 46–57.
[16] Guoping Xu, B. Guenin, M. Vogel, Extension of air cooling for high power processors, in: The Ninth Intersociety Conference on Thermal and Thermomechanical Phenomena in Electronic Systems (IEEE Cat. No.04CH37543), IEEE, Las Vegas, NV, USA, 2004: pp. 186–193.
[17] M.H. Rausch, L. Kretschmer, S. Will, A. Leipertz, A.P. Fröba, Density, Surface Tension, and Kinematic Viscosity of Hydrofluoroethers HFE-7000, HFE-7100, HFE-7200, HFE-7300, and HFE-7500, J. Chem. Eng. Data 60 (2015) 3759–3765.
[18] I. L. Pioro, W. Rohsenow, and S. S. Doerffer, "Nucleate pool-boiling heat transfer. I: review of parametric effects of boiling surface," International Journal of Heat and Mass Transfer, vol. 47, no. 23, pp. 5033–5044, Nov. 2004.
[19] B. Bourdon, E. Bertrand, P. Di Marco, M. Marengo, R. Rioboo, and J. De Coninck, "Wettability influence on the onset temperature of pool boiling: Experimental evidence onto ultra-smooth surfaces," Advances in Colloid and Interface Science, vol. 221, pp. 34–40, Jul. 2015.
[20] C. Corty, A.S. Foust, Surface variables in nucleate boiling, American Institute of Chemical Engineers, New York, 1953.
[21] Nukiyama, S., The Maximum and Minimum Values of the Heat transmitted from Metal to boiling Water under atmospheric Pressure. Journal Japan Society Mechanical Eng., Vol. 37, pp. 367, 1934 (in Japanese).
[22] Drew, T.B.; Mueller, A.C. Boiling. Trans. AIChE 1937, 33, 449–473.
[23] G. Liang and I. Mudawar, "Pool boiling critical heat flux (chf) – part 1: Review of mechanisms, models, and correlations," International Journal of Heat and Mass Transfer, vol. 117, pp. 1352 –1367, 2018. 7
[24] S. Kutateladze, Boiling and bubbling heat transfer under free convection of liquid, International Journal of Heat and Mass Transfer, vol. 22, pp. 281–299, 1979.
[25] B. S. Petukhov and S. A. Kovalev, Methodics and some results of measuring critical load during transition from film to nucleate boiling. Teploenergetika 5, 65 (1962) (in Russian).
[26] G. Hesse, Heat transfer in nucleate boiling, maximum heat flux and transition boiling. Int. J. Heat Mass Transfer 16, 161 1- 1627 (1973).
[27] N. Zuber, On the stability of boiling heat transfer. J. Heat Transfer 80, No. 3, 7 1 1-720 (1958).
[28] T. Aoki and J. R. Welty, Energy transfer mechanisms in transition pool boiling. International Journal of Heat and Mass Transfer, vol. 13, pp. 1237 – 1240, 1970.
[29] Y. Katto, et al. Mechanism of boiling crisis and transition boiling on pool boiling. Proc. Int. Heat Transfer Conf. 4th. 1970, 5 (1970).

[30] S. Ishigai, T. Kuno. Experimental study of transition boiling on a vertical wall in open vessel. Bull JSME, 9 (No. 34) (1966), pp. 361-368.
[31] S. A. Kovalev, On methods of studying heat transfer in transition boiling. Int. J. Heat Mass Tramfer 11, No. 2,279-283 (1968); 13, No. 11, 1505- 1506 (1970).
[32] Y. P. Chang, Wave theory of heat transfer in film boiling, Journal of Heat Transfer 81 (1) (1959) 1-8. 81, No. 1,
[33] P. J. Berenson, Film boiling heat transfer from a horizontal surface. Znt. J. Heat Transfer 83, No. 3 (1961).
[34] J. H. Lienhard and P. T. Y. Wong, The dominant unstable wavelength and minimum heat flux during film boiling on a horizontal cylinder. Int. J. Heat Transfer 86, No. 2 (1964).
[35] R. C. Kesselring et al., Transition and film boiling from horizontal strips. AIChE J. 13, Heat Mass Transfer 13, 1237- 1240 (1970).
[36] R. M. Canon and E. L. Park, Transition boiling of normal pentane from a horizontal flat gold surface at one atmosphere pressure. Int. J. Heat Mass Transfer 19, No. 6,696-698 (1976).
[37] V. A. Grigorev, Yu. M. Pavlov, and E. V. Ametistov, Boiling of Griogenic Liquids. Energia, Moscow, 1977 (in Russian).
[38] A. J. Lowery and J. H. Westwater, Heat transfer to boiling methanol-Effect of added agents. Ind. Eng. Chem. 49, No. 9, 1445- 1448 (1957).
[39] C. Corty, A.S. Foust, Surface variables in nucleate boiling, American Institute of Chemical Engineers, New York, 1953.
[41] K.C. Leong, J.Y. Ho, K.K. Wong, A critical review of pool and flow boiling heat transfer of dielectric fluids on enhanced surfaces, Applied Thermal Engineering, 112 (2017) 999-1019.
[42] G. Liang, I. Mudawar, Review of pool boiling enhancement by surface modification, International Journal of Heat and Mass Transfer, 128 (2019) 892-933.
[43] D.W. Zhou, C.F. Ma, J. Yu, Boiling hysteresis of impinging circular submerged jets with highly wetting liquids, International Journal of Heat and Fluid Flow, 25(1) (2004) 81-90.
[44] C.F. Ma, A.E. Bergles, Jet impingement nucleate boiling, International Journal of Heat and Mass Transfer, 29(8) (1986) 1095-1101.
[45] H. B. Clark, P. S. Strenge, and J. W. Westwater, “ACTIVE SITES FOR NUCLEATE BOILING,” Chem. Eng. Progr., vol. Vol: 55, Symposium Ser. No. 29, Jan. 1959, Accessed: Aug. 04, 2023. [Online].
[46] K. Cornwell, Naturally formed boiling site cavities, Letters in Heat and Mass Transfer 4 (1977) 63–71.

[47] K. Cornwell, R.B. Schüller, A study of boiling outside a tube bundle using high speed photography, International Journal of Heat and Mass Transfer 25 (1982) 683–690.
[48] K. Cornwell, On boiling incipience due to contact angle hysteresis, International Journal of Heat and Mass Transfer 25 (1982) 205–211.
[49] J.J. (James J. Lorenz, The effects of surface conditions on boiling characteristics., Thesis, Massachusetts Institute of Technology, 1972.
[50] L.L. Manetti, G. Ribatski, R.R. Souza, E.M. Cardoso, Pool boiling heat transfer of HFE-7100 on metal foams, Experimental Thermal and Fluid Science, 113 (2020) 110025.
[51] M. S. El-Genk, J. L. Parker, Enhanced boiling of HFE-7100 dielectric liquid on porous graphite, Energy Conversion and Management, 46 (15-16) (2005) 2455-2481.
[52] Gregorcic, P.; Zupancic, M.; Golobic, I. Scalable Surface Microstructuring by a Fiber Laser for Controlled Nucleate Boiling Performance of High- and Low-Surface-Tension Fluids. Sci. Rep. 2018, 8, 7461.
[53] Ho, J.Y.; Wong, K.K.; Leong, K.C. Saturated pool boiling of FC-72 from enhanced surfaces produced by Selective Laser Melting. Int. J. Heat Mass Transf. 2016, 99, 107–121.
[54] Orman, L.J.; Radek, N.; Pietraszek, J.; Szczepaniak, M. Analysis of Enhanced Pool Boiling Heat Transfer on Laser-Textured Surfaces. Energies 2020, 13, 2700. [Google Scholar] [CrossRef]
[55] Moze, M.; Vajc, V.; Zupancic, M.; Golobic, I. Hydrophilic and Hydrophobic Nanostructured Copper Surfaces for Efficient Pool Boiling Heat Transfer with Water, Water/Butanol Mixtures and Novec 649. Nanomaterials 2021, 11, 3216.
[56] Su, C.Y.; Yang, C.Y.; Jhang, B.W.; Hsieh, Y.L.; Sin, Y.Y.; Huang, C.C. Pool Boiling Heat Transfer Enhanced by Fluorinated Graphene as Atomic Layered Modifiers. ACS Appl. Mater. Interfaces 2020, 12, 10233–10239.
[57] H. Honda, J.J. Wei, Enhanced boiling heat transfer from electronic components by use of surface microstructures, Experimental Thermal and Fluid Science, 28(2) (2004) 159-169.
[58] Y.W. Lu, S.G. Kandlikar, Nanoscale surface modification techniques for pool boiling enhancement—A critical review and future directions, Heat Transfer Engineering, 32(10) (2011) 827-842.
[59] C.M. Patil, S.G. Kandlikar, Review of the manufacturing techniques for porous surfaces used in enhanced pool boiling, Heat Transfer Engineering, 35(10) (2014) 887-902.
[60] S.J. Thiagarajan, R. Yang, C. King, S. Narumanchi, Bubble dynamics and nucleate pool boiling heat transfer on microporous copper surfaces, Int. J. Heat Mass Transf. 89 (2015) 1297–1315.
[61] A. Bar-Cohen and T. W. Simon, “wall Superheat Excursions in the Boiling incipience of

Dielectric Fluids," Heat Transfer Engineering, vol. 9, no. 3, pp. 19–31, Jun. 1988.
[62] S. G. Bankoff, "Entrapment of gas in the spreading of a liquid over a rough surface," AIChE J., vol. 4, no. 1, pp. 24–26, Mar. 1958.
[63] T. Liu, C.-J. Kim, Doubly re-entrant cavities to sustain boiling nucleation in FC-72, in: 2015 28th IEEE Int. Conf. Micro Electro Mech. Syst. MEMS, IEEE, Estoril, Portugal, 2015: pp. 1122–1124.
[64] A. Tuteja, W. Choi, J. M. Mabry, G. H. McKinley, R. E. Cohen, Proc. Natl. Acad. Sci. U.S.A. 105, 18200–18205 (2008).
[65] R. Hensel et al., Langmuir 29, 1100–1112 (2013).
[66] Tingyi Leo Liu, Chang-Jin, CJ. Kim, Turning a surface super repellent even to completely wetting liquids. Science346,1096-1100(2014).
[67] Y.Y. Hsu, On the Size Range of Active Nucleation Cavities on a Heating Surface, J. Heat Transf. 84 (1962) 207–213.
[68] Mudawar, T.M. Anderson, Parametric investigation into the effects of pressure, subcooling, surface augmentation and choice of coolant on pool boiling in the design of cooling systems for high-power-density electronic chips, Journal of Electronic Packaging, (112), (1990), 375-382.
[69] McCoubrey, J. C., & Singh, N. M. Viscosity of some fluorocarbons in the vapor phase. Trans. Faraday Soc., 56, (1960) 486-489.
[70] Fellows B.R., Richard R.G., Shankland I.R, Thermal conductivity data for some environmentally acceptable fluorocarbons in Thermal Conductivity 21, 1990 - book edited by Cremers C.J. and Fine H.A.
[71] M.H. Rausch, L. Kretschmer, S. Will, A. Leipertz, A.P. Fröba, Density, Surface Tension, and Kinematic Viscosity of Hydrofluoroethers HFE-7000, HFE-7100, HFE-7200, HFE-7300, and HFE-7500, J. Chem. Eng. Data 60 (2015) 3759–3765.
[72] F.P. Pike, P.D. Miller, K. Beatty, Effect of gas evolution on surface boiling at wire coils, Chem. Eng. Prog. Symp. Ser., 51 (1955), pp. 13-19.
[73] R.W. Murphy, A.E. Bergles, Subcooled flow boiling of fluorocarbons—hysteresis and dissolved gas effects on heat transfer, Proc. Heat Transfer and Fluid Mech. Inst., Stanford Univ. Press, Stanford, CA (1972), pp. 400-416.
[74] Jeschar, R., Kraushaar, H. and Griebel, H., 1996, Influence of gases dissolved in cooling water on heat transfer during stable film boiling, Steel Research, Vol. 67, No. 6, pp.227-234.
[75] Keitel, G., and Onken, U., Inhibition of bubble coalescence by solutes in air-water dispersions, Chernical Engineering Science, Vol. 17, pp. 1635-1 638.

[76] Limelette, P. et al, Influence of ferroelastic domain walls on thermal conductivity, Physical Review B (2023).
[77] Kaźmierczak-Bałata, A., Bodzenta, J., Dehbashi, M., Mayandi, J., & Venkatachalapathy, V. (2022). Influence of Post Processing on Thermal Conductivity of ITO Thin Films. Materials, 16.
[78] Johannes, C., Lins, F., Meyer, M., Hartung, M., & Heim, H. (2023). The Influence of Thermal and Mechanical Stress on the Electrical Conductivity of ITO-Coated Polycarbonate Films. Polymers, 15.
[79] Du, X., Li, X., Zhang, Y., Guo, X., Li, Z., Cao, Y., Yang, Y., Wang, W., & Wang, J, Visible transparent, infrared stealthy polymeric films with nanocoating of ITO enable efficient passive radiative heating and solar/electric thermal conversion. Nano Research, 16 (2022), 3326-3332.
[80] B.N. Taylor, C.E. Kuyatt, Guidelines for evaluating and expressing the uncertainty of NIST measurement results, (n.d.).
[81] A. Luke, Pool boiling heat transfer from horizontal tubes with different surface roughness, International Journal of Refrigeration, 20(8) (1997) 561-574.
[82] K. Ferjančič, I. Golobič, Surface effects on pool boiling CHF, Experimental Thermal and Fluid Science, 25(7) (2002) 565-571.
[83] H. O'Hanley, C. Coyle, J. Buongiorno, T. McKrell, L.W. Hu, M. Rubner, R. Cohen, Separate effects of surface roughness, wettability, and porosity on the boiling critical heat flux, Applied Physics Letters, 103(2) (2013) 024102.
[84] Wang, C., Su, G., Akinsulire, O., Zhang, L., Rahman, M. M., & Bucci, M, Investigation of critical heat flux enhancement on nanoengineered surfaces in pressurized subcooled flow boiling using infrared thermometry. Heat Transfer Engineering, 45(4–5), 417–432 (2023).
[85] G.-Y. Su, et al., Investigation of flow boiling heat transfer and boiling crisis on a rough surface using infrared thermometry, Int. J. Heat Mass Transf., vol. 160, pp. 120134, Oct. 2020.
[86] VDI e. V., Ed., VDI Heat Atlas. Berlin, Heidelberg: Springer Berlin Heidelberg, 2010.
[87] T. Fujii and H. Imura, Natural-convection heat transfer from a plate with arbitrary inclination, International Journal of Heat and Mass Transfer, vol. 15, no. 4, pp. 755–767, Apr. 1972.
[88] "Discrete transitions in turbulent convection," Proc. R. Soc. Lond. A, vol. 225, no. 1161, pp. 185–195, Aug. 1954.
[89] N. Zuber, "Nucleate boiling. The region of isolated bubbles and the similarity with natural convection," International Journal of Heat and Mass Transfer, vol. 6, no. 1, pp. 53–78, Jan. 1963.
[90] Mcadams William H., Heat Transmission. 1942. Accessed: May 02, 2024. [Online]. Available: http://archive.org/details/in.ernet.dli.2015.238768.

[91] A. E. Bergles and W. M. Rohsenow, “The Determination of Forced-Convection Surface-Boiling Heat Transfer,” Journal of Heat Transfer, vol. 86, no. 3, pp. 365–372, Aug. 1964.
[92] J. M. S. Jabardo, E. F. da Silva, G. Ribatski, and S. F. de Barros, “Evaluation of the rohsenow correlation through experimental pool boiling of halocarbon refrigerants on cylindrical surfaces,” J. Braz. Soc. Mech. Sci. & Eng., vol. 26, pp. 218–230, Jun. 2004.
[93] D. Lee, B. S. Kim, H. Moon, N. Lee, S. Shin, and H. H. Cho, “Enhanced boiling heat transfer on nanowire-forested surfaces under subcooling conditions,” International Journal of Heat and Mass Transfer, vol. 120, pp. 1020–1030, May 2018.
[94] S. Oktay, “Departure from Natural Convection (DNC) in Low-Temperature Boiling Heat Transfer Encountered in Cooling Microelectronic LSI Devices,” Heat Transfer Engineering, vol. 9, no. 3, pp. 93–100, Jun. 1988.

Acknowledgement

As I approach the completion of my Ph.D., I am filled with gratitude for the many individuals who have supported and guided me throughout my journey. In this section, I would like to acknowledge their invaluable contributions and express my deepest thanks.

First and foremost, I would like to express my deepest gratitude to my supervisor, Professor Shoji Mori, for welcoming me into your group and guiding me over the past four years. The extensive knowledge I have gained in boiling heat transfer and other subjects from you has profoundly shaped this work and will continue to influence me long after my time at Kyushu University. I am also deeply thankful for your unwavering support in my personal life, especially during challenging times. Your patience and understanding have been a source of encouragement, helping me to stay positive and resilient.

I would like to extend my sincere appreciation to Professor Yasuyuki Takata and Wei Liu for your suggestions on my research and for serving as co-examiner for this thesis. Your insightful feedback has been instrumental in refining my ideas and elevating the quality of my work.

I am also grateful to Assistant Professor Yutaro Umehara for your invaluable suggestions and advice on my work. Your insights have significantly contributed to the advancement of this work.

My heartfelt thanks go to laboratory staffs, Mr. Eto and Ms. Yamashita. for their supportive roles in the laboratory. Your expertise and guidance have been crucial to the success of this research.

I am thankful to all the members of the Thermal Energy Conversion Lab for their kind help and support, which have made my time at Kyushu University both productive and enjoyable. Special thanks to Tsutomu Hisano for your assistance with testing and running experiments. I have greatly valued our intense academic discussions throughout this process. Additionally, I would like to express my gratitude to my lab-mates, Zhang, Wei, Hayashida, and Wang, for your ongoing help and support in the lab.

I also wish to thank my former advisors, Assistant Professor Zhihao Chen and Professor Yoshio Utaka. Your guidance and advice have been instrumental throughout my graduate studies. You taught me the importance of stepping out of my comfort zone, which was a key factor in my decision to pursue an academic career.

Finally, I want to express my profound gratitude to my parents and friends. Your tremendous understanding and encouragement over the past few years have been essential to the completion of my studies. Thank you for your unwavering support and belief in me.

Appendix A. Geometry of the cavities in the HPP3 through CT scan

In the HPP3, re-entrant cavities were able to be found by microcomputer tomography. Description of the processing of the scanning image was shown in Fig. A1. The process was summarized as follows:

CT Scanning: The HPP3 sample was subjected to CT scanning (SKYSCAN) to obtain a 3D representation of its internal structure.

Cavities Finding: The CT scan data was processed using an image analysis software (CTAn) to identify and locate the cavities within the porous structure, as indicated by the red highlights in the CT scan image.

3D Rebuild: The identified cavities were then used to reconstruct a 3D model of the cavity within the HPP3 sample by CTvox software.

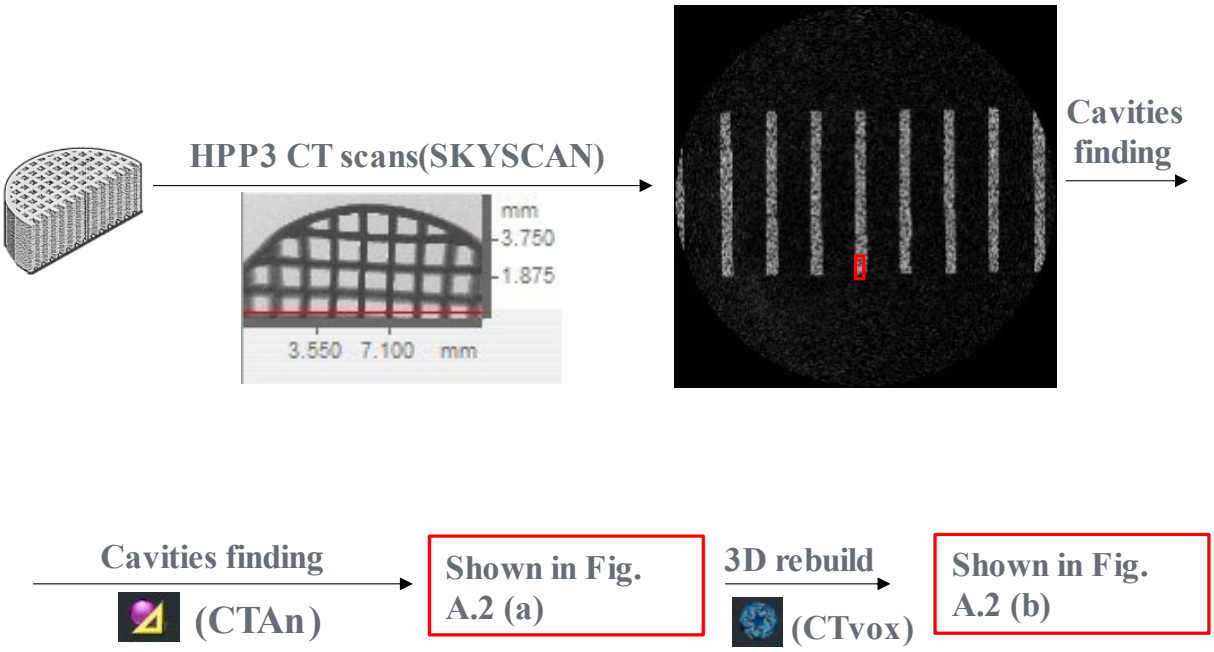

Fig. A1. Description of the processing of the scanning image for the HPP3

Re-constructed 3D models of the scanning images have confirmed that re-entrant cavities were formed in the HPP3, as shown in Fig. A2. These re-entrant cavities will play a crucial role in promoting nucleation and maintaining a reducing superheat for the ONB in the later boiling experiments.

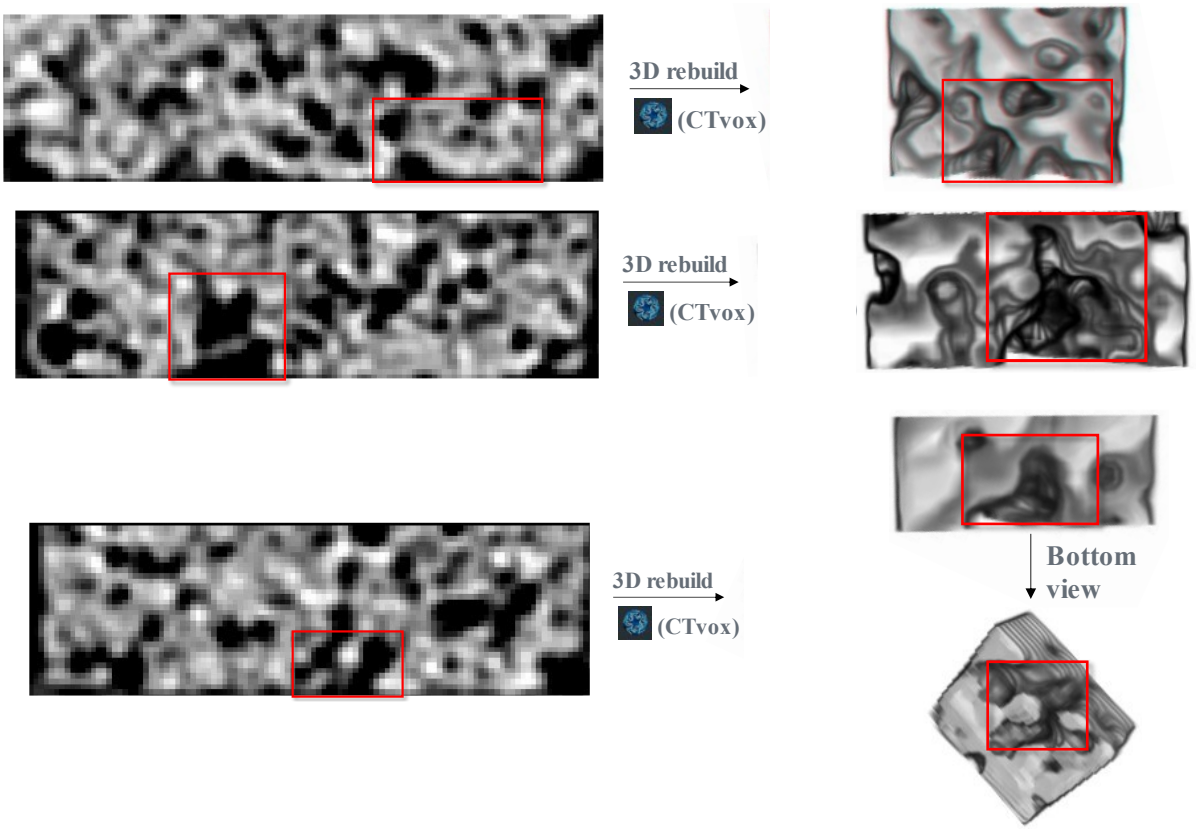

(a) (b)

Fig. A2. (a) Cavities finding results of the CTAn and (b) Re-constructed re-entrant cavities of the HPP3.

Appendix B. 3D steady calculation of the ITO heater

In boiling experiments, heat flux was provided by an ITO heater with a current interval of 0.5 A until 12 W/cm^2 (typically ~60% of the estimated CHF value). Waiting period for each current was set as 60s to reach the quasi-steady state. The two-dimensional temperature of the backside of the boiling surface was captured by the IR camera. Heat transfer analysis through the ITO heater was estimated by three-dimensional steady heat conduction equation. The waiting period for the stepwise heat flux of the ITO heater with thinner thickness was 60 s which was confirmed enough for steady state. The computational domain, as depicted in Fig. B1 (a), the size was matched the ITO heater dimensions of 40 mm (x) × 40 mm (y) × 1 mm (z). Boiling was observed occurred on the heating area as marked in purple rectangle. On the active heating area, mesh size was set as same as the actual pixel size (50 μm × 50 μm) of the IR camera, as shown in Fig B1 (b). Coarser mesh is used in the surrounding non-heating areas. The total number of cells of the x-y plane is 288 × 288. Mesh size of the thickness direction (z) was 50 μm. Boundary condition for the ITO heater was set as following:

a) Four side surfaces and the bottom surface of the sapphire: adiabatic boundary condition.

b) Top surface of the sapphire (bottom surfaces of the ITO layer) for the active heating area (10 × 10 mm) as shown in yellow rectangle: temperature boundary condition, the temperature was measured by the IR camera. Then heat conduction of the ITO layer was calculated based on the ITO layer thickness and the boiling surface temperature can be attained.

c) Top surface of the sapphire (non-boiling area): Natural convection condition with the surrounding AE-3000 liquid.

One example of the calculation result under the ONB condition (ΔT_{ONB} = 49.8 K) for the plain surface was shown in Fig. B2. A 2D slice of the superheat distribution along the x-z plane at y = 0.02 m (center of the y-coordinate) was shown in the right side of the Fig. B2. It shows that the superheat is nearly uniform along the thickness (z) direction within the heating area. The difference between the top and bottom surface temperatures in this area is less than 1.0 K, indicating efficient heat transfer. The average superheat on both the top and bottom surfaces of the active heating area under various heat flux conditions was summarized in Table B.1.

Once temperature distribution through the ITO heater was calculated, given the z-axis (thickness direction) temperature profile, the heat flux from the ITO heater to AE-3000 liquid can be calculated by Fourier conduction law as given:

$$q_{\mathrm{w}} = q - k_{\mathrm{s}}(T_{Top})\frac{T_{Top} - T(z_{\mathrm{top}} - z_{\mathrm{c}})}{z_{\mathrm{c}}} \tag{B.1}$$

where z_{top} is the z-coordinate of the top surface, the z_{c} is the distance between the top surface and the center of the adjacent cell in the z-direction, the mesh size of z_{c} is 50 μm. k_{s} is temperature-dependent thermal conductivity related to the top surface temperature. Top surface superheat ($\Delta T_{\mathrm{w}} = T_{\mathrm{top}}$-$T_{\mathrm{sat}}$) and heat flux from the ITO heater to the AE-3000 liquid (q_{w}) were used in boiling curves.

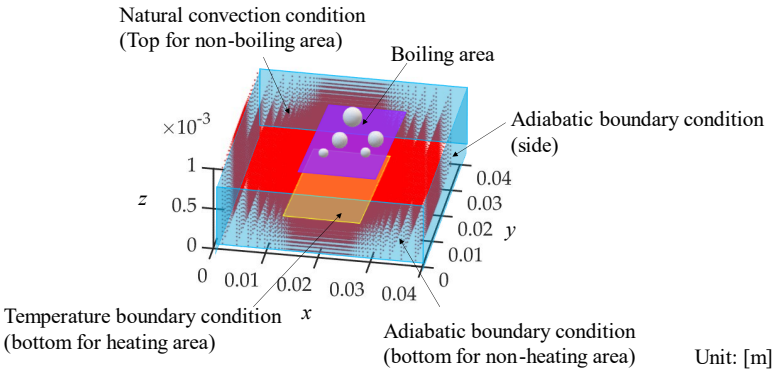

(a)

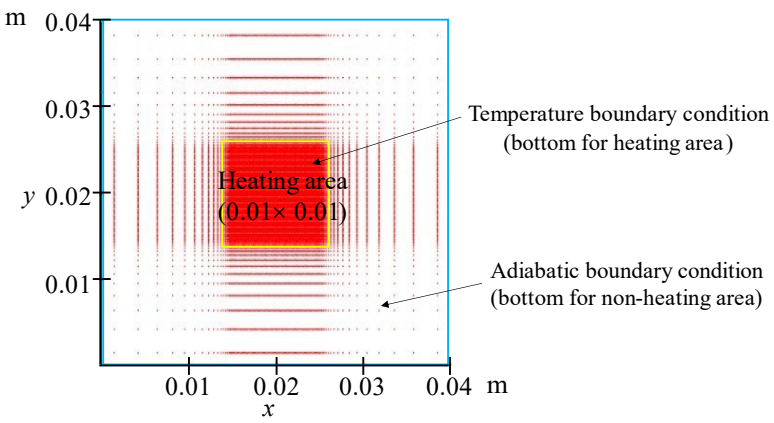

(b)

Fig. B.1 (a) Description of the computational domain and boundary conditions and (b) *x*-*y* plane.

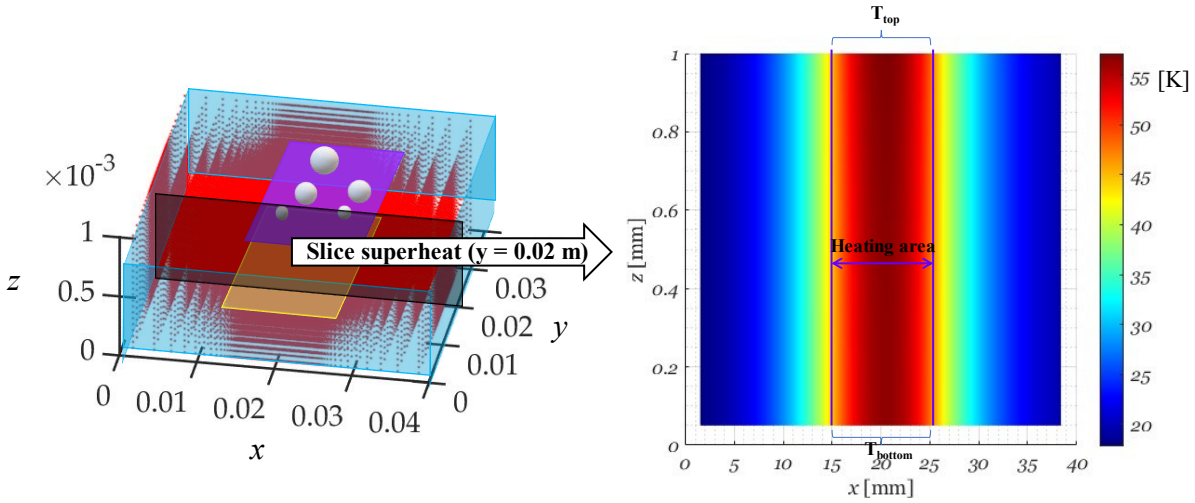

Fig. B.2 *x*-*z* plane temperature distribution under the ONB condition for the plain surface (ΔT_{ONB} = 49.8 K).

Table B.1 Average superheat on the top and bottom surfaces of the active heating area

$q[W/cm^2]$	$T_{top-avg}[K]$	$T_{\text{bottom-avg}}[K]$	$T_{\text{top-avg}} - T_{\text{bottom-avg}}[K]$
3.3	20.4	20.1	0.3
5.0	30.2	29.7	0.5
7.9	49.8	49.2	0.6

Appendix C. ΔT_{ONB} of the HPP3 over longer immersion time

Extended boiling experiments with longer immersion time was conducted on the best performance porous plate (HPP3) to test the long-term stability and performance of the ΔT_{ONB}. As

shown in Fig. C.1, ΔT_{ONB} of the HPP3 was increased gradually with increasing immersing times. For immersion times up to 192 hours, nearly eliminated boiling curves were achieved, indicating excellent boiling performance with very low ΔT_{ONB}. After around 400 hours of immersion, degradation in the ΔT_{ONB} was observed. The maximum ΔT_{ONB} of 14.5 K was found during the 453-hour immersion experiments. However, even after 500 hours, the ΔT_{ONB} remained below the operating temperature requirement. Detail of the ΔT_{ONB} during each immersing time was summarized in Table C.1.

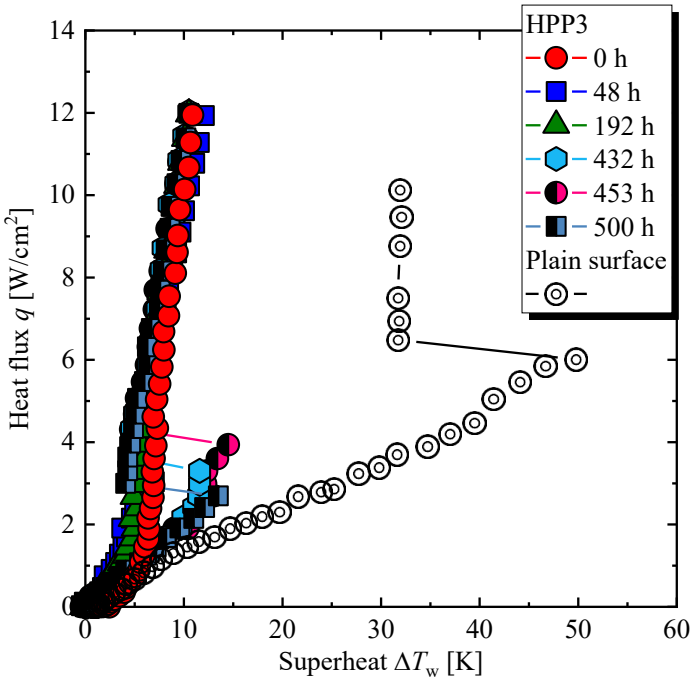

Fig. C.1 Boiling performance on the HPP3 over longer immersion time.

Table C.1 ΔT_{ONB} of the HPP3 among immersion time.

Immersion times	ΔT_{ONB} [K]
0 h	Nearly eliminated ΔT_w excursion
48 h	Nearly eliminated ΔT_w excursion
192 h	Nearly eliminated ΔT_w excursion
432 h	11.6(ΔT_w excursion = 7.0 K)
453 h	14.5(ΔT_w excursion = 9.9 K)
500 h	13.5(ΔT_w excursion = 9.4 K)

Appendix D. ΔT_{ONB} of the HPP2 and HPP3 among running times

Previous studies have shown that the presence of dissolved gases leads to highly unstable and non-repeatable boiling incipience superheat during the boiling experiments of FC-72 and R-113 liquid. To solve this issue, dissolved gases can be removed by pre-boiling the liquid with a pre-heater for a sufficient duration.

In our experiments, the reproducibility of the ΔT_{ONB} was confirmed over three consecutive boiling experiments. However, it was hypothesized that extending the number of consecutive boiling experiments could further reduce the dissolved gas concentration in the vicinity of the ITO heating surface. Also increasing the number of consecutive boiling experiments may also accelerate flooding of the cavities by liquid cooling.

Based on this consideration, additional experiments were conducted with increased running times, extending the number of consecutive boiling experiments to 6 or 7. The same experimental procedure, as discussed in the Chapter 2 was employed.

As shown in Fig. D.1, ΔT_{ONB} of the HPP2 was increased gradually with increasing running times. For the initial boiling experiments, the ΔT_{ONB} was 11.0 K. With each subsequent boiling run, ΔT_{ONB} was increased, reaching a maximum of 15.5 K by the 6th run. Detail of the ΔT_{ONB} during each subsequent boiling run was summarized in Table D.1.

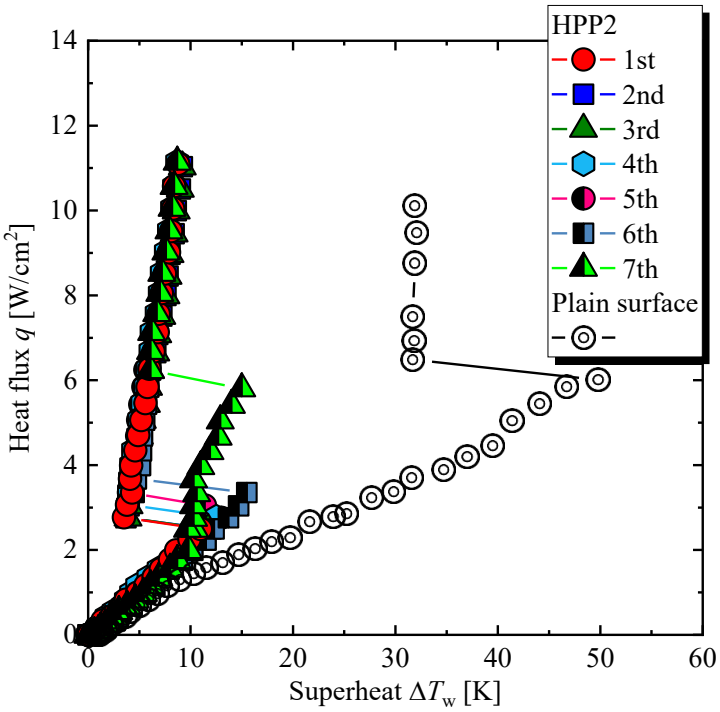

Fig. D.1 Effect of the running times on the ΔT_{ONB} of the HPP2.

Table D.1 ΔT_{ONB} of the HPP2 among running times.

Running times	ΔT_{ONB} [K]	Running times	ΔT_{ONB} [K]
1st	11.0	5th	11.4
2nd	12.0	6th	15.5
3rd	12.4	7th	15.0
4th	12.5		

Similarly, boiling curves of the HPP3 among multiple boiling runs were shown in Fig. D.2. During the first and second runs, the boiling curve exhibited eliminated superheat excursion, indicating a stable and ideal performance with lower boiling incipience superheat. From the third run onwards, ΔT_{ONB} could be identified by superheat excursion and reach a maximum of 10.5 K by the 6th run. With the increase in ΔT_{ONB}, superheat excursions also appeared and worsened with each run. At the 6th run, not only maximum of the ΔT_{ONB} was shown but also higher superheat excursion of 6.3 K was found. Detail of the ΔT_{ONB} and superheat excursion during each subsequent boiling run was summarized in Table D.2.

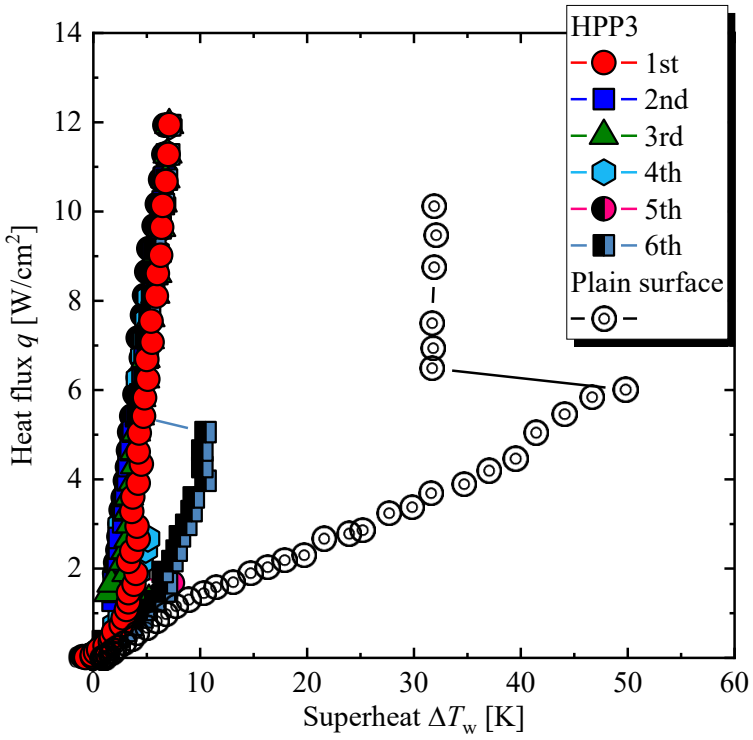

Fig. D.2 Effect of the running times on the ΔT_{ONB} of the HPP3.

Table D.2 ΔT_{ONB} of the HPP3 among running times.

Running times	ΔT_{ONB} [K]
1st	Nearly eliminated ΔT_w excursion
2nd	Nearly eliminated ΔT_w excursion
3rd	5.2(ΔT_w excursion = 3.8 K)
4th	5.1(ΔT_w excursion = 2.6 K)
5th	7.4(ΔT_w excursion = 5.4 K)
6th	10.5(ΔT_w excursion = 6.3 K)